

ROLE OF TRANSITION METAL CATALYSTS IN HYDROGEN  
ADSORPTION KINETICS ON SURFACES OF HYDROGEN  
STORAGE MATERIALS: A COMPUTATIONAL STUDY

PATCHARAPORN KHAJONDETHAIRIT



A Thesis Submitted in Partial Fulfillment of the Requirements for the  
Degree of Doctor of Philosophy in Chemistry  
Suranaree University of Technology  
Academic Year 2021

บทบาทของตัวเร่งปฏิกิริยาโลหะทรานซิชันต่อจลนพลศาสตร์  
การดูดซับของไฮโดรเจนบนพื้นผิววัสดุกักเก็บไฮโดรเจน:  
การศึกษาเชิงคำนวณ



นางสาวพัชราภรณ์ ขจรเดชชัยฤทธิ

วิทยานิพนธ์นี้เป็นส่วนหนึ่งของการศึกษาตามหลักสูตรปริญญาวิทยาศาสตรดุษฎีบัณฑิต  
สาขาวิชาเคมี  
มหาวิทยาลัยเทคโนโลยีสุรนารี  
ปีการศึกษา 2564

ROLE OF TRANSITION METAL CATALYSTS IN HYDROGEN ADSORPTION  
KINETICS ON SURFACES OF HYDROGEN STORAGE MATERIALS:  
A COMPUTATIONAL STUDY

Suranaree University of Technology has approved this thesis submitted in partial fulfillment of the requirements for the Degree of Doctor of Philosophy.

Thesis Examining Committee



(Dr. Anchalee Junkaew)

Chairperson



(Asst. Prof. Dr. Suwit Suthirakun)

Member (Thesis Advisor)



(Dr. Pussana Hirunsit)

Member (Thesis Co-Advisor)



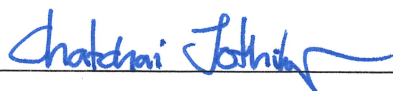
(Prof. Dr. Kritsana Sagarik)

Member



(Assoc. Prof. Dr. Rapee Utke)

Member



(Assoc. Prof. Dr. Chatchai Jothityangkoon)

Vice Rector for Academic Affairs

and Quality Assurance



(Prof. Dr. Santi Maensiri)

Dean of Institute of Science

พัชรภรณ์ ขจรเดชชัยฤทธิ์ : บทบาทของตัวเร่งปฏิกิริยาโลหะทรานซิชันต่อจลนพลศาสตร์ การดูดซับของไฮโดรเจนบนพื้นผิววัสดุกักเก็บไฮโดรเจน: การศึกษาเชิงคำนวณ (ROLE OF TRANSITION METAL CATALYSTS IN HYDROGEN ADSORPTION KINETICS ON SURFACES OF HYDROGEN STORAGE MATERIALS: A COMPUTATIONAL STUDY)  
อาจารย์ที่ปรึกษา : ผู้ช่วยศาสตราจารย์ ดร.สุวิทย์ สุธีรากุล, 110 หน้า.

คำสำคัญ: วัสดุกักเก็บไฮโดรเจน, เฟิร์สพริซินิเฟิล, วัสดุแมกนีเซียมไฮไดรด์, วัสดุคาร์บอน

วิทยานิพนธ์นี้ใช้ระเบียบวิธีวิจัยการคำนวณบนพื้นฐานของทฤษฎีฟังก์ชันนอลความหนาแน่นในการศึกษาบทบาทของตัวเร่งปฏิกิริยาโลหะทรานซิชันต่อการปรับปรุงคุณสมบัติ ทั้งทางด้านจลนศาสตร์และอุณหพลศาสตร์ของปฏิกิริยาการดูดซับไฮโดรเจนในวัสดุกักเก็บไฮโดรเจน ซึ่งงานวิจัยก่อนหน้านี้พบว่า การเพิ่มตัวเร่งปฏิกิริยานิกเกิลและวานาเดียมลงในวัสดุแมกนีเซียมช่วยลดพลังงานการกักเก็บมันต์ในการเกิดปฏิกิริยาการดูดซับและการคายซับได้เป็นอย่างดี จากผลการทดลองดังกล่าว พบว่าการเพิ่มตัวเร่งปฏิกิริยานิกเกิลจะอยู่ในรูปแบบของสารประกอบแมกนีเซียมนิกเกิล การเพิ่มตัวเร่งปฏิกิริยวานาเดียมในรูปแบบของอนุภาคนาโนบนพื้นผิววัสดุสารประกอบแมกนีเซียมนิกเกิล จากผลการคำนวณพบว่าทั้งตัวเร่งปฏิกิริยานิกเกิลและวานาเดียมเพื่อช่วยให้การดูดซับของไฮโดรเจนบนพื้นผิว มีความเสถียรขึ้นและเกิดกระบวนการแตกตัวของไฮโดรเจนโมเลกุลได้ดีขึ้น ซึ่งการเพิ่มตัวเร่งปฏิกิริยวานาเดียมบนพื้นผิวแมกนีเซียมนิกเกิลนั้นทำให้เกิดการเรียงตัวของพื้นผิววัสดุในรูปแบบใหม่ ที่ทำให้ไฮโดรเจนสามารถดูดซับบนพื้นผิวได้มากขึ้นและทำให้เกิดเส้นทางในการแพร่จากอนุภาคนาโนลงไปที่พื้นผิวได้รวดเร็วขึ้น เพราะการใช้พลังงานกระตุ้นในการแพร่ต่ำลง และการเพิ่มปริมาณของไฮโดรเจนช่วยลดพลังงานกักเก็บมันต์ในการแพร่ลงไปภายในวัสดุ จากผลการคำนวณพบว่าพลังงานกักเก็บมันต์ลดลงมาครึ่งหนึ่งเมื่อเทียบกับสถานะที่มีไฮโดรเจนต่ำ โดยผลของตัวเร่งปฏิกิริยานิกเกิลและวานาเดียมถูกสนับสนุนจากผลการคำนวณการจำลองพลวัตเชิงโมเลกุลซึ่งพบว่าไฮโดรเจนสามารถแตกตัวและถูกดูดซับได้ดีบนตัวเร่งปฏิกิริยาและสามารถแพร่ต่อไปภายในวัสดุได้นอกจากนี้ ผู้วิจัยได้ศึกษาบทบาทของโลหะนิกเกิลที่อยู่บนพื้นผิวของวัสดุคาร์บอนร่วมกับการทดลองผลจากการทดลองพบว่า การเติมอนุภาคนิกเกิลขนาดนาโนลงในวัสดุคาร์บอนสามารถเพิ่มปริมาณการกักเก็บไฮโดรเจนได้อย่างดียิ่ง นอกจากนี้พื้นฐานทางด้านการทดลองแสดงให้เห็นว่าการใช้สารตั้งต้นของวัสดุคาร์บอนที่แตกต่างกัน จะพบความไม่สมบูรณ์ของพื้นผิววัสดุคาร์บอนที่มีลักษณะแตกต่างกันด้วย ซึ่งทำให้เกิดแรงระหว่างอนุภาคของนิกเกิลกับพื้นผิววัสดุคาร์บอนที่แตกต่างกัน ผลการคำนวณพบว่าคลัสเตอร์ของนิกเกิลขนาดสิบสามอะตอมสามารถเกิดอันตรกิริยาอย่างแข็งแกร่งกับพื้นผิววัสดุคาร์บอนที่ประกอบด้วยอะตอมของธาตุอื่น ๆ เช่น ไนโตรเจน หรือออกซิเจน ซึ่งการเกิด

อันตรกิริยาที่แข็งแกร่งนี้ทำให้การรวมตัวกันของอนุภาค निकเกิดเกิดขึ้นได้ยากในระหว่างกระบวนการดูดซับของไฮโดรเจนและส่งผลโดยตรงต่อการเพิ่มขึ้นของปริมาณการกักเก็บไฮโดรเจนของวัสดุที่มีคาร์บอนเป็นองค์ประกอบหลักอีกด้วย



สาขาวิชาเคมี

ปีการศึกษา 2564

ลายมือชื่อนักศึกษา Patcharaporn

ลายมือชื่ออาจารย์ที่ปรึกษา Ant

ลายมือชื่ออาจารย์ที่ปรึกษาร่วม Pisun

PATCHARAPORN KHAJONDETHAIRIT : ROLE OF TRANSITION METAL CATALYSTS  
IN HYDROGEN ADSORPTION KINETICS ON SURFACES OF HYDROGEN STORAGE  
MATERIALS: A COMPUTATIONAL STUDY. THESIS ADVISOR : ASST. PROF. SUWIT  
SUTHIRAKUN, Ph.D. 110 PP.

Keyword: Hydrogen storage, first-principles calculations, Mg-based hydrides, Carbon-based materials

In this thesis, computational tools based on density functional theory (DFT) were utilized to study the roles transition metal catalysts on improving kinetics and thermodynamics of hydrogen absorption in the chemical storage materials. Previous experimental study reported that, upon adding Ni and V catalysts in the Mg, formation enthalpy and activation energies of de/hydrogenation were dramatically decreased. As evidenced from the experimental observations, this research studied the effect of Ni catalysts in the form of  $Mg_2Ni$  surface whereas the deposition of V catalyst exists as a cluster on the surface. It was found that both V and Ni help stabilize hydrogen adsorption and facilitate dissociation of the H—H bond. The V cluster adding on the  $Mg_2Ni$  surface induces surface reconstruction which in turn provides extra adsorption sites and creates facile diffusion paths where hydrogen can easily spillover from the cluster to the surface. The diffusion kinetics on the surface are also improved where the formation of connected Ni sites serves as low-energy diffusion paths. Although the subsurface diffusion into the materials requires higher barriers, increasing hydrogen coverages reduces such barriers by a half suggesting that hydrogen absorption into the materials is kinetically appreciable at operating conditions of high  $H_2$  pressure. The catalytic roles of Ni and V are supported by the results obtained from AIMD simulations where hydrogen prefers to dissociatively adsorb on the TM sites and can further diffuse into the subsurface region.

Next, the role of Ni decorated on carbon-based material was studied. The experimental study reported that, upon adding Ni nanoparticle in the carbon-based material, the hydrogen uptake was increased. As evidenced from the experimental observations, the carbon-based material was synthesized by difference carbon sources

which obtain difference defect on carbon-based materials. The combination effect of Ni catalysts and hetero defect graphene was studied. Computations show that the  $\text{Ni}_{13}$  cluster binds dramatically strong to the defect graphene. Such strong interactions could inhibit Ni sintering upon hydrogen sorption leading to superior hydrogen storage capability and long cycle life.



School of Chemistry

Academic Year 2021

Student's Signature Patcharapom

Advisor's Signature [Signature]

Co-advisor's Signature [Signature]

## ACKNOWLEDGEMENTS

I would like to express appreciation to my thesis advisor Asst. Prof. Dr. Suwit Suthirakun and co-advisor Dr. Pussana Hirunsit for their patience, kind support, guidance, discussion, and encouragement throughout my thesis. I would like to acknowledge Dr. Anchalee Junkaew, Prof. Dr. Kritsana Sagarik, and Assoc. Prof. Rapee Utker for contributing as the thesis-examining committees. I am thankful to Asst. Prof. Dr. Suwit Suthirakun and Dr. Pussana Hirunsit for their help with the most parts of my thesis, useful suggestion and offering valuable comments. I also appreciate Lappawat Ngamwongwan for his help with some parts of my thesis and kind suggestion. I am grateful for the Research Network NANOTEC – SUT on Advanced Nanomaterials and Characterization (RNN), School of Chemistry, Suranaree University of Technology and One Research One Graduate (OROG) from Institute of Research and Development, Suranaree University of Technology for the scholarship and financial support during my doctor's program. I acknowledge NSTDA Supercomputer Center (ThaiSC), Institute of Science, Suranaree University of Technology, and Synchrotron Light Research Institute (SLRI) for computational resources. I would like to thank people from the School of Chemistry, Institute of Science, Suranaree University of Technology for their guidance and friendship. I am grateful to my friends in Computational Material Science and Catalysis (COMSCAT) Group for their love, kind support and encouragement throughout the period of this research. Finally, I would like to thank to my family for their love, kind support and encouragement.

Patcharaporn Khajondetchairit

# CONTENTS

	Page
ABSTRACT IN THAI.....	I
ABSTRACT IN ENGLISH.....	II
ACKNOWLEDGEMENTS.....	III
CONTENTS.....	IV
LIST OF TABLES.....	VIII
LIST OF FIGURES.....	IX
LIST OF ABBREVIATIONS.....	XVI
<b>CHAPTER</b>	
<b>I INTRODUCTION.....</b>	<b>1</b>
1.1 Background and significance.....	1
1.2 Scope and limitation.....	2
1.3 Organization of the thesis.....	3
1.4 References.....	4
<b>II LITERATURE REVIEW.....</b>	<b>8</b>
2.1 Overview of hydrogen storage .....	8
2.2 Chemical storage of hydrogen.....	10
2.3 Hydrogen storage in carbon-based material.....	12
2.3.1 Role of catalyst on the carbon-based material in the experimental study.....	13
2.3.2 Role of catalyst on the carbon-based material in the computational study.....	15
2.4 Hydrogen storage Mg-based hydrides.....	17
2.4.1 Role of catalyst on the carbon-based material in the experimental study.....	21

## CONTENTS (Continued)

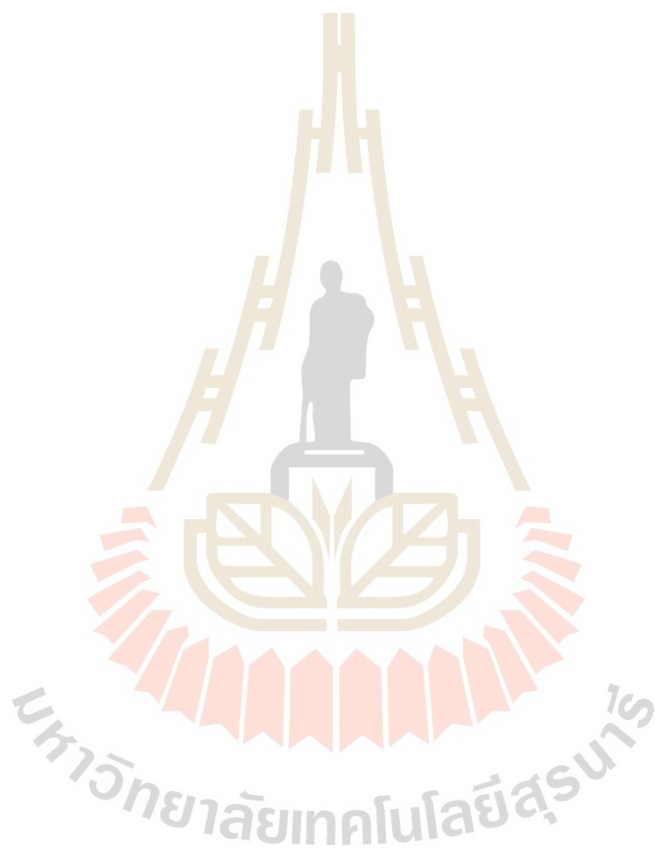
		Page
	2.4.2 Role of catalyst on the carbon-based material in the computational study.....	22
	2.5 References.....	28
<b>III</b>	<b>THEORETICAL AND COMPUTATIONAL APPROACHES.....</b>	<b>36</b>
	3.1 Schrödinger equation.....	36
	3.2 The Born-Oppenheimer approximation.....	37
	3.3 Density functional theory.....	37
	3.4 Approximations for the exchange-correlation functional .....	40
	3.5 Plane-wave basis set and pseudopotential approximation.....	40
	3.6 Climbing image nudged elastic band (CI-NEB) method.....	42
	3.7 Ab-initio molecular dynamic simulation (AIMD).....	43
	3.8 Summary of computational details.....	46
	3.9 References.....	47
<b>IV</b>	<b>DFT STUDY ON THE ROLE OF SYNERGISTIC EFFECT ON TRANSITION METALS OF Mg-BASED HYDROGEN STORAGE MATERIALS: MODEL DEVELOPMENTS.....</b>	<b>49</b>
	4.1 Introduction.....	49
	4.2 Computational details.....	50
	4.3 Model developments.....	51
	4.3.1 Mg(0001) surface model.....	51
	4.3.2 Mg <sub>2</sub> Ni(010) surface model.....	52
	4.3.3 V/Mg <sub>2</sub> Ni(010) surface model.....	54
	4.4 Conclusion.....	59
	4.5 References.....	59

## CONTENTS (Continued)

		Page
V	DFT STUDY ON THE ROLE OF SYNERGISTIC EFFECT ON TRANSITION METALS OF Mg-BASED HYDROGEN STORAGE MATERIALS: RESULTS AND DISCUSSION.....	63
	5.1 Introduction.....	63
	5.2 Behavior of H <sub>2</sub> adsorption.....	64
	5.3 Hydrogen diffusion on Mg(0001), Mg <sub>2</sub> Ni(010), and V/Mg <sub>2</sub> Ni(010) surfaces.....	71
	5.3.1 Hydrogen diffusion behavior on Mg(0001) surface.....	71
	5.3.2 Hydrogen diffusion behavior on Mg <sub>2</sub> Ni(010) surface.....	73
	5.3.3 Hydrogen diffusion behavior on V/Mg <sub>2</sub> Ni(010) surface.....	75
	5.4 Effect of hydrogen coverages.....	79
	5.5 References.....	87
VI	HYDROGEN ADSORPTION ON CARBON-BASED MATERIALS DECORATED WITH Ni NANOPARTICLES.....	90
	6.1 Introduction.....	91
	6.2 Computational details.....	91
	6.3 Hydrogen adsorption of O/N-rich hierarchical carbon scaffold decorated with Ni NPs.....	92
	6.3.1 Model development.....	92
	6.3.2 Hydrogen adsorption on the defect-free surface and the HCS surface model.....	94
	6.4 Ni-doped activated carbon nanofibers for storing hydrogen at ambient condition.....	96
	6.4.1 Model development of Ni supported pyrrolic graphene model.....	96
	6.4.2 Hydrogen adsorption on the defect-free surface and the HCS surface model.....	98
	6.5 Conclusion.....	100

## CONTENTS (Continued)

	Page
6.6 References.....	101
<b>VII CONCLUSION.....</b>	<b>104</b>
APPENDIX.....	106
CURRICULUM VITAE.....	110



## LIST OF TABLES

Table	Page
2.1	Advantages and disadvantages of different chemical storage approaches.....10
2.2	Experimentally results of the different Mg-TM systems in the hydrogenation phase and dehydrogenation phase were characterized XRD and XPS. The adsorption temperature and the hydrogenation capacity (wt%) were measured by automatic Sievert's apparatus at three different temperatures (°C).....21
4.1	Calculated surface energy of Mg <sub>2</sub> Ni(010) surface in the different ratios of Ni and Mg atoms on the topmost layer. Their geometrical structures are shown in Figure 4.2.....53
5.1	Calculated adsorption energies, E <sub>ads</sub> , (eV) for hydrogen adsorption on the Mg(0001), Mg <sub>2</sub> Ni(010), and V <sub>10</sub> /Mg <sub>2</sub> Ni(010) surfaces. Energy barrier of hydrogen dissociation (eV). Bader Charges of the total hydrogen atoms in (Q, H)  e . Adsorption site is nearest neighbors of hydrogen atoms.....65

## LIST OF FIGURES

Figure	Page
2.1	Renewable hydrogen cycle from renewable to application .....8
2.2	Classification of hydrogen storage method.....9
2.3	Potential energy surface of hydrogen physisorption and chemisorption as a function of distance from the adsorbent's surface.....11
2.4	The experimental results of hydrogen storage capacity and optimized pressure (a), and the variation of estimated isosteric heat of adsorption with adsorption amount (b) .....14
2.5	Illustration of spillover phenomena, based on the data.....15
2.6	Chemical structure of graphene oxide with functional groups. The green shaded and labeled as A: Epoxy bridges, B: hydroxy groups, C: pairwise carboxy groups, respectively.....16
2.7	Schematic of N-functionalized structure in carbon network.....17
2.8	Schematic represents the various metal hydrides materials, Operating conditions, and their hydrogen capacity.....18
2.9	Formation of metal hydride.....19
2.10	Illustration of the temperature-dependent of dissociation pressure of MgH <sub>2</sub> .....20
2.11	The illustration of TPD-MS cures of the different Mg-TM systems with a heating rate of 4 K min <sup>-1</sup> .....22
2.12	The relation between the energy barriers of hydrogen dissociation process (black) and hydrogen diffusion barriers (red) on pure Mg and TMs doped Mg surface and the calculated d-band center position.....23
2.13	The hydrogen diffusion coefficient for the sample milling time for 7 h. in benzene.....25

## LIST OF FIGURES (Continued)

Figure	Page
2.14	TEM image of the Mg-Ni-V nanoparticles [left], schematic diagram Proposed the catalytic effect of Mg <sub>2</sub> Ni and V [middle], and hydrogen adsorption cure of Mg-Ni-V nanocomposite.....26
2.15	Hydrogen dissociation and diffusion on the Ni (orange) and V (yellow) doped on Mg(0001) surface; (a) the illustration of hydrogen dissociation process, and (b) the energy profiles of hydrogen dissociation process (a) to (b), and the two diffusion paths from (b) to (c1) and (b) to (c2), and (b) .....27
3.1	Self-Consistent Field calculation (SCF) in DFT.....39
3.2	The schematic of saddle point obtained resulted from CINEB and NEB modification.....42
4.1	Optimized structure of Mg(0001) surface.....51
4.2	Optimized structure of Mg <sub>2</sub> Ni bulk.....52
4.3	Optimized geometries of the different ratios of Mg and Ni atoms on the topmost layers of Mg <sub>2</sub> Ni(010) surface.....53
4.4	Optimized geometries of Mg <sub>2</sub> Ni(010) surface.....54
4.5	Optimized geometries of isolated V <sub>n</sub> clusters: (a) from 8-15 atoms, and (b) Stability function, $\Delta^2E$ , with respect to the number of vanadium atoms ( $n = 9-14$ ).....55
4.6	Optimized structure of V <sub>10</sub> adsorbed on Mg <sub>2</sub> Ni(010) surface. The yellow ball labeled the vanadium active sites. (b) seven adsorption sites of V <sub>10</sub> on Mg <sub>2</sub> Ni(010) surface.....56
4.7	Optimized structures of V <sub>10</sub> decorated on Mg <sub>2</sub> Ni(010) where the bottom atoms of V <sub>10</sub> adsorbed on site 4 (atop-Ni atom) and site 7 (atop-Mg atom) on Mg <sub>2</sub> Ni(010) surface at different sites: E (edge), T (tip), and F (face). The blue, green, and gray shades represent Ni, Mg, and V atoms.....57

## LIST OF FIGURES (Continued)

Figure	Page
4.8 Optimized structures of $V_{10}$ decorated on $Mg_2Ni(010)$ where the bottom atoms of $V_{10}$ adsorbed on site 1-6 on $Mg_2Ni(010)$ surface at tip-on sites. The blue, green, and gray shades represent Ni, Mg, and V atoms. ....	58
4.9 Optimized structure of $V_{10}$ adsorbed on $Mg_2Ni(010)$ surface. (a) Side view, and (b) top view. The $V_{10}$ cluster fuse into the $Mg_2Ni(010)$ surface which can be distinguished as i) interface V atoms and ii) cluster V atoms which are marked in red and orange circles, respectively. The elements are colored as follows: green, Mg; blue, Ni; and gray, V.....	59
5.1 Atomic structures of $H_2$ on (a) molecular adsorption mode on Mg atop site, (b) dissociative adsorption on two Mg hollow sites, (c) Kubas adsorption on Ni atop site, and (d) dissociative adsorption on two Ni-Ni-Mg hollow sites. The labeling numbers show associated H-H, H-Mg, or H-Ni bond lengths in Angstrom.....	66
5.2 The relationship between the adsorption energies of hydrogen and (a) adsorption sites and (b) degrees of charge transfer from the surface to the adsorbed H atoms. The adsorption sites and modes are noted as the color and the shape of the marks, respectively. All illustrations of the atomic structures are generated by VESTA.....	68
5.3 Calculated projected density of states (PDOS) [left] and charge transfer to hydrogen [right] upon adsorption on $V_{10}/Mg_2Ni(010)$ surface at (a) V cluster, (b) interface, (c) hollow site on the surface, (d) atop of Mg, and (e) atop of Ni. The shaded areas in the PDOS represent the states contributed by H 1s (pink), V 3d (gray), Ni 3d (blue), and Mg 2p (green). The vertical dash line in the PDOS denotes the Fermi level ( $E_F$ ). The labeled numbers next to red arrows indicate	

## LIST OF FIGURES (Continued)

Figure	Page
numbers of charge transfer from substrate to adsorbed hydrogen atoms or molecule.....	69
5.4 Schematic illustrations of the most favorable diffusion paths for (a) surface and (b) subsurface diffusion on Mg(0001) surface with (c) their corresponding potential energy profiles. Labeled numbers in the brackets indicate diffusion barriers of the diffusion process.....	72
5.5 Schematic illustration of all considered surface diffusion paths and the corresponding diffusion barriers and reaction energies for surface diffusion. The diffusion barriers and relative energies are labeled as numbers with and without bracket, respectively. All energies are in eV.....	73
5.6 Schematic illustration of all considered diffusion paths and the corresponding diffusion barriers and reaction energies for subsurface diffusion. The diffusion barriers and relative energies are labeled as numbers with and without bracket, respectively. All energies are in eV. The Ni/Mg ratios indicate the nearest-neighbor environment of the H atom at different adsorption sites.....	74
5.7 Schematic illustration for (a) different surface diffusion paths (A-E) on the V/Mg <sub>2</sub> Ni(010) surface in top view and (b) the corresponding energy profiles. Labeled numbers indicate the diffusion barriers in eV.....	76
5.8 Schematic illustrations of (a) two different diffusion paths, path A (left) and B (right), from V cluster to under-subsurface layer of the V/Mg <sub>2</sub> Ni system with (b) the corresponding potential energy profiles. Labeled numbers with and without brackets indicate diffusion barriers and relative energies, respectively.....	77

## LIST OF FIGURES (Continued)

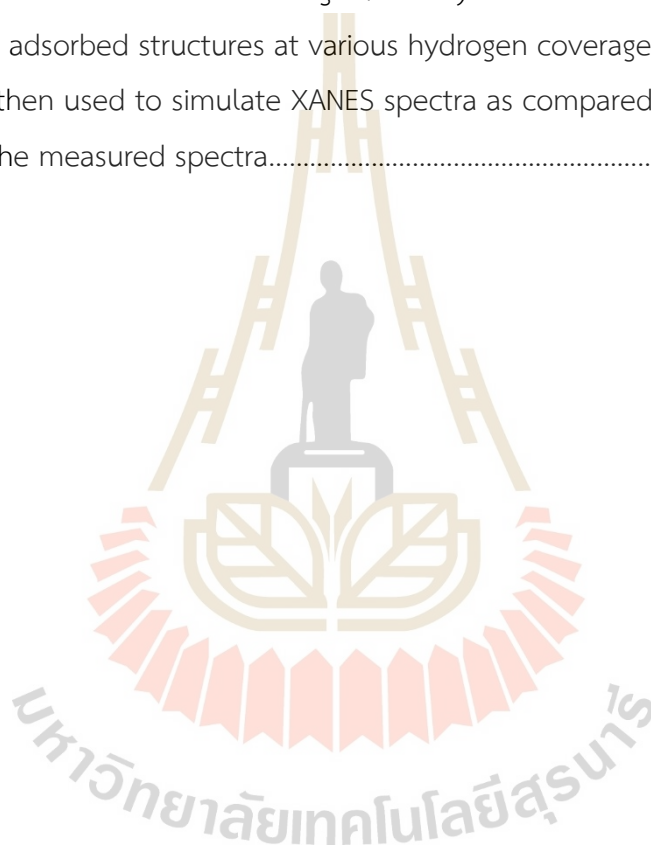
Figure	Page
5.9 The crystal structure of (side view) diffused H atom jump from the subsurface [left] site to under subsurface diffusion [right] into the bulk $Mg_2Ni$ . Only structures at the region near the subsurface and under subsurface sites are shown for clarity. The H-Mg and H-Ni bond lengths surrounded the interstitial site which corresponding to the labelled numbers in crystal structure. The elements are colored as follows: green, Mg; blue, Ni; pink, H.....	78
5.10 The AIMD results involve 40 $H_2$ in the system at 30 ps (300 K); a) $Mg(0001)$ , b) $Mg_2Ni(010)$ , and $V_{10}/Mg_2Ni(010)$ surface. Green, Mg; blue, Ni; pink, H; gray, V.....	80
5.11 Optimized structures of low-energy configurations obtained from the AIMD simulations for high hydrogen coverage (1 ML) on $Mg_2Ni(010)$ surface including 16 adsorbed H atoms. The subsurface H atoms are marked with red circles.....	81
5.12 Energy profiles of the most favorable subsurface diffusion on $Mg_2Ni(010)$ surface at low and high hydrogen coverage. Only structures at the region near the subsurface and under subsurface sites are shown for clarity. The elements are colored as follows: green, Mg; blue, Ni; pink, H.....	82
5.13 Optimized structures of low-energy configurations obtained from the AIMD simulations for high hydrogen coverage (1 ML) on $V/Mg_2Ni$ system containing 20 adsorbed H atoms. The subsurface H atoms are marked with red circles.....	83

## LIST OF FIGURES (Continued)

Figure	Page
5.14 Schematic illustrations of a) hydrogen diffusion from V cluster to under-surface layer of the V/Mg <sub>2</sub> Ni system at high hydrogen coverage (1 ML) with b) the corresponding potential energy profiles at low and high coverages. Labeled numbers with and without brackets indicate diffusion barriers and relative energies, respectively.....	84
6.1 The optimized structures of the Ni <sub>13</sub> cluster supported on pristine a) graphene and b) defected graphene. The calculated cluster-support binding energies, E <sub>b</sub> , is labelled. The numbers of electron gain/loss by each species are indicated.....	93
6.2 The optimized structures of H <sub>2</sub> adsorbed structures are illustrated on pristine a) graphene and b) defected graphene. respectively. The calculated H <sub>2</sub> adsorption energy per H <sub>2</sub> molecule, E <sub>ads</sub> , is labelled.....	95
6.3 The simulate XANES spectra of Ni K-edge of the Ni <sub>13</sub> cluster supported on defect graphene in the absence (Figure 6.1) and presence of hydrogen coverage (Figure 6.2).....	95
6.4 The optimized structures of Ni <sub>13</sub> cluster supported on pyrrolic graphene in the absence.....	97
6.5 The electron transfer is schematically depicted by the colors of each atom where the positive and negative values describe electron gains and losses, respectively. The labelled numbers represent the total number of electrons gain/loss by each atomic species.....	98
6.6 The optimized structures H <sub>2</sub> adsorbed on Ni <sub>13</sub> cluster supported on pyrrolic graphene in the absence.....	99

## LIST OF FIGURES (Continued)

Figure		Page
6.7	The electron transfer is schematically depicted by the colors of each atom where the positive and negative values describe electron gains and losses, respectively. The labelled numbers represent the total number of electrons gain/loss by each atomic species.....	99
6.8	The H adsorbed structures at various hydrogen coverages were then used to simulate XANES spectra as compared with the measured spectra.....	101



## LIST OF ABBREVIATIONS

DOE	= US Department of Energy
TMs	= Transition metals
XRD	= X-ray diffraction
XPS	= X-ray Photoelectron spectroscopy
TPD-MS	= Temperature Programmed Desorption Mass-Spectrometry
DFT	= Density functional theory
TEM	= Transmission electron microscopy
MA	= Wet mechanical alloy
NPs	= Nanoparticles
AIMD	= Ab-initio molecular dynamic simulations
VASP	= Vienna ab-initio simulation package
PDOS	= Projected density of states
CI-NEB	= Climbing image nudged elastic band
TS	= Transition state
ps	= Pico second
fs	= Femto second
n	= Number of atoms
Q	= Bader Charges of the total hydrogen atoms
$E_a$	= Energy barrier
$E_{ads}$	= Adsorption energy
PBE	= Perdew–Burke–Ernzerhof functional
ML	= Monolayer

# CHAPTER I

## INTRODUCTION

### 1.1 Introduction

Over the last decade, hydrogen has been one of the most promising candidates as a future energy carrier owing to its high energy density, renewability, and environmental friendliness (Jain *et al.*, 2010; Sadhasivam *et al.*, 2017). However, hydrogen technology is still suffering from significant storage and transportation challenges (El Khatabi *et al.*, 2018; El Khatabi *et al.*, 2016). High-pressure storage in tanks, where hydrogen is compressed into liquid form at low temperature (Graetz, 2012; Mohan *et al.*, 2019), hinders the actual application of hydrogen energy due to a danger of gas compression and substantial cost to liquefy hydrogen (Chen *et al.*, 2018; Schüth *et al.*, 2004). To effectively use hydrogen as an energy carrier, safe hydrogen storage systems with high efficiency are necessary. To meet these critical goals, many efforts have been made to develop alternative materials based on the chemical bonding between the solid material and hydrogen atoms. Solid-state materials can be classified into two broad categories, namely, (i) physical adsorption and (ii) chemical absorption (Lim *et al.*, 2010).

The physical adsorption via van der Waals interaction between hydrogen and substrates, include carbon-based material and metal-organic framework (MOF). One of the potential types of materials in physical adsorption is carbon-based material. Carbon-based materials have been extensively studied for their ability to adsorb and release hydrogen at a moderate temperature (Cracknell, 2001; Dillon *et al.*, 1997). However, only a small amount of hydrogen can be adsorbed even at a pressure of 90 bar in pure carbon material (Lim *et al.*, 2010). In the chemical absorption, several light metals and alloys are of interest to store hydrogen in the forms of chemical compounds, such as LiH, MgH<sub>2</sub>, NaH, LiBH<sub>4</sub>, and NaAlH<sub>4</sub> (Chen *et al.*, 2016; Mohan *et al.*, 2019; Schüth *et al.*, 2004). Among these materials, Mg is one of the most promising

candidates for hydrogen storage (Sadhasivam *et al.*, 2017) because it has a high gravimetric hydrogen density of 7.6 wt%. However, Mg-based material cannot be used onboard due to their high desorption temperatures of 623-673 K, inhibiting its practical application for vehicles (Crivello *et al.*, 2016; Zhang *et al.*, 2019; Zhang *et al.*, 2018).

As a result, many works aimed to improve the hydrogen capability and the kinetics of hydrogenation and dehydrogenation of solid-stage material, including carbon material and metal hydrides via alloying, or doping with transition metals (Plerdsranoy *et al.*, 2021; Thaweelap *et al.*, 2021; Xiubo *et al.*, 2018). The improvement of alternative hydrogen storage material is of great interest to study the role of transition metal catalysts and is the topic of this thesis.

## 1.2 Scope and limitations

As mentioned above, the alternative hydrogen storage materials as carbon-based and Mg-based materials, cannot be used in practical application due to the requirements for a storage property (Boateng and Chen, 2020; Zhang *et al.*, 2019). The desirable hydrogen storage should process the following characteristic: safe hydrogen storage systems with high efficiency (5.5 wt%), moderate operating temperature (298 – 393 K), fast kinetics, low cost, excellent reversibility, and low toxicity. The US Department of Energy system set the benchmark targets of material efficiency for 2025 (Allendorf *et al.*, 2018; Banerjee *et al.*, 2008; Jain *et al.*, 2010; Mahant *et al.*, 2021).

Both experimental and theoretical investigations reported that adding transition metals (TMs) such as V (Liu *et al.*, 2011), Ni (Hong *et al.*, 2018; Plerdsranoy *et al.*, 2021; Thaweelap *et al.*, 2021; Zou *et al.*, 2015), enhances the hydrogen absorption/desorption processes and the hydrogen capability. For example, it has been experimentally shown that small amounts of transition metal catalysts may improve the capacity and the reaction kinetic with the hydrogen storage materials (Emami *et al.*, 2016; Sakamoto and Atsumi, 2019; Xiubo *et al.*, 2018). Therefore, in this work, the catalytic role of TMs as Ni and V impurities has been assessed by a computational study based on density functional theory (DFT). The calculation employed the model of the V cluster supported on the Mg<sub>2</sub>Ni alloy surface to represent the experimentally observed phases of V and Ni catalysts on the Mg-based

hydrogen storage materials. The DFT calculations and ab-initio molecular dynamic (AIMD) simulations were applied to study the catalytic roles of Ni and V for hydrogen adsorption, hydrogen dissociation and diffusion behavior. These processes were studied on the Mg(0001), Mg<sub>2</sub>Ni(010), and V cluster supported on Mg<sub>2</sub>Ni surfaces. We also analyzed the projected density of state (PDOS) and the charge difference between the adsorbed H atoms and their adsorbents. The outcome provides a theoretical insight into how V and Ni catalysts enhance the hydrogen sorption processes. In addition, to consider the effect of high hydrogen pressure at hydrogenation conditions, the effect of high hydrogen coverages was examined on various diffusion processes. Furthermore, the enhancements of hydrogen adsorption performances of Ni-doped on carbon-based materials are examined. First-principles calculations based on the DFT method are employed to study the interactions between Ni cluster and surfaces. The behavior of H<sub>2</sub> adsorption and their structural are studied and analyzed in the electronic properties of nitrogen and oxygen heteroatoms as evidenced from experimental studies (Plerdsranoy *et al.*, 2021; Thaweelap *et al.*, 2021).

### 1.3 Organization of the thesis

This introduction is followed by chapter II, “Literature reviews”, which summarize the basic knowledge of hydrogen storage material and review their performance. The primary motivation of this work is also proposed in the chapter which points out why we want to study the role of transition metal catalysts on the different hydrogen storage materials in experimental and computational studies.

Chapter III gives a detailed description of the theoretical and computational approaches throughout this thesis. This chapter contains the short methods section of the specific methodology for further information in chapters IV and V.

Chapter IV deals with the geometry optimization of difference surfaces, including Mg(0001), Mg<sub>2</sub>Ni(010), and the V cluster supported on Mg<sub>2</sub>Ni surface.

Chapter V, the DFT calculations and ab-initio molecular dynamic (AIMD) simulations were applied to study the role of synergetic effects of Ni and V for hydrogen adsorption, hydrogen spillover, and surface and subsurface diffusion. The effect of hydrogen coverage was also discussed in this section.

Chapter VI discusses the role of Ni adding in the carbon nanomaterial, involving the geometry optimization, electronic structure, and the charge difference between adsorbed gas and host materials. This chapter is motivated by an experimental study from Plerdsranoy *et al.*, and Thaweelap *et al.*, (Plerdsranoy *et al.*, 2021; Thaweelap *et al.*, 2021). The computational results reported that adding Ni to the carbon materials can improve the hydrogen storage performance, according to the experiment observations.

Finally, chapter VII summarizes how the computational tools can be used to better understand the role of transition metals catalysts in improving hydrogen storage material performance. The insight obtained from the theoretical and guidance on using a combination of TM catalysts to improve the performance of hydrogen storage materials.

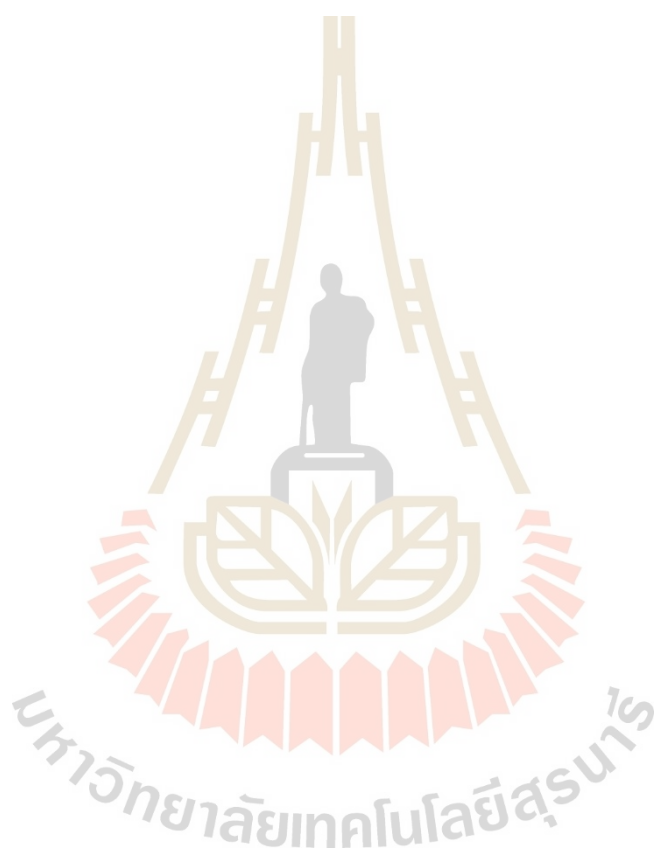
#### 1.4 References

- Allendorf, M. D., Hulvey, Z., Gennett, T., Ahmed, A., Autrey, T., Camp, J., Seon Cho, E., Furukawa, H., Haranczyk, M., Head-Gordon, M., Jeong, S., Karkamkar, A., Liu, D.-J., Long, J. R., Meihaus, K. R., Nayyar, I. H., Nazarov, R., Siegel, D. J., Stavila, V., Urban, J. J., Veccham, S. P., and Wood, B. C. (2018). An Assessment of Strategies for the Development of Solid-State Adsorbents for Vehicular Hydrogen Storage. *Energy Environ. Sci.* *11*, 2784.
- Banerjee, S., Pillai, C. G. S., and Majumder, C. (2008). First-Principles Study of the H<sub>2</sub> Interaction With Transition Metal (Ti, V, Ni) Doped Mg(0001) Surface: Implications for H-Storage Materials. *J. Chem. Phys.* *129*, 174703.
- Boateng, E. and Chen, A. (2020). Recent Advances in Nanomaterial-Based Solid-State Hydrogen Storage. *Mater. Today Adv.* *6*, 100022.
- Chen, H., Yu, H., Zhang, Q., Liu, B., Liu, P., Zhou, X., Han, Z., and Zhou, S. (2016). Enhancement in Dehydrogenating Performance of Magnesium Hydride by Iron Incorporation: A Combined Experimental and Theoretical Investigation. *J. Power Sources.* *322*, 179.
- Chen, Y., Dai, J., and Song, Y. (2018). Stability and Hydrogen Adsorption Properties of Mg/Mg<sub>2</sub>Ni Interface: A First Principles Study. *Int. J. Hydrog. Energy.* *43*, 16598.

- Cracknell, R. F. (2001). Molecular simulation of hydrogen adsorption in graphitic nanofibres. *Phys. Chem. Chem. Phys.* **3**, 2091.
- Crivello, J. C., Denys, R. V., Dornheim, M., Felderhoff, M., Grant, D. M., Huot, J., Jensen, T. R., de Jongh, P., Latroche, M., Walker, G. S., Webb, C. J., and Yartys, V. A. (2016). Mg-Based Compounds for Hydrogen and Energy Storage. *Appl. Phys. A*. **122**, 85.
- Dillon, A. C., Jones, K. M., Bekkedahl, T. A., Kiang, C. H., Bethune, D. S., and Heben, M. J. (1997). Storage of hydrogen in single-walled carbon nanotubes. *Nature*. **386**, 377.
- El Khatabi, M., Bhihi, M., Lakhal, M., Abdellaoui, M., Benyoussef, A., El Kenz, A., and Loulidi, M. (2018). Enhanced Hydrogen Sorption Kinetics of Co-Doped MgH<sub>2</sub> Hydrides. *Comput. Mater. Sci.* **152**, 192.
- El Khatabi, M., Bhihi, M., Naji, S., Labrim, H., Benyoussef, A., El Kenz, A., and Loulidi, M. (2016). Study of Doping Effects with 3d and 4d-Transition Metals on the Hydrogen Storage Properties of MgH<sub>2</sub>. *Int. J. Hydrog. Energy*. **41**, 4712.
- Emami, H., Edalati, K., Staykov, A., Hongo, T., Iwaoka, H., Horita, Z., and Akiba, E. (2016). Solid-state reactions and hydrogen storage in magnesium mixed with various elements by high-pressure torsion: experiments and first-principles calculations. *RSC Adv.* **6**, 11665.
- Graetz, J. (2012). Metastable Metal Hydrides for Hydrogen Storage. *ISRN mater. sci.* **2012**, 863025.
- Hong, S. H., Kwak, Y. J., and Song, M. Y. (2018). Enhancement of the hydrogen-storage characteristics of Mg by adding Mg<sub>2</sub>Ni and Ni to MgH<sub>2</sub> via high energy ball milling in hydrogen atmosphere. *Korean J. Met. Mater.* **56**, 59.
- Jain, I. P., Lal, C., and Jain, A. (2010). Hydrogen Storage in Mg: A Most Promising Material. *Int. J. Hydrog. Energy*. **35**, 5133.
- Lim, K. L., Kazemian, H., Yaakob, Z., and Daud, W. R. W. (2010). Solid-state Materials and Methods for Hydrogen Storage: A Critical Review. *Chem. Eng. Technol.* **33**, 213.

- Liu, T., Zhang, T., Qin, C., Zhu, M., and Li, X. (2011). Improved hydrogen storage properties of Mg–V nanoparticles prepared by hydrogen plasma–metal reaction. *J. Power Sources*. 196, 9599.
- Mahant, B., Linga, P., and Kumar, R. (2021). Hydrogen Economy and Role of Hythane as a Bridging Solution: A Perspective Review. *Energy & Fuels*. 35, 15424.
- Mohan, M., Sharma, V. K., Kumar, E. A., and Gayathri, V. (2019). Hydrogen Storage in Carbon Materials—A Review. *J. Energy Storage*. 1, 35.
- Plerdsranoy, P., Thaweelap, N., Poo-arporn, Y., Khajondetchairit, P., Suthirakun, S., Fongkaew, I., Chanlek, N., Utke, O., Pangon, A., and Utke, R. (2021). Hydrogen adsorption of O/N-rich hierarchical carbon scaffold decorated with Ni nanoparticles: Experimental and computational studies. *Int. J. Hydrog. Energy*. 46, 5427.
- Sadhasivam, T., Kim, H.-T., Jung, S., Roh, S.-H., Park, J.-H., and Jung, H.-Y. (2017). Dimensional effects of nanostructured Mg/MgH<sub>2</sub> for hydrogen storage applications: A review. *Renew. Sust. Energ. Rev.* 72, 523.
- Sakamoto, T. and Atsumi, H. (2019). Hydrogen absorption/desorption characteristics of Mg-V-Ni hydrogen storage alloys. *Fusion Eng. Des.* 138, 6.
- Schüth, F., Bogdanović, B., and Felderhoff, M. (2004). Light Metal Hydrides and Complex Hydrides for Hydrogen Storage. *Chem. Commun.* 2249.
- Thaweelap, N., Plerdsranoy, P., Poo-arporn, Y., Khajondetchairit, P., Suthirakun, S., Fongkaew, I., Hirunsit, P., Chanlek, N., Utke, O., Pangon, A., and Utke, R. (2021). Ni-doped activated carbon nanofibers for storing hydrogen at ambient temperature: Experiments and computations. *Fuel*. 288, 119608.
- Xiubo, X., Ming, C., Peng, L., Jiayang, S., and Tong, L. (2018). Synergistic Catalytic Effects of the Ni and V Nanoparticles on the Hydrogen Storage Properties of Mg-Ni-V Nanocomposite. *Chem. Eng.* 347, 145.
- Zhang, J., Li, Z., Wu, Y., Guo, X., Ye, J., Yuan, B., Wang, S., and Jiang, L. (2019). Recent advances on the thermal destabilization of Mg-based hydrogen storage materials. *RSC Adv.* 9, 408.
- Zhang, J., Yan, S., and Qu, H. (2018). Recent progress in magnesium hydride modified through catalysis and nanoconfinement. *Int. J. Hydrog. Energy*. 43, 1545.

Zou, J., Long, S., Chen, X., Zeng, X., and Ding, W. (2015). Preparation and hydrogen sorption properties of a Ni decorated Mg based Mg@Ni nano-composite. *Int. J. Hydrog. Energy.* 40, 1820.



## CHAPTER II

### LITERATURE REVIEW

#### 2.1 Overview of hydrogen storage

Nowadays, CO<sub>2</sub> emission from fossil fuel combustion indicate the environmental impact and global warming effect that has led to the development of alternative energy systems. Sustainable energy is the most promising candidate owing to being clean, available, flexible, and cost-efficient (Aguey-Zinsou and Ares-Fernández, 2010; Jain, 2010). Hydrogen has been identified as a new source of energy for transportation, utilization. (Sadhasivam *et al.*, 2017). It can be found and produced from many different sources, for example, oil, natural gas, biomass, and water (Dimanta *et al.*, 2019), as shown in Figure 2.1.

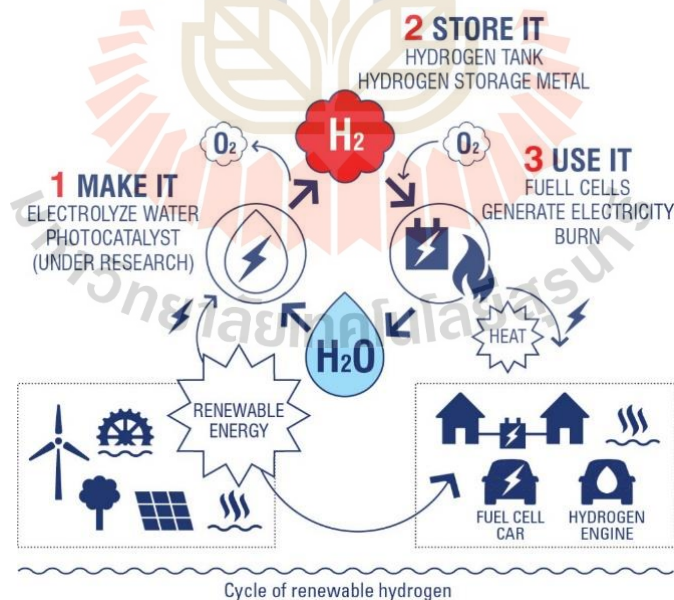


**Figure 2.1** Renewable hydrogen cycle from renewable to application modified from (<http://hydroville.be>).

With all these good qualities, hydrogen energy is likely a key to the global energy revolution (Jain *et al.*, 2010). However, storing hydrogen is not conveniently obtainable for several applications. Hydrogen technology suffers from the major challenge of its storage and utilization (El Khatabi *et al.*, 2018; El Khatabi *et al.*, 2016). In the past, there were two conventional methods for on-board hydrogen storage:

- (i) Compressed gaseous hydrogen (35-70 MPa and room temperature)
- (ii) Cryogenic or liquid hydrogen at 20 to 30 K and 0.5-1 MPa

Since hydrogen has a higher energy density by mass, its volume is inferior. Thus, it requires a more extensive or heavier storage vehicle than the smaller storage tank needed to deliver the same amount of energy. The volumetric storage density of both systems is relatively low in the automotive industry. In addition, high-pressure storage in tanks, where hydrogen is compressed into liquid form at low temperature (Graetz, 2012; Mohan *et al.*, 2019), hinders the actual application of hydrogen energy due to a danger of gas compression and substantial cost to liquefy hydrogen (Chen *et al.*, 2018; Schüth *et al.*, 2004). Various methods have been developed to store sufficient hydrogen at a lower cost and higher energy density. Most research on hydrogen storage has mainly focused on storing hydrogen in chemical storage that can maintain hydrogen in portable usage, as shown in Figure 2.2.

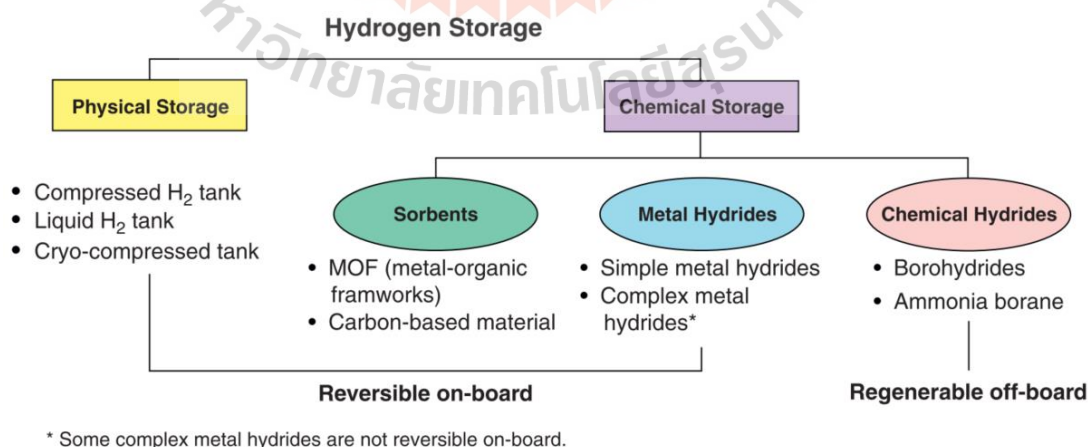


**Figure 2.2** Classification of hydrogen storage method (Hwang and Varma, 2014).

## 2.2 Chemical storage of hydrogen

To define the effective use of hydrogen in high efficiency and safe hydrogen storage systems, hydrogen adsorption on material with high specific surface area and chemically bonded is becoming attractive. Chemical storages have been developed, such as sorbents, metal hydrides, and chemical hydrides (Chen *et al.*, 2016), as shown in Figure 2.2. The advantages and disadvantages for each approach are summarized in Table 2.1.

**Table 2.1** Advantages and disadvantages of different chemical storage approaches.

H <sub>2</sub> storage system	Advantages	Disadvantages	Compound
Sorbent	- Reversible on-board	- Low volumetric density - Low operating temperature for H <sub>2</sub> uptake	- Carbon-based material - Metal-organic framework (MOF)
Metal hydrides	- Good volumetric capacity - Reversible on-board	- High adsorption and desorption temperature	- LiH - NaH - CaH <sub>2</sub> - MgH <sub>2</sub>
Chemical metal hydrides	- Gravimetric capacity is relatively high. (4.5-10.8 wt%)	- Release hydrogen under relatively mild operating conditions - Dehydrogenation reactions are irreversible	- LiBH <sub>4</sub> - NaBH <sub>4</sub> - NH <sub>3</sub> BH <sub>3</sub>
Chemical hydrides	- Release hydrogen reversibly at modest temperature (150 °C)	- Low gravimetric capacity (1.4 wt%) - Costly	- LiAlH <sub>4</sub> - NaAlH <sub>4</sub> - LaNi <sub>5</sub> H <sub>6</sub>

To produce the alternative in chemical storages, hydrogen gas can be stored in the form of hydrogen molecules or atoms that can react with other elements with the formation of bond with host materials. Meanwhile, many efforts have been made to propose two hydrogen storage classifications depending on the interaction between  $H_2$  and the existing adsorbents: (i) adsorption of hydrogen molecules on surfaces, namely physisorption, and (ii) hydrogen atoms forming chemical bonds, namely chemisorption. The physisorption is mainly found on the carbon-based material, caused by weak Van der Waals interaction. This energy minimum corresponds to the binding energy in a range of 0.01-0.1 eV (Felderhoff *et al.*, 2007; Nagar *et al.*, 2017). This potential energy curve shows the barrierless hydrogen approaching the surface, as shown in Figure 2.3. In the chemisorption, the potential energy curve shows that the one at the nearest distance between  $H_2$  and the adsorbent is the  $H_2$  chemisorption as hydride form corresponding binding energy of 0.5 to 1.0 eV under various conditions (Sun *et al.*, 2018)

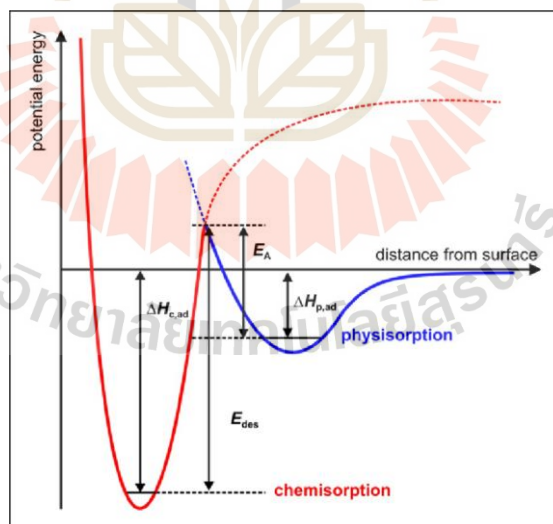


**Figure 2.3** Potential energy surface of hydrogen physisorption and chemisorption as a function of distance from the adsorbent's surface (Hirscher and Panella, 2005).

As mentioned above, the storing hydrogen in solid-state materials exhibited a different binding energy range of chemical bonded. However, these materials still have some drawbacks that cannot meet all the criteria required. The next section discusses challenges of each solid-state material that can be used to store hydrogen. The United States Department of Energy (U.S. DOE) set the requirement of the current hydrogen storage technology for different materials as follows:

- (i) cost,
- (ii) weight and volume,
- (iii) efficiency,
- (iv) reversibility, and
- (v) hydrogen capacity (Lim *et al.*, 2010).

For practical application, many efforts have been made to develop the potential hydrogen storage to meet the goal set by U.S. DOE. For the longer term, solid-state hydrogen storage materials such as high surface area sorbents and hydrides offer potential.

### 2.3 Hydrogen storage in carbon-based materials

Materials investigated for hydrogen physisorption are mainly carbon-based materials owing to their high surface area and porosity. As mentioned previously, the hydrogen adsorption enthalpy is small, where the H-H bond of adsorbed gas remains the same as hydrogen gas molecules. Therefore, this material involves the fast kinetic with high hydrogen uptake via physisorption. Various carbon-based materials have been extensively studied as the hydrogen storage media, including activated carbon (Rossetti *et al.*, 2015; Zhao *et al.*, 2019; Zieliński *et al.*, 2007), carbon nanotube (Akbarzadeh *et al.*, 2019; Banerjee *et al.*, 2015; Dillon *et al.*, 1997), or graphene (Li *et al.*, 2014; López *et al.*, 2014; Ma *et al.*, 2014). The hydrogen storage capacity dominates by the surface area and the porosity in the material. To improve the hydrogen uptake capacity, the surface area of carbon-based material should be increased with multiple adsorption layers. The gravimetric H<sub>2</sub> uptake at 77 K and 35 bar is about 1 wt% per

500 m<sup>2</sup>g<sup>-1</sup> (Hirscher and Panella, 2005). These materials cannot meet the target goal from U.S. DOE. For this reason, the modifications through doping with TMs, defect formation, or heteroatoms substitution are effective ways to enhance the H<sub>2</sub> interaction and adsorption sites on the adsorbents.

### 2.3.1 Role of catalyst on the carbon-based material in the experimental study

The DOE target proposed the hydrogen adsorption enthalpy between 0.1–0.5 eV under ambient conditions. Carbon-based materials suffer from a low storage capacity according to the van der Waals interactions (the binding energy in a range of 0.01-0.1 eV) between adsorbed H<sub>2</sub> molecule and adsorbent. Many efforts have been made to overcome this drawback which adds the TMs as a catalyst. To improve the interaction and increase the adsorption sites, the most common metal dopant incorporated into the adsorbent material are Ni (Li *et al.*, 2014; Plerdsranoy *et al.*, 2021; Thaweelap *et al.*, 2021), Pt (Divya and Ramaprabhu, 2014; Jin *et al.*, 2015), and Pd (López *et al.*, 2014; Ma *et al.*, 2014; Rangel and Sansores, 2014). For example, the hydrogen adsorption capacity enhanced with Pt loaded on hydrogen exfoliate graphene sheets (Pt-HEG) to 1.4 wt% in comparison to pristine hydrogen exfoliate graphene (HEG) (0.5 wt%) at 2 MPa under ambient condition (Divya and Ramaprabhu, 2014). To measure the change of enthalpy when the H<sub>2</sub> molecule became to adsorbate phase (Tun and Chen, 2021), they calculated the isosteric heat of adsorption ( $\Delta H_{\text{ads}}$ ) using the equation in following:

$$|\Delta H_{\text{ads}}| = -R \left( \frac{\partial \ln P}{\partial \left( \frac{1}{T} \right)} \right) \quad (2.1)$$

Where  $R$  is the ideal gas constant.  $\Delta H_{\text{ads}}$  can be measured from experimental adsorption isotherm at multiple temperatures as shown in Figure 2.4(a)

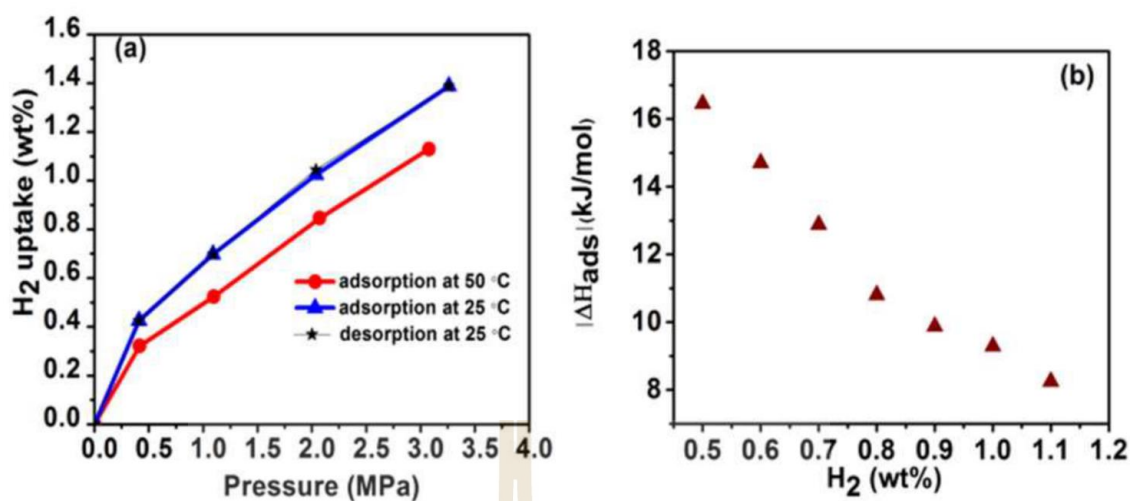


**Figure 2.4** The experimental results of hydrogen storage capacity and optimized pressure (a), and the variation of estimated isosteric heat of adsorption with adsorption amount (b) (Divya and Ramaprabhu, 2014).

Figure 2.4 (b) shows that Pt loaded on hydrogen exfoliate graphene sheets (Pt-HEG) has an isosteric heat of adsorption in the range of 8-17 kJ/mol which higher than that of pristine HEG (6.03-6.78 kJ/mol). They also proposed that hydrogen can spillover from Pt particle to the adsorbent which is caused to enhance the storage capacity at room temperature (Divya and Ramaprabhu, 2014). The spillover effect has been widely used to describe the enhancement of hydrogen storage capacity, where hydrogen molecules were started to adsorb or dissociate on the TMs particles and were further spilled onto different adsorption sites of the carbon-based materials as shown in Figure 2.5

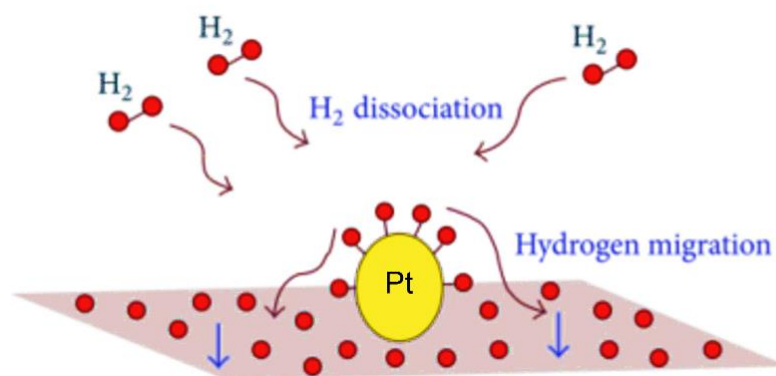


**Figure 2.5** Illustration of spillover phenomena, based on the data from (Zacharia and Rather, 2015).

### 2.3.2 Role of catalyst on the carbon-based material in the computational study

Many computational studies have been studied the mechanism of hydrogen atom spillover from TMs catalyzed sites to the graphene as a carbon substrate (Cheng *et al.*, 2008; Psofogiannakis and Froudakis, 2009; Sihag *et al.*, 2019). Nevertheless, the Pt-doped graphite was studied by DFT-GGA (PW91) computations. They found that dissociated H atoms must overcome a significant energy barrier ( $> 2.17$  eV) to diffuse from Pt cluster to graphite surface. On the other hand, they also suggest that the other important factor will occur in the experiment to increase the hydrogen storage via the oxygen functionalized, the formation of defect or the attraction of heteroatoms from the carbon precursor (Cheng *et al.*, 2008; Nair *et al.*, 2015).

The imperfect surface was often found as an acid functionalization in the surface functionally groups like epoxy, hydroxyl, carbonyl, etc., on/in the defect or edges on the carbon-based materials as graphene oxide (Georgakilas *et al.*, 2012), as shown in Figure 2.6. The chemical modification of carbon-based materials has been investigated to increase the formation of defects and local dipole moment molecules. Among these TMs dopant, Ni is suitable for doping into the adsorbent owing to its low

cost, availability, good performance, and abundance. In a recent study, the Ni nanoparticle was decorated on carbon-based material as the hierarchical porous structure with multi-layer pores, and high specific area. The obtained experimental results demonstrate that this material can uptake hydrogen of 4.22 wt% at 77 K under the pressure of 5 bar. According to the XPS spectra, the formation of the Ni-O-C bond can improve the affinity of Ni nanoparticles to graphene substrate. They also proposed that the enhanced hydrogen capacity is due to the distributed Ni NPs on/in the stacking of graphene sheets (Liu *et al.*, 2018).

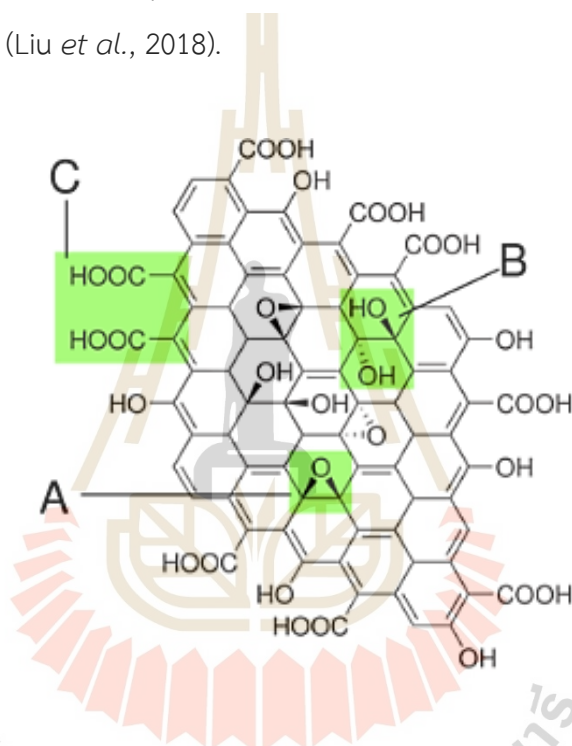


**Figure 2.6** Chemical structure of graphene oxide with functional groups. The green shaded and labeled as A: Epoxy bridges, B: hydroxy groups, C: pairwise carboxy groups, respectively (Notarianni *et al.*, 2016).

Moreover, the carbon support was attached by various heteroatoms (i.e., oxygen, sulfur, nitrogen, phosphorus, and boron) from the different carbon resources. Based on theoretically and experimentally studies, the combination of doping transition metals and carbon-based materials modification have been reported that the increased hydrogen uptake has been correlated with the good dispersion of TMs particles (i.e., Ni, Pt, Cu, Pd) on the adsorbent (Banerjee *et al.*, 2015; Rossetti *et al.*,

2015). For example, the Pt and Pd nanoparticles on N-doped activated carbon (NAC) and GP were achieved to present the higher enhancement of hydrogen uptake than those of pristine activated carbon (AC) or GP without heteroatoms. They proposed that high dispersion of nanoparticles and strong interaction between metals particle and N-dope support (Parambath *et al.*, 2012; Zhao *et al.*, 2019). The XPS analysis found that the various types of N-functionalized carbon have occurred in the carbon network of GP as depicted in Figure 2.7. The pyridinic and pyrrolic defects were observed in the carbon lattice (Rangel *et al.*, 2016; Zhao *et al.*, 2019).

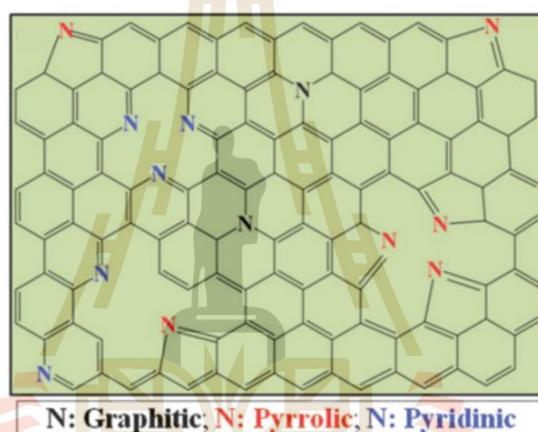


**Figure 2.7** Schematic of N-functionalized structure in carbon network (Zhao *et al.*, 2019).

## 2.4 Hydrogen storage in Mg-based hydrides

Various metals and alloys can reversibly absorb hydrogen via direct reaction of the metal with hydrogen gas. Hydrogen storage in solid-state material can store hydrogen at low pressure and ambient temperature. By comparing the composites based on alloys with different stoichiometries can be divided into metal-based hydride and complex hydrides, as mentioned in previously (Mohan *et al.*, 2019; Schüth *et al.*, 2004). The metal-based hydrides are considered an appropriate category because  $\text{LaNi}_5$  can release hydrogen at ambient conditions, but they can store the lowest density of hydrogen (Abd.Khalim Khafidz *et al.*, 2016). The highest volumetric and gravimetric

densities of hydrogen were observed in complex hydrides (e.g.,  $\text{NaBH}_4$ , and  $\text{LiBH}_4$ ). Unfortunately, this capability is poor kinetics and high desorption temperature (Figure 2.8).

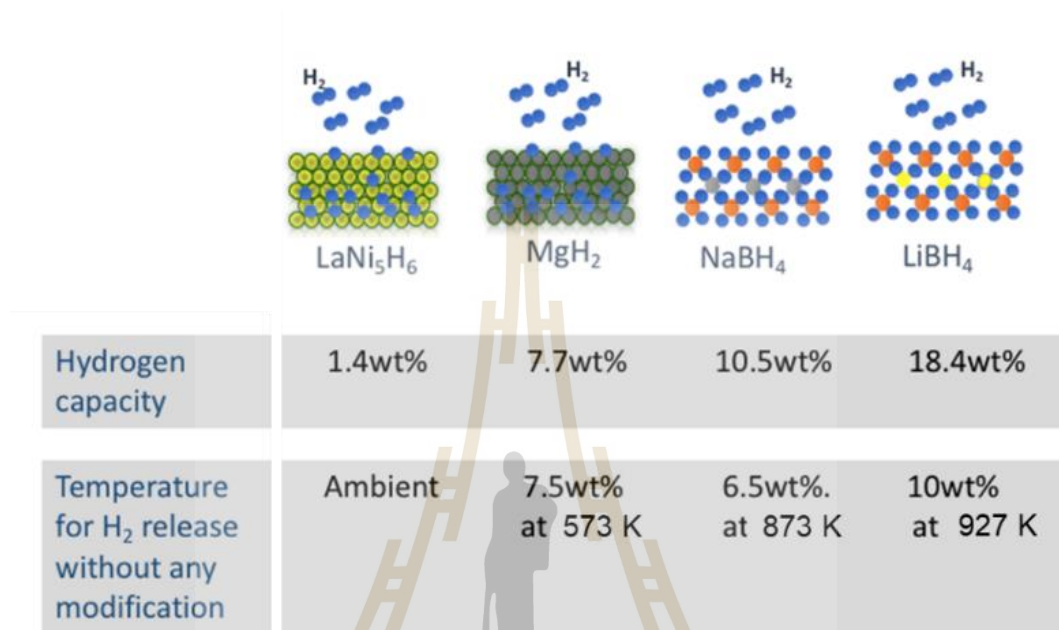


**Figure 2.8** Schematic represents the various metal hydrides materials, operating conditions, and their hydrogen capacity (<https://merlin-h2.com>).

Nevertheless, they still cannot fulfill the great obligation of hydrogen storage because of their low gravimetric capacity, irreversibility, and high operating temperatures (Reiser *et al.*, 2000; Schüth *et al.*, 2004).

Among these materials in Figure 2.8, Mg is one of the most promising candidates for hydrogen storage (Sadhasivam *et al.*, 2017) because it has a high gravimetric hydrogen density of 7.6 wt% which is higher than the US Department of Energy 2025 targets (5.5 wt%) (Allendorf *et al.*, 2018; Banerjee *et al.*, 2008; Jain *et al.*, 2010; Mahant *et al.*, 2021). In addition, Mg is accessible and low cost. Its hydride complexes exhibit good reversibility at 573 K and 0.1 MPa of  $\text{H}_2$  pressure (Jain *et al.*, 2010; Zhang *et al.*, 2018). However, these materials cannot be used onboard due to their high stability where its formation enthalpy is exothermic by 0.76 eV/mol which is much larger than

those of other metal hydrides (0.2 – 0.4 eV/mol) (Boateng and Chen, 2020; Zhang *et al.*, 2019), as shown in equation 2.2.



The formation of magnesium hydrides can be described in Figure 2.9. The adsorption process started a solid solution with the dissociation of  $\text{H}_2$  molecules to  $\text{H}_2$  atoms. Then, the  $\alpha$ -phase is happened by a relatively low hydrogen concentration when the interaction between hydrogen atoms and the surface via the van der Waals interactions, and the mobility is rapidly high. As the hydrogen concentration increase, the hydrogen atom diffuses into the subsurface where bulk migration occurs. These metals completed form a solid solution of metal hydrides or  $\beta$ -phase.

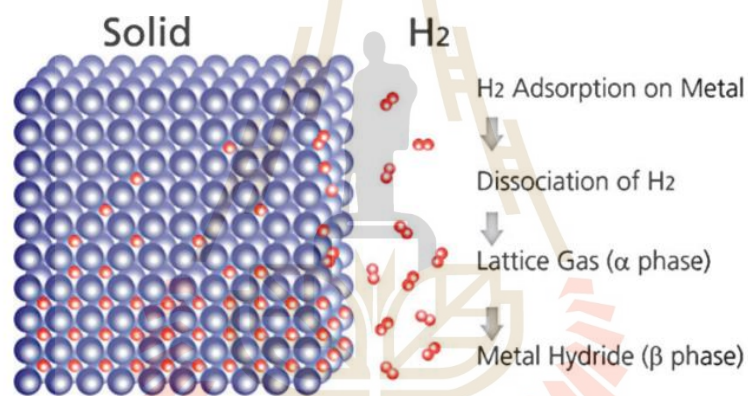


**Figure 2.9** Formation of magnesium hydride (Dimanta *et al.*, 2019).

According to the plateau pressure as a function of temperature for  $\text{MgH}_2$  (Figure 2.10), the high stability of  $\text{MgH}_2$  requires desorption temperatures higher than 550 K to desorb hydrogen under 1 bar. (Crivello *et al.*, 2016; Zhang *et al.*, 2019; Zhang *et al.*, 2018).

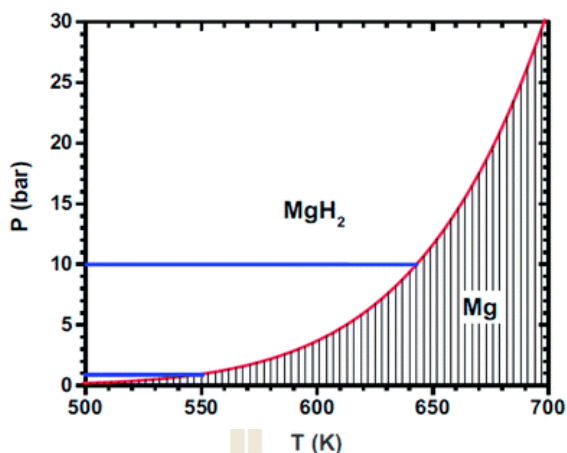


**Figure 2.10** Illustration of the temperature-dependent of dissociation pressure of  $\text{MgH}_2$  (Zhang *et al.*, 2019).

The thermodynamics of  $\text{MgH}_2$  is the main impediment to its practical application. As mentioned before, many works aimed to improve both thermodynamics and kinetics for hydrogenation and dehydrogenation of Mg-based hydrides via alloying or doping with other elements (Humphries *et al.*, 2017; Mamula *et al.*, 2014; Vujasin *et al.*, 2017).

In recent years, many efforts have been made to devoted for improving the disadvantages of high desorption temperature and slow kinetics of hydrogen sorption. To overcome these drawbacks, reducing the particle size and using additive elements as a catalyst have been reported (Emami *et al.*, 2016; Humphries *et al.*, 2017; Mamula *et al.*, 2014; Vujasin *et al.*, 2017). Both experimental and theoretical investigations have reported that the addition of transition metals (TMs) such as V (Liu *et al.*, 2011), Ni (Hong *et al.*, 2018; Zou *et al.*, 2015), Co (Kim *et al.*, 2011), Fe (Gattia *et al.*, 2019; Puzkiel *et al.*, 2018), Nb (Jin *et al.*, 2007; Takahashi *et al.*, 2013), and Ti (Bhatnagar *et al.*, 2018; Cuevas *et al.*, 2012) could play an important role in improving the hydrogen adsorption and desorption process.

#### 2.4.1 Role of catalyst on the Mg-based material in the experimental study

Based on the experimental study, Cui *et al.* investigated the effect of TMs on the Mg-based hydrogen storage performance (Cui *et al.*, 2014). They proposed that modified Mg-surface with TMs was showed the improvement of dehydrogenation properties. All samples mainly contain Mg as a core whereas the different TMs (TMs: Ti, Nb, V, Co, Mo, or Ni) are coated as a shell in the nanocomposites. Accordingly, the

automatic Sieverts apparatus was used to study the hydrogen absorption and desorption properties at 275 °C. It can be found that all samples exhibit favorable hydrogenation kinetics at a high hydrogen capacity in the range of 4.80 – 5.85 wt%, as detailed in Table 2.2. Under the same condition, the Mg-Ni sample exhibits the highest hydrogen adsorption capacity.

**Table 2.2** Experimental results of the different Mg-TM systems in the hydrogenation phase and dehydrogenation phase were characterized by XRD and XPS. The adsorption temperature and the hydrogenation capacity (wt%) were measured by automatic Sievert's apparatus at three different temperatures (°C).

Samples	Hydrogenation phase	Dehydrogenation phase	Adsorption temperature (°C)	Hydrogen capacity (wt%)
Mg-Ti	TiH <sub>2</sub>	Ti	275	5.50
Mg-Nb	Nb	Nb	275	5.85
Mg-Ni	Mg <sub>2</sub> Ni	Mg <sub>2</sub> NiH <sub>4</sub>	275	6.20
Mg-V	V	V	275	5.50
Mg-Co	Co	Co	275	5.50
Mg-Mo	Mo	Mo	275	4.80

The Temperature Programmed Desorption Mass-Spectrometry (TPD-MS) technique was used to study the dehydrogenation performance which compare with the pure Mg sample. TPD-MS results show that all systems of Mg-TM nanocomposite can dramatically decrease the desorption temperature as illustrated in Figure 2.11. Accordingly, the structures, the phases, and the surface morphology were determined by X-ray diffraction (XRD) and transmission electron microscopy (TEM). After the hydrogenation and dehydrogenation process, the Ni surface in the Mg-Ni systems exhibits different to the other Mg-TM where the formation of Mg<sub>2</sub>NiH<sub>4</sub> and Mg<sub>2</sub>Ni has

occurred. This phase can dramatically improve the adsorption and desorption processes than that of pure Mg (Cui *et al.*, 2014).

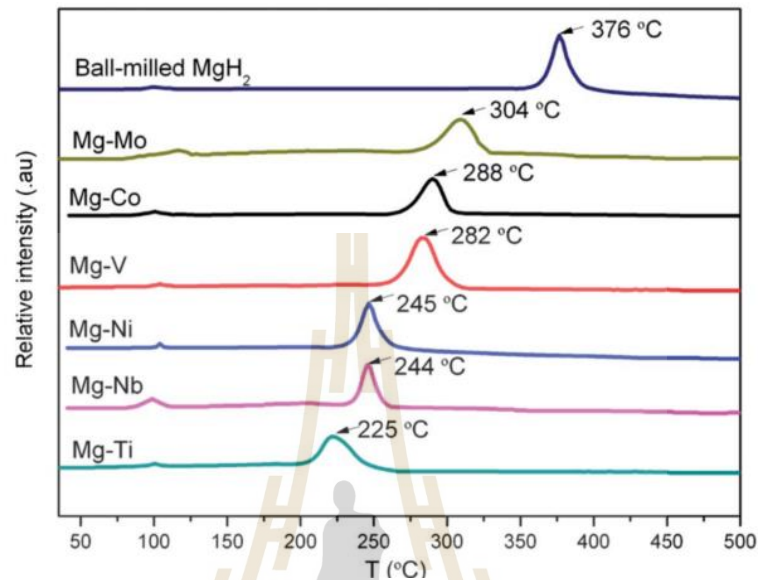


**Figure 2.11** The illustration of TPD-MS cures of the different Mg-TM systems with a heating rate of  $4 \text{ K min}^{-1}$  (Cui *et al.*, 2014).

#### 2.4.2 Role of catalyst on the Mg-based material in the computational study

To better understand insight the effect of TMs on Mg-based material, the previous computational was added TM atoms (Ti, Zr, V, Fe, Ru, Co, Rh, Ni, Pd, Cu, and Ag) as catalysts to improve the hydrogen dissociation and diffusion on Mg(0001) surface. The Mg atom was replaced by one TM atom. According to their results, the barrierless dissociation reaction was found when TMs at the left of the periodic table (TMs = Ti, V, Zr, and Ru) doped on the Mg(0001) surface. In contrast, the diffusion process shows a higher energy barrier (0.7 - 0.9 eV) than the Mg surface (0.11 eV) due to the strong interaction between the hydrogen atom and catalytic site. The results show that Ag, Cu, and Pd doped on the surface can produce a large dissociation barrier (0.39 - 1.18 eV) but the diffusion barrier is low (0.08 - 0.1 eV). Overall, these metals provide catalytic activity of dissociation and diffusion process include Ni, Rh, and Fe.

They also observed the correlation between the d-band center and dissociation and diffusion barriers. The results show that the closer the d-band center to the Fermi level, the higher the energy barriers (see Figure 2.12) (Pozzo and Alfè, 2009).

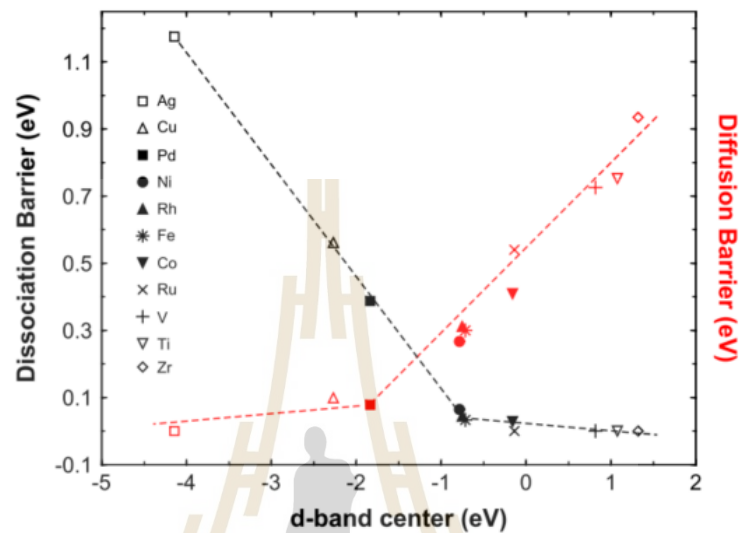


**Figure 2.12** The relation between the energy barriers of hydrogen dissociation process (black) and hydrogen diffusion barriers (red) on pure Mg and TMs doped Mg surface and the calculated d-band center position (Pozzo and Alfè, 2009)

In addition, a previous computational study also considers the heat of formations and desorption temperatures of each Mg-based hydride system. The TMs in the same period in the periodic table (Sc, Ti, V, Cr, Y, Zr, Nb, and Mo) were doped to study the effect of TMs in the Mg-bulk system. The desorption temperature was calculated as

$$T_d = \Delta H / \Delta S \quad (2.3)$$

where  $\Delta H$  and  $\Delta S$  are the heat of formation and the entropy change of the dehydrogenation reaction, respectively. The computational revealed that the heat of formation energy decreases from left to right of each period, i.e. Sc > Ti > V > Cr; Y > Zr > Nb > Cr without any significant reduction of the storage capacity. Particularly, TMs doping can decrease desorption temperature within the range of 289-393 K when compared to those of MgH<sub>2</sub> (460 K). They proposed that bonding between Mg and H

are weakening where the bond strength between Mg and TMs increases. The stability of  $\text{MgH}_2$  and its desorption temperature were reduced (El Khatabi *et al.*, 2016).

Among these additives, both experimental and theoretical studies reported that small amounts of Ni or V impurity can enhance the hydrogenation and dehydrogenation properties of Mg (Banerjee *et al.*, 2009; J. Cui *et al.*, 2014; Emami *et al.*, 2016; Xiubo *et al.*, 2018). To better understand the effect of Ni and V adding in Mg-based material, the earlier experimental studies have reported 5% of V and Ni mixed in the Mg powder where the wet mechanical alloy (MA) was used (Sakamoto and Atsumi, 2019). The hydrogen absorption capacities of the sample were examined under a hydrogen pressure of 0.2 MPa at 473 K. The experimental results show that the Mg-Ni-V alloys exhibit the highest hydrogen absorption capacity of 5.15 mass% when the sample was milled for 7 h in benzene. The particle size was decreased from 800  $\mu\text{m}$  to 20  $\mu\text{m}$  due to diffusion was facilitated. The apparent diffusion coefficient of the Mg-Ni-V is smaller than those of pure Mg, as shown in Figure 2.13.

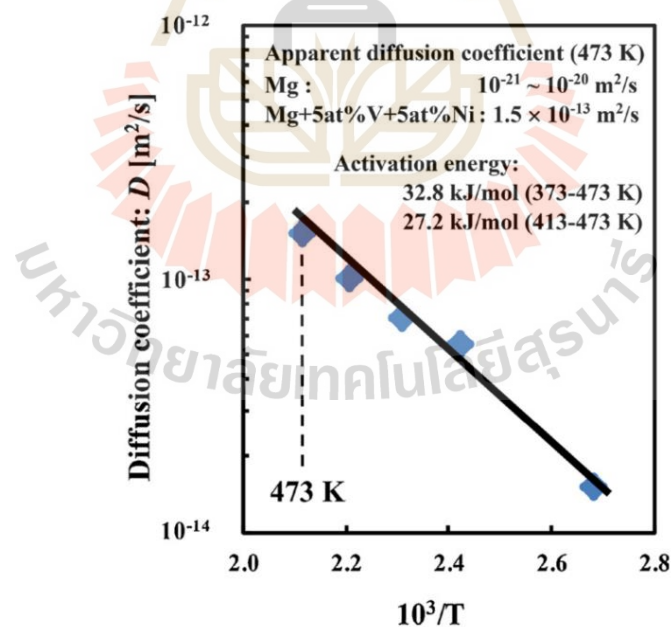


**Figure 2.13** The hydrogen diffusion coefficient for the sample milling time for 7 h. in benzene (Sakamoto and Atsumi, 2019).

For this reason, the Mg-Ni-V alloys can improve the hydrogen adsorption capacity and the diffusion distance of hydrogen better than pure Mg. The diffraction patterns from the X-ray diffractometer indicated that the Mg<sub>2</sub>Ni phase was formed during the hydrogen absorption and desorption (Sakamoto and Atsumi, 2019) as same as previous works (Cui *et al.*, 2014; Emami *et al.*, 2016).

Recently, another experimental study was proposed such a main motivation of this work. The multiphase catalysts of 5 wt% of Ni and 2.3 wt% of V on Mg nanoparticles (NPs) were prepared by the hydrogen plasma metal method (Xiubo *et al.*, 2018). The hydrogen absorption and desorption properties of the Mg-Ni-V and Mg-Ni nanocomposites were measured by the Sieverts-type apparatus. In Figure 1.7, at 473 K within 60 min, the Mg-Ni-V nanocomposite can uptake 5.1 wt% H<sub>2</sub>, compared to 4.8 wt% by Mg-Ni and 3.8 wt% by Mg-V nanocomposites H<sub>2</sub>. The experimental results show that the activation energies of the hydrogen sorption processes are reduced by 10.40 and 4.20 kJ per mol H<sub>2</sub>, respectively. Especially, the effect of Ni and V plays an important role in hydrogen adsorption and desorption performance. After the first cycling, Ni nanoparticles from an alloy with Mg substrate compound become Mg<sub>2</sub>Ni phase (J. Cui *et al.*, 2014; Emami *et al.*, 2016; Khan *et al.*, 2018). On the contrary, V nanoparticles remain in the same phase even after hydrogen absorption and desorption cycling (see in Figure 2.14). The experimental results indicate that the synergetic catalytic events occur during the sorption processes. H<sub>2</sub> molecules were dissociated into hydrogen atoms by the Mg<sub>2</sub>Ni and V nanoparticles. The dissociation of the H<sub>2</sub> molecule is mainly rate-limiting for the hydrogen absorption process on the surface and another one is the diffusion of a hydrogen atom in bulk (Xiubo *et al.*, 2018).

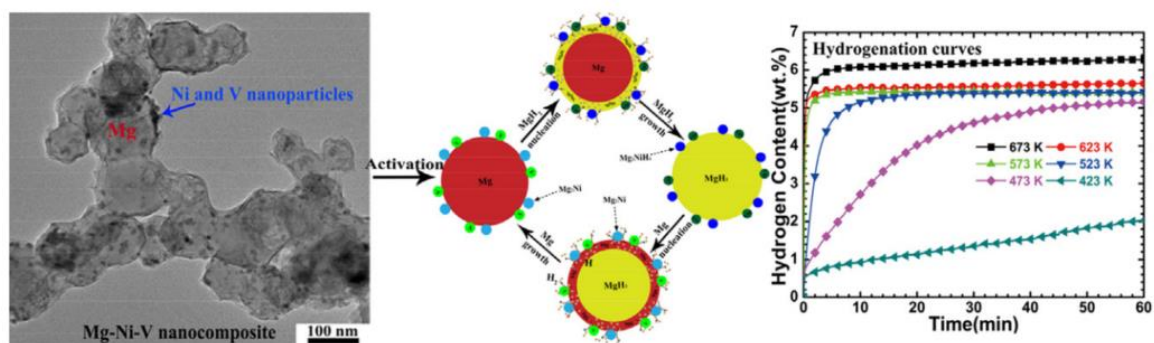


**Figure 2.14** TEM image of the Mg-Ni-V nanoparticles [left], schematic diagram proposed the catalytic effect of Mg<sub>2</sub>Ni and V [middle], and hydrogen adsorption curve of Mg-Ni-V nanocomposite (Xiubo *et al.*, 2018).

To clarify the role of Ni and V catalysts in Mg-based material, the previous computational study employed a five-layer Mg(0001) surface to study the effect of Ni and V impurities (7.52 wt% doping concentration) by substituting two Mg atoms from the same or different layers. The catalytic role of Ni and V impurities has been assessed by a computational study based on density functional theory (DFT). The hydrogen dissociation process must overcome a small energy barrier (0.14 eV) where hydrogen is placed above the catalytic site. The interaction between hydrogen atoms and the catalytic sites was increased (Banerjee *et al.*, 2009). Two hydrogen atoms show different diffusion barriers, depending upon their positions. The results reveal that the diffusion of hydrogen atoms is rate-determining step as shown in Figure 2.15. They reveal that double substitution of Ni and V atoms at the Mg sites increases interactions of metal-hydrogen bond and lowers the dissociation barrier of hydrogen molecules (Banerjee *et al.*, 2009).

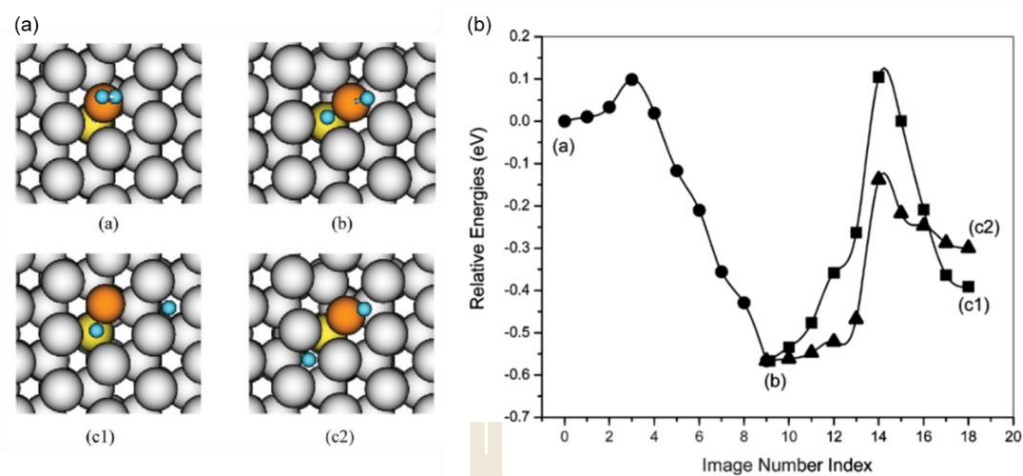


**Figure 2.15** Hydrogen dissociation and diffusion on the Ni (orange) and V (yellow) doped on Mg(0001) surface; (a) the illustration of hydrogen dissociation process, and (b) the energy profiles of hydrogen dissociation process (a) to (b), and the two diffusion paths from (b) to (c1) and (b) to (c2), and (b) (Banerjee *et al.*, 2009).

In summary, compared with hydrogen storage via physisorption in carbon-based materials and chemisorption in metal hydrides have the advantages of being completely reversible and of displaying fast kinetics. But physisorption has the disadvantage of small hydrogen sorption enthalpy due to low H<sub>2</sub> uptake. Metal hydrides have higher volumetric densities but lower gravimetric densities whereas carbon adsorbents offer better gravimetric densities but lower volumetric densities. Since hydrogen storage operating at ambient temperature is highly desirable, the new strategy to increase the operation temperature for carbon-based material is a combination of heteroatoms and TMs on the adsorbent due to increasing the binding energy between metal particles and substrate. To make lower the operating temperature for hydrides via chemisorption, the TMs acting as catalysts were added to improve the hydrogen storage materials performance. However, the understanding of the role of TMs catalysts on both solid-state materials is still limited. In this work, we employed the computational tools based on DFT calculations and ab-initio molecular dynamic (AIMD) simulations were applied to study the catalytic roles of TMs in the hydrogen storage solid-state material on hydrogen sorption process.

## 2.5 References

- Abd.Khalim Khafidz, N. Z., Yaakob, Z., Lim, K. L., and Timmiati, S. N. (2016). The kinetics of lightweight solid-state hydrogen storage materials: A review. *Int. J. Hydrog. Energy*. *41*, 13131.
- Aguey-Zinsou, K.-F. and Ares-Fernández, J.-R. (2010). Hydrogen in magnesium: new perspectives toward functional stores. *Energy Environ. Sci*. *3*, 526.
- Akbarzadeh, R., Ghaedi, M., Nasiri Kokhdan, S., and Vashaei, D. (2019). Remarkably improved electrochemical hydrogen storage by multi-walled carbon nanotubes decorated with nanoporous bimetallic Fe–Ag/TiO<sub>2</sub> nanoparticles. *Dalton Trans.* *48*, 898.
- Allendorf, M. D., Hulvey, Z., Gennett, T., Ahmed, A., Autrey, T., Camp, J., Seon Cho, E., Furukawa, H., Haranczyk, M., Head-Gordon, M., Jeong, S., Karkamkar, A., Liu, D.-J., Long, J. R., Meihaus, K. R., Nayyar, I. H., Nazarov, R., Siegel, D. J., Stavila, V., Urban, J. J., Veccham, S. P., and Wood, B. C. (2018). An Assessment of Strategies for the Development of Solid-State Adsorbents for Vehicular Hydrogen Storage. *Energy Environ. Sci*. *11*, 2784.
- Banerjee, S., Dasgupta, K., Kumar, A., Ruz, P., Vishwanadh, B., Joshi, J. B., and Sudarsan, V. (2015). Comparative evaluation of hydrogen storage behavior of Pd doped carbon nanotubes prepared by wet impregnation and polyol methods. *Int. J. Hydrog. Energy*. *40*, 3268.
- Banerjee, S., Pillai, C. G. S., and Majumder, C. (2008). First-Principles Study of the H<sub>2</sub> Interaction With Transition Metal (Ti, V, Ni) Doped Mg(0001) Surface: Implications for H-Storage Materials. *J. Chem. Phys.* *129*, 174703.
- Banerjee, S., Pillai, C. G. S., and Majumder, C. (2009). Dissociation and Diffusion of Hydrogen on the Mg(0001) Surface: Catalytic Effect of V and Ni Double Substitution. *J. Phys. Chem. C*. *113*, 10574.
- Bhatnagar, A., Johnson, J. K., Shaz, M. A., and Srivastava, O. N. (2018). TiH<sub>2</sub> as a Dynamic Additive for Improving the De/Rehydrogenation Properties of MgH<sub>2</sub>: A Combined Experimental and Theoretical Mechanistic Investigation. *J. Phys. Chem. C*. *122*, 21248.

- Boateng, E. and Chen, A. (2020). Recent Advances in Nanomaterial-Based Solid-State Hydrogen Storage. *Mater. Today Adv.* 6, 100022.
- Chen, H., Yu, H., Zhang, Q., Liu, B., Liu, P., Zhou, X., Han, Z., and Zhou, S. (2016). Enhancement in Dehydrogenation Performance of Magnesium Hydride by Iron Incorporation: A Combined Experimental and Theoretical Investigation. *J. Power Sources.* 322, 179.
- Chen, Y., Dai, J., and Song, Y. (2018). Stability and Hydrogen Adsorption Properties of Mg/Mg<sub>2</sub>Ni Interface: A First Principles Study. *Int. J. Hydrog. Energy.* 43, 16598.
- Cheng, H., Chen, L., Cooper, A. C., Sha, X., and Pez, G. P. (2008). Hydrogen spillover in the context of hydrogen storage using solid-state materials. *Energy Environ. Sci.* 1, 338.
- Crivello, J. C., Denys, R. V., Dornheim, M., Felderhoff, M., Grant, D. M., Huot, J., Jensen, T. R., de Jongh, P., Latroche, M., Walker, G. S., Webb, C. J., and Yartys, V. A. (2016). Mg-Based Compounds for Hydrogen and Energy Storage. *Appl. Phys. A.* 122, 85.
- Cuevas, F., Korablov, D., and Latroche, M. (2012). Synthesis, structural and hydrogenation properties of Mg-rich MgH<sub>2</sub>-TiH<sub>2</sub> nanocomposites prepared by reactive ball milling under hydrogen gas. *Phys. Chem. Chem. Phys.* 14, 1200.
- Cui, Liu, Wang, Ouyang, Sun, Zhu, and Yao. (2014). Mg-TM (TM: Ti, Nb, V, Co, Mo or Ni) core-shell like nanostructures: synthesis, hydrogen storage performance and catalytic mechanism. *J. Mater. Chem.* 2, 9645.
- Cui, J., Liu, J., Wang, H., Ouyang, L., Sun, D., Zhu, M., and Yao, X. (2014). Mg-TM (TM: Ti, Nb, V, Co, Mo or Ni) Core-Shell like Nanostructures: Synthesis, Hydrogen Storage Performance and Catalytic Mechanism. *J. Mater. Chem.* 2, 9645.
- Dillon, A. C., Jones, K. M., Bekkedahl, T. A., Kiang, C. H., Bethune, D. S., and Heben, M. J. (1997). Storage of hydrogen in single-walled carbon nanotubes. *Nature.* 386, 377.
- Dimanta, I., Paiders, M., Gruduls, A., and Nikolajeva, V. (2019). Selection and modification of microorganisms and substrates for acquiring and separation of energy carriers. In (pp. 69).

- Divya, P. and Ramaprabhu, S. (2014). Hydrogen storage in platinum decorated hydrogen exfoliated graphene sheets by spillover mechanism. *Phys. Chem. Chem. Phys.* *16*, 26725.
- El Khatabi, M., Bhihi, M., Lakhal, M., Abdellaoui, M., Benyoussef, A., El Kenz, A., and Loulidi, M. (2018). Enhanced Hydrogen Sorption Kinetics of Co-Doped MgH<sub>2</sub> Hydrides. *Comput. Mater.* *152*, 192.
- El Khatabi, M., Bhihi, M., Naji, S., Labrim, H., Benyoussef, A., El Kenz, A., and Loulidi, M. (2016). Study of Doping Effects with 3d and 4d-Transition Metals on the Hydrogen Storage Properties of MgH<sub>2</sub>. *Int. J. Hydrog. Energy.* *41*, 4712.
- Emami, H., Edalati, K., Staykov, A., Hongo, T., Iwaoka, H., Horita, Z., and Akiba, E. (2016). Solid-state reactions and hydrogen storage in magnesium mixed with various elements by high-pressure torsion: experiments and first-principles calculations. *RSC Adv.* *6*, 11665.
- Felderhoff, M., Weidenthaler, C., von Helmolt, R., and Eberle, U. (2007). Hydrogen storage: the remaining scientific and technological challenges. *Phys. Chem. Chem. Phys.* *9*, 2643.
- Gattia, D. M., Jangir, M., and Jain, I. P. (2019). Study on nanostructured MgH<sub>2</sub> with Fe and its oxides for hydrogen storage applications. *J. Alloys Compd.* *801*, 188.
- Georgakilas, V., Otyepka, M., Bourlinos, A. B., Chandra, V., Kim, N., Kemp, K. C., Hobza, P., Zboril, R., and Kim, K. S. (2012). Functionalization of Graphene: Covalent and Non-Covalent Approaches, Derivatives and Applications. *Chem. Rev.* *112*, 6156.
- Graetz, J. (2012). Metastable Metal Hydrides for Hydrogen Storage. *ISRN mater. sci.* *2012*, 863025.
- Hirscher, M. and Panella, B. (2005). Nanostructures with high surface area for hydrogen storage. *J. Alloys Compd.* *404-406*, 399.
- Hong, S. H., Kwak, Y. J., and Song, M. Y. (2018). Enhancement of the hydrogen-storage characteristics of Mg by adding Mg<sub>2</sub>Ni and Ni to MgH<sub>2</sub> via high energy ball milling in hydrogen atmosphere. *Korean J. Met. Mater.* *56*, 59.
- Humphries, T. D., Sheppard, D. A., and Buckley, C. E. (2017). Recent advances in the 18-electron complex transition metal hydrides of Ni, Fe, Co and Ru. *Coord. Chem. Rev.* *342*, 19.

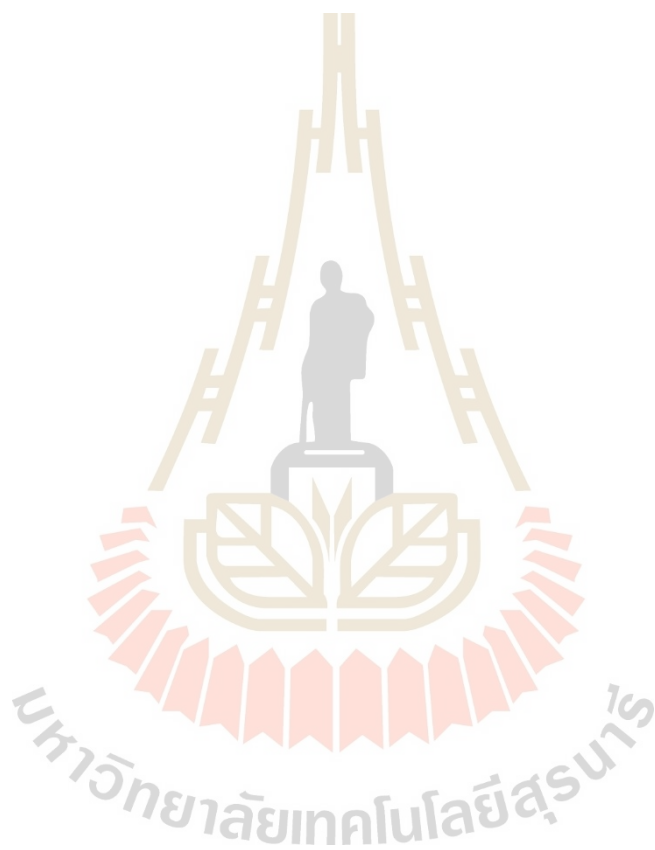
- Hwang, H. T. and Varma, A. (2014). Hydrogen storage for fuel cell vehicles. *Curr. Opin. Chem. Eng.* 5, 42.
- Jain, C. L., Ankur Jain. (2010). Hydrogen storage in Mg: A most promising material. *Int. J. Hydrog. Energy.* 35, 5133.
- Jain, I. P., Lal, C., and Jain, A. (2010). Hydrogen Storage in Mg: A Most Promising Material. *Int. J. Hydrog. Energy.* 35, 5133.
- Jin, N., Han, J., Wang, H., Zhu, X., and Ge, Q. (2015). A DFT study of oxygen reduction reaction mechanism over O-doped graphene-supported Pt<sub>4</sub>, Pt<sub>3</sub>Fe and Pt<sub>3</sub>V alloy catalysts. *Int. J. Hydrog. Energy.* 40, 5126.
- Jin, S.-A., Shim, J.-H., Ahn, J.-P., Cho, Y. W., and Yi, K.-W. (2007). Improvement in hydrogen sorption kinetics of MgH<sub>2</sub> with Nb hydride catalyst. *Acta Mater.* 55, 5073.
- Khan, D., Zou, J., Zeng, X., and Ding, W. (2018). Hydrogen storage properties of nanocrystalline Mg<sub>2</sub>Ni prepared from compressed 2MgH<sub>2</sub>Ni powder. *Int. J. Hydrog. Energy.* 43, 22391.
- Kim, H., Nakamura, J., Shao, H., Nakamura, Y., Akiba, E., Chapman, K. W., Chupas, P. J., and Proffen, T. (2011). Insight into the Hydrogenation Properties of Mechanically Alloyed Mg<sub>50</sub>Co<sub>50</sub> from the Local Structure. *J. Phys. Chem.* 115, 20335.
- Li, Q., Wang, H., Xia, H., Wei, S., and Yang, J. (2014). Density functional study of hydrogen adsorption and diffusion on Ni-loaded graphene and graphene oxide. *Int. J. Quantum Chem.* 114, 879.
- Lim, K. L., Kazemian, H., Yaakob, Z., and Daud, W. R. W. (2010). Solid-state Materials and Methods for Hydrogen Storage: A Critical Review. *Chem. Eng. Technol.* 33, 213.
- Liu, T., Zhang, T., Qin, C., Zhu, M., and Li, X. (2011). Improved hydrogen storage properties of Mg-V nanoparticles prepared by hydrogen plasma-metal reaction. *J. Power Sources.* 196, 9599.
- Liu, Y., Zhang, Z., and Wang, T. (2018). Enhanced hydrogen storage performance of three-dimensional hierarchical porous graphene with nickel nanoparticles. *Int. J. Hydrog. Energy.* 43, 11120.

- López, M. J., Cabria, I., and Alonso, J. A. (2014). Palladium Clusters Anchored on Graphene Vacancies and Their Effect on the Reversible Adsorption of Hydrogen. *J. Phys. Chem. C*. *118*, 5081.
- Ma, L., Zhang, J.-M., and Xu, K.-W. (2014). Hydrogen storage on nitrogen induced defects in palladium-decorated graphene: A first-principles study. *Appl. Surf. Sci.* *292*, 921.
- Mahant, B., Linga, P., and Kumar, R. (2021). Hydrogen Economy and Role of Hythane as a Bridging Solution: A Perspective Review. *Energy & Fuels*. *35*, 15424.
- Mamula, B., Grbović Novaković, J., Radisavljević, I., Ivanović, N., and Novaković, N. (2014). Electronic structure and charge distribution topology of MgH<sub>2</sub> doped with 3d transition metals. *Int. J. Hydrog. Energy*. *39*, 5874.
- Mohan, M., Sharma, V. K., Kumar, E. A., and Gayathri, V. (2019). Hydrogen Storage in Carbon Materials—A Review. *J. Energy Storage*. *1*, 35.
- Nagar, R., Vinayan, B. P., Samantaray, S. S., and Ramaprabhu, S. (2017). Recent advances in hydrogen storage using catalytically and chemically modified graphene nanocomposites. *J. Mater. Chem. A*. *5*, 22897.
- Nair, A. A. S., Sundara, R., and Anitha, N. (2015). Hydrogen storage performance of palladium nanoparticles decorated graphitic carbon nitride. *Int. J. Hydrog. Energy*. *40*, 3259.
- Notarianni, M., Liu, J., Vernon, K., and Motta, N. (2016). Synthesis and applications of carbon nanomaterials for energy generation and storage. *Beilstein J. Nanotechnol.* *7*, 149.
- Parambath, V. B., Nagar, R., and Ramaprabhu, S. (2012). Effect of Nitrogen Doping on Hydrogen Storage Capacity of Palladium Decorated Graphene. *Langmuir*. *28*, 7826.
- Plerdsranoy, P., Thaweelap, N., Poo-arporn, Y., Khajondetchairit, P., Suthirakun, S., Fongkaew, I., Chanlek, N., Utke, O., Pangon, A., and Utke, R. (2021). Hydrogen adsorption of O/N-rich hierarchical carbon scaffold decorated with Ni nanoparticles: Experimental and computational studies. *Int. J. Hydrog. Energy*. *46*, 5427.

- Pozzo, M. and Alfè, D. (2009). Hydrogen Dissociation and Diffusion on Transition Metal (=Ti, Zr, V, Fe, Ru, Co, Rh, Ni, Pd, Cu, Ag)-Doped Mg(0001) Surfaces. *Int. J. Hydrog. Energy*. *34*, 1922.
- Psogogiannakis, G. M. and Froudakis, G. E. (2009). DFT Study of the Hydrogen Spillover Mechanism on Pt-Doped Graphite. *J. Phys. Chem. C*. *113*, 14908.
- Puszkiel, J., Castro Riglos, M. V., Ramallo-López, J. M., Mizrahi, M., Gemming, T., Pistidda, C., Arneodo Larochette, P., Bellosta von Colbe, J., Klassen, T., Dornheim, M., and Gennari, F. (2018). New Insight on the Hydrogen Absorption Evolution of the Mg-Fe-H System under Equilibrium Conditions. *Metals*. *8*, 96701.
- Rangel, E. and Sansores, E. (2014). Theoretical study of hydrogen adsorption on nitrogen doped graphene decorated with palladium clusters. *Int. J. Hydrog. Energy*. *39*, 6558.
- Rangel, E., Sansores, E., Vallejo, E., Hernández-Hernández, A., and López-Pérez, P. A. (2016). Study of the interplay between N-graphene defects and small Pd clusters for enhanced hydrogen storage via a spill-over mechanism. *Phys. Chem. Chem. Phys.* *18*, 33158.
- Reiser, B Bogdanović, and Schlichte, K. (2000). The application of Mg-based metal-hydrides as heat energy storage systems. *Int. J. Hydrog. Energy*. *25*, 425.
- Rossetti, I., Ramis, G., Gallo, A., and Di Michele, A. (2015). Hydrogen storage over metal-doped activated carbon. *Int. J. Hydrog. Energy*. *40*, 7609.
- Sadhasivam, T., Kim, H.-T., Jung, S., Roh, S.-H., Park, J.-H., and Jung, H.-Y. (2017). Dimensional effects of nanostructured Mg/MgH<sub>2</sub> for hydrogen storage applications: A review. *Renew. Sust. Energ. Rev.* *72*, 523.
- Sakamoto, T. and Atsumi, H. (2019). Hydrogen absorption/desorption characteristics of Mg-V-Ni hydrogen storage alloys. *Fusion Eng. Des.* *138*, 6.
- Schüth, F., Bogdanović, B., and Felderhoff, M. (2004). Light Metal Hydrides and Complex Hydrides for Hydrogen Storage. *Chem. Commun.* 2249.
- Sihag, A., Xie, Z.-L., Thang, H. V., Kuo, C.-L., Tseng, F.-G., Dyer, M. S., and Chen, H.-Y. T. (2019). DFT Insights into Comparative Hydrogen Adsorption and Hydrogen Spillover Mechanisms of Pt<sub>4</sub>/Graphene and Pt<sub>4</sub>/Anatase (101) Surfaces. *J. Phys. Chem. B*. *123*, 25618.

- Sun, Y., Shen, C., Lai, Q., Liu, W., Wang, D.-W., and Aguey-Zinsou, K.-F. (2018). Tailoring magnesium based materials for hydrogen storage through synthesis: Current state of the art. *Energy Storage Mater.* 10, 168.
- Takahashi, K., Isobe, S., and Ohnuki, S. (2013). The Catalytic Effect of Nb, NbO and Nb<sub>2</sub>O<sub>5</sub> With Different Surface Planes on Dehydrogenation in MgH<sub>2</sub>: Density Functional Theory Study. *J. Alloys Compd.* 580, S25.
- Thaweelap, N., Plerdsranoy, P., Poo-arporn, Y., Khajondetchairit, P., Suthirakun, S., Fongkaew, I., Hirunsit, P., Chanlek, N., Utke, O., Pangon, A., and Utke, R. (2021). Ni-doped activated carbon nanofibers for storing hydrogen at ambient temperature: Experiments and computations. *Fuel.* 288, 119608.
- Tun, H. and Chen, C.-C. (2021). Isotheric heat of adsorption from thermodynamic Langmuir isotherm. *Adsorption.* 27, 979.
- Vujasin, R., Grbović Novaković, J., Novaković, N., Giusepponi, S., and Celino, M. (2017). Ab-Initio Study of Hydrogen Mobility in the Vicinity of MgH<sub>2</sub>-Mg Interface: The Role of Ti and TiO<sub>2</sub>. *J. Alloys Compd.* 696, 548.
- Xiubo, X., Ming, C., Peng, L., Jiayang, S., and Tong, L. (2018). Synergistic Catalytic Effects of the Ni and V Nanoparticles on the Hydrogen Storage Properties of Mg-Ni-V Nanocomposite. *Chem. Eng.* 347, 145.
- Zacharia, R. and Rather, S. u. (2015). Review of Solid State Hydrogen Storage Methods Adopting Different Kinds of Novel Materials. *J. Nanomater.* 2015, 914845.
- Zhang, J., Li, Z., Wu, Y., Guo, X., Ye, J., Yuan, B., Wang, S., and Jiang, L. (2019). Recent advances on the thermal destabilization of Mg-based hydrogen storage materials. *RSC Adv.* 9, 408.
- Zhang, J., Yan, S., and Qu, H. (2018). Recent progress in magnesium hydride modified through catalysis and nanoconfinement. *Int. J. Hydrog. Energy.* 43, 1545.
- Zhao, W., Luo, L., Chen, T., Li, Z., Zhang, Z., Wang, H., Rao, J., Feo, L., and Fan, M. (2019). Synthesis and characterization of Pt-N-doped activated biocarbon composites for hydrogen storage. *Compos. B. Eng.* . 161, 464.
- Zieliński, M., Wojcieszak, R., Monteverdi, S., Mercy, M., and Bettahar, M. M. (2007). Hydrogen storage in nickel catalysts supported on activated carbon. *Int. J. Hydrog. Energy.* 32, 1024.

Zou, J., Long, S., Chen, X., Zeng, X., and Ding, W. (2015). Preparation and hydrogen sorption properties of a Ni decorated Mg based Mg@Ni nano-composite. *Int. J. Hydrog. Energy.* 40, 1820.



## CHAPTER III

### THEORETICAL AND COMPUTATIONAL APPROACHES

#### 3.1 The Schrödinger equation

Computational chemistry has become one of the critical components of surface chemistry and catalysis science. The theoretical studies have become practical as they provide the fundamental descriptor of the chemical reactivity, materials properties, and catalytic mechanism. In the traditional methods, the behavior of electrons can be described by the basic laws of quantum mechanics, which derive from the Schrödinger equation. The general form is the time-independent Schrödinger equation that describes the quantum nature of matter is written as:

$$\hat{H}\Psi_i = E\Psi_i \quad (3.1)$$

where  $\hat{H}$  denotes the Hermitian operator describing the system's interaction, which call the Hamiltonian,  $\Psi_i$  denotes the wave function, and  $E$  is the energy. The Schrödinger equation can be solved exactly for the simplest cases.

For many bodies form of the time-independent Schrödinger equation consisting of  $M$  nuclei and  $N$  electrons are written as:

$$\hat{H}\Psi_i(\vec{r}_1, \dots, \vec{r}_N, \vec{R}_1, \dots, \vec{R}_M) = E\Psi_i(\vec{r}_1, \dots, \vec{r}_N, \vec{R}_1, \dots, \vec{R}_M) \quad (3.2)$$

where  $(\vec{r})$  denotes the position of electrons with numbers 1, 2, 3, ...,  $N$ , and nuclear coordinates  $(\vec{R})$ . In atomic units, the Hamiltonian for  $M$  nuclei and  $N$  electrons are

$$\hat{H} = -\frac{1}{2} \sum_{i=1}^N \nabla_i^2 - \frac{1}{2} \sum_{A=1}^M \nabla_A^2 - \sum_{i=1}^N \sum_{A=1}^M \frac{Z_A}{r_{iA}} + \sum_{i=1}^N \sum_{j>i}^N \frac{1}{r_{ij}} + \sum_{A=1}^M \sum_{B>A}^M \frac{Z_A Z_B}{R_{AB}} \quad (3.3)$$

where  $i$  and  $j$  denote the  $N$  electrons in the system, whereas  $A$  and  $B$  represent  $M$  nuclei, and  $Z$  are charge with nuclei.  $\nabla_i^2$  and  $\nabla_A^2$  are the Laplacian operators with respect to the coordinate of the electron ( $i$ ) and nuclei ( $A$ ). The first two terms represent the kinetic energies of electrons and nuclei. The other three terms represent the potential energy part of the Coulomb interactions consisting of nucleus-electron attraction, and the repulsion between electrons and between nuclei, respectively.

### 3.2 The Born-Oppenheimer approximation

The mass of a proton or neutron within a nucleus is over 1800 times that of an electron. The nuclei are infinitely massive where the position ( $\vec{R}$ ) will be fixed in some configurations. From eq. 3.3, appropriate approximations were used to solve the problem by reducing the complexity of the system and providing a solution where it allows to study only the electronic degrees of freedom. The Born-Oppenheimer approximation (Born and Oppenheimer, 1927) allows us to treat the electron and nuclei motion separately which consider the three remaining terms of Hamiltonian, e.g.,

$$\hat{H}_{elec} = -\frac{1}{2} \sum_{i=1}^N \nabla_i^2 - \sum_{i=1}^N \sum_{A=1}^M \frac{Z_A}{r_{iA}} + \sum_{i=1}^N \sum_{j>i}^N \frac{1}{r_{ij}} \quad (3.4)$$

However, this approach has significant limitations become  $3N$  variables for many body electron wave functions. The electrostatic repulsion between electrons is a challenging problem to solve.

### 3.3 Density functional theory

Instead of using the many-body Schrödinger equation, density functional theory (DFT) has been proposed to simplify the complexity ( $3N$  coordinates of the wave function) into the one-body density. DFT approach was proposed by Hohenberg–Kohn (Hohenberg and Kohn, 1964) and further modified by Kohn–Sham Theorems

(Kohn and Sham, 1965). Since the electron density distribution  $n(\mathbf{r})$  is used to describe the system as a function of only three spatial coordinates, which makes the solution is achievable even for a large system. The Hohenberg–Kohn proposed that the ground state electron density included the total electronic energy, kinetic energy, and potential energy. The overall electron number in each energy term in Hamiltonian becomes the interaction overall electron density. Based on Kohn–Sham theorems, they divided the functional into two terms, including the known and unknown energy functionals. The Kohn-Sham equations can be expressed as

$$\left[ -\frac{\nabla^2}{2} + \frac{1}{2} \int \frac{n(\mathbf{r}')}{|\mathbf{r} - \mathbf{r}'|} d\mathbf{r}' - \sum_{A=1}^M \int \frac{Z_A}{|\mathbf{R}_A - \mathbf{r}|} d\mathbf{r} + V_{xc}[n(\mathbf{r})] \right] \Psi_i^{KS}(\mathbf{r}) = E_i \Psi_i^{KS}(\mathbf{r}) \quad (3.5)$$

$\Psi_i^{KS}(\mathbf{r})$  is the Kohn-Sham orbital of the electron number in-band index  $i$ , and  $E_i$  is the electron energy. The first term is the kinetic energy operator of a single electron. The second term is the Coulomb repulsion. The third term is Coulomb attraction between a single electron and nuclei.  $V_{xc}[n(\mathbf{r})]$  is the exchange-correlation potential which can be expressed as a functional as

$$[V_{xc}[n(\mathbf{r})]] = \frac{\delta E_{xc} n(\mathbf{r})}{\delta n} \quad (3.6)$$

To solve the Kohn-Sham equation, The self-consistent field (SCF) method was used to solve the Kohn-Sham equation and find the ground-state density as shown in Figure 3.1.

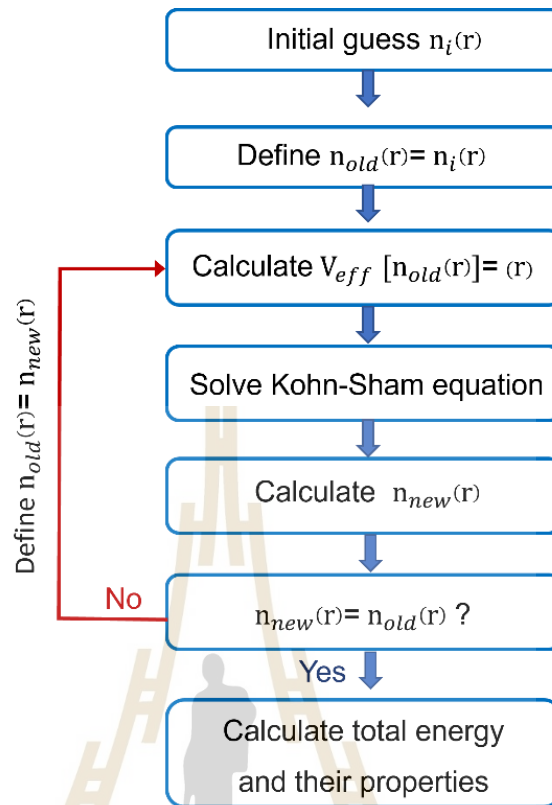


**Figure 3.1** Self-Consistent Field calculation (SCF) in DFT.

The step of self-consistent field is outlined as follows:

1. Guessing the initial trial electron density,  $n(r)$ .
2. Defining the old electron density,  $n_{old}(r) = n_i(r)$ .
3. Using the effective potential into Kohn-Sham equation and finding a single electron wavefunctions  $\psi_i$ .
4. Calculating new electron density from the calculated wavefunctions.
5. Comparing the new electron density and the old one.
  - If both densities are the same, then the obtained electron density is the ground state.
  - If both densities are different, the mixing of them will be used to calculate the next trial electron density and repeat until being self-consistent.

### 3.4 Approximations for the exchange-correlation functional

From eq. 3.6, to get more accurate results, the exact solution of the exchange-correlation functional as a functional of the density must be approximated. This term included the quantum effect of exchange and the correlation of electrons. The simplest form of all functionals is constructed the approximate exchange-correlation functional as the homogeneous electron gas system, where the so-called local density approximation (LDA). In LDA, the exchange-correlation energy is given by

$$\left[ E_{xc}^{LDA}[n(\mathbf{r})] \right] = \int n(\mathbf{r}) \epsilon_{xc} [n(\mathbf{r})] d\mathbf{r} \quad (3.7)$$

where  $\epsilon_{xc} [n(\mathbf{r})]$  is the exchange-correlation electron density of uniform electron gas. The LDA can be used to prove for a wide variety of systems where the functional depends on the electron density  $n(\mathbf{r})$  at that position. Moreover, the improved functional was achieved to use in the inhomogeneous behavior of the real system where the functional dependent on electron density and its first spatial gradient. This calls the generalized gradient approximation (GGA). In GGA, the exchange-correlation energy is written as

$$\left[ E_{xc}^{GGA}[n(\mathbf{r})] \right] = \int n(\mathbf{r}) \epsilon_{xc} [n(\mathbf{r}), \nabla n(\mathbf{r})] d\mathbf{r} \quad (3.8)$$

In practice, GGA has various commonly used forms where the terms depend on the electron density and the gradient of electron density. The difference of GGA is the mathematic term of  $\epsilon_{xc} [n(\mathbf{r}), \nabla n(\mathbf{r})]$ . In this thesis, the exchange-correlation functional was approximated using the Perdew–Burke–Ernzerhof functional (PBE) (Perdew *et al.*, 1996a) which is the most widely used in the calculation of metal (delocalize electron).

### 3.5 Plane-wave basis set and pseudopotential approximation

The density functional theory (DFT) has become one of the key components of computational material science (Lee, 2021; Weijing *et al.*, 2018). They are a powerful

tool for studying the behaviors of electrons to describe the properties of materials. The material especially metals are periodic in structure, but the calculations for properties of materials can be studies only the electrons in the periodic cell indicate the periodic properties. The Bloch's theorem can be dramatically reduced the number of atoms in the crystal as the lattice,  $\mathbf{u}_{\mathbf{k}}(\mathbf{r})$ , i.e., The equation is written as

$$\Psi_{\mathbf{k}}(\mathbf{r}) = \mathbf{u}_{\mathbf{k}}(\mathbf{r})e^{i\mathbf{k}\cdot\mathbf{r}} \quad (3.9)$$

The plane-wave is written in terms of wave vector  $\mathbf{k}$  in the reciprocal space, and the position of an atom in the unit cell represented in  $\mathbf{r}$ . The accuracy of the results depends on the number of basic sets to produce the Kohn-Sham orbital. This means that more required computational resource will be obtained with more accuracy, but it will require extensive computational resources. To overcome this problem, the number of basis sets is limited by the cut-off energy term. This concept dramatically reduces the required computational resources for solving the Kohn-Sham equations.

As mentioned previously, the physical properties of solids are mainly influenced by the valence electrons to a much greater extent than on the core electrons. This led to the concept of pseudopotential where the inner shell electrons do affect the interatomic bond significantly. The nuclease was combined with that frozen core electron. The pseudopotential of all-electrons resolves all electron potential around the ionic potential (nucleus). The pseudopotential approximation is another concept that allows the electronic wave function to expand using a much smaller number of plane wave basis states. This effective concept emphasizes that pseudopotential is a to speed-up the calculations where the number of considering electrons decrease, but also smaller the basis set used for the representative of the Kohn-Sham orbitals. There are three commonly used types of pseudopotentials: norm-conserving (Hamann *et al.*, 1979); ultrasoft (Vanderbilt, 1990); and projector augmented wave (PAW) (Blöchl, 1994; Kresse and Joubert, 1999). In this work, the projector-augmented wave (PAW) method (Blöchl, 1994; Kresse and Joubert, 1999) were used and discussed in more detail in the summary of computational information.

### 3.6 Climbing image nudged elastic band (CI-NEB) method

The nudged elastic band (NEB) was used as an efficient method for finding the transition state and minimum energy path between a given initial and final state. This method has become widely used in particular plane wave based DFT calculation and electronic structure calculation. To define the minimum energy path (MEP), the images were constructed by optimizing several intermediate images along the reaction path. A spring interaction was used to mimic an elastic band that add along the path between adjacent images due to the potential perpendicular to the band. The minimization of the force acting on the images brings the band to the MEP. The maximum energy configuration along the minimum energy path is determined as the saddle point. The NEB method has an essential feature that was proposed via the force projection. It means that the true force does not affect the distribution of images along the MEP. The CINEB method was modified from a few improvements of NEB calculation, which can promote the highest energy image to the saddle point, as shown in Figure 3.2.

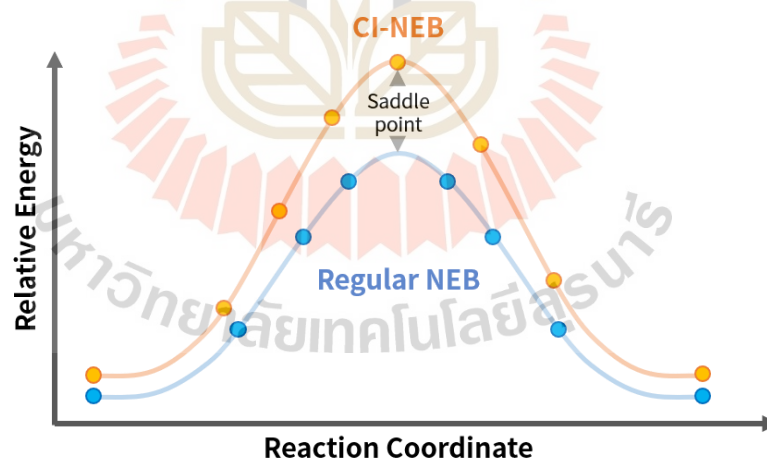


Figure 3.2 The schematic of saddle point obtained resulted from CINEB and NEB modification (<https://www.materialsquare.com>).

### 3.7 Ab-initio molecular dynamic simulation (AIMD)

In the last decade, computational simulation capabilities have continuously developed and become more powerful for comprehensive studies of chemical, physical, and material science. In the basic concept, the atoms and molecules movements occur even at low temperatures due to the quantum motion. The significant movement is thermal. This can be done using empirical potentials and describing atoms as point particles. The situation is more complicated when the system is described using quantum mechanics.

Ab initio molecular dynamics (AIMD) simulation is one of the irreplaceable techniques for realistic simulation. AIMD differs from molecular dynamic (MD) in a few things. It is well known that AIMD is based on the quantum Schrödinger equation while its classical counterpart relies on Newton's equation. An effective semiempirical potential was provided to MD to approximate quantum effects, while AIMD is based on the real physical potential. Moreover, the ab initio molecular dynamic method is based on computing the forces acting on the nuclei from electronic structure calculations. Based on quantum mechanics, the Hamiltonian contains both nuclear and electronic degrees of freedom, as detailed in equation 3.10.

$$\hat{H} = T_n + T_e + V_{ee}(\mathbf{r}) + V_{nn}(\mathbf{R}) + V_{ne}(\mathbf{r}, \mathbf{R}) \quad (3.10)$$

where  $T$ ,  $V_{ee}$ ,  $V_{nn}$ , and  $V_{ne}$  is the kinetic energy of an electron, the potential energy of electron-electron interaction, nucleus-nucleus interaction, and nucleus-electron interaction, respectively. According to the many-body effect, this equation is complicated to solve directly. To reduce the complexity, two approximations were applied to allow more extensive molecular system to be simulated and longer timescales while maintaining the predictive accuracy of the calculations.

$$[T_n + T_e + V_{ee}(\mathbf{r}) + V_{nn}(\mathbf{R}) + V_{ne}(\mathbf{r}, \mathbf{R})]\Psi(\mathbf{x}, \mathbf{R}) = E\Psi(\mathbf{x}, \mathbf{R}) \quad (3.11)$$

To this end, the nuclear and electronic contributions to the total wave function, which depends on both the nuclear and electronic coordinates, must be separated. The electronic degree of freedom ( $\mathbf{x}$ ) and nuclear degree of freedom ( $\mathbf{R}$ ) must be solved.

The adiabatic approximation was applied when the movements of the valence electrons are described with the time-dependent many-body Schrödinger equations. This approximation is justified by the electrons being much lighter than the nucleuse. The motion of electron becomes relativistic when the electrons are too close to the nucleuse, as shown in the equation:

$$\nabla_i \Psi_i = 0 \quad (3.12)$$

The second approximation assumes that the electronic and the nuclear motions are separable because of the difference between nuclear and electronic masses. As a matter of fact, the most obvious way to perform AIMD would be to compute the forces on the nuclei by performing electronic structure calculations on the ground state Born-Oppenheimer potential energy surface. The expansion reduces to a single Eigen state:

$$\Psi(\mathbf{x}, \mathbf{R}) = \phi(\mathbf{x}, \mathbf{R}) \chi(\mathbf{R}) \quad (3.13)$$

This should be a good approximation where it is assumed that the electronic wave function is in its ground state:

$$\hat{H}_e \Psi_0 = E_0 \Psi_0 \quad (3.14)$$

This equation occurs if the thermal energy is lower than the energy difference between the ground state and the first excited state in low temperature. A more straightforward approach where only the ground state wave function is included, and the wave function is assumed to be always at the minimum is Born-Oppenheimer MD (BOMD). This potential energy is minimized at every MD step. Due to the adiabatic separation, there are no additional restrictions on the maximum permissible integration time step (Mazurek *et al.*, 2021).

The Born-Oppenheimer approximations are valid to assume the nuclear motion, which is the semiclassical correspond to the nuclei are relatively heavy. Newton's equation determined this approximation due to the average nuclear motion. The Ehrenfest theorem gives the basic form for this equation. To seek and replace the interacting of electrons by a fictitious, the equivalent system of noninteracting particles further reduce the computational complexity. AIMD simulations require the CPU time-consuming and very efficient parallel computers. Kohn-Sham formulation replaces the interacting electrons with a fictitious noninteracting system that generates the same electronic density as the physical system of interacting particles (Paquet and Viktor, 2018). The electronic density is defined as

$$n \cong \sum_i f_i \langle \psi_i | \psi_i \rangle \quad (3.15)$$

where  $f_i$  is the occupation number of a given orbital. In this formulation of AIMD, the Ehrenfest term is replaced by the Kohn-Sham energy: The latter is defined as

$$E^{KS}[n] \cong -\frac{1}{2} \sum_{i=1}^N f_i \langle \psi_i | \nabla^2 | \psi_i \rangle + \int dr V_{ext}(r) n(r) + \frac{1}{2} \int dr V_H(r) n(r) + E_{XC}[n] \quad (3.16)$$

The total electronic kinetic energy associated with the electrons is the first term. The second term is the electrostatics integration energy between electron density and the external potential, and the third term is the self-electrostatic interaction energy associated with electronic density. The last term is the exchange-correlation energy or density functional, which considers the residual electronic interaction. As mentioned above, the exchange-correlation functional can be solved the electronic interchange in terms of the sole electron density. The most used AIMD codes is DFT using the generalized gradient approximation (GGA) to treat the electrons.

Also, the modern AIMD packages include most of the tools of empirical MD e.g., temperature, pressure control, and free energy calculations with different type of constraints (Laasonen, 2013).

### 3.8 Summary of computational details

All calculations were carried out based on the spin-polarized DFT method (W. Kohn and L. J. Sham, 1965) as implemented in the Vienna ab-initio simulation package (VASP 5.4) (Kresse and Furthmüller, 1996a, 1996b; Kresse and Joubert, 1999). The Perdew-Burke-Ernzerhof form of the generalized gradient approximation was employed to describe the exchange-correlation functional (Perdew *et al.*, 1996b). The projector-augmented wave method (Blöchl, 1994; Kresse and Joubert, 1999) was used to treat core-valence electron interaction and the plane-wave basis with the kinetic energy cutoff of 450 eV. The convergence criteria of self-consistent field energies were set at  $1 \times 10^{-6}$  eV while the force of the geometry optimization was set to converge within a threshold of 0.02 eV/Å.

To understand the behavior of hydrogen adsorption, the molecular and dissociative adsorption modes were examined on all surface models. The Grimme's correction method (DFT-D3) was employed to describe the van der Waals interactions in all systems (Grimme, 2006). The projected density of states (PDOS) and Bader charge analysis (Henkelman *et al.*, 2006; Sanville *et al.*, 2007) were carried out to obtain insight into the origin of the adsorption strength. In addition, we explore the hydrogen diffusion behavior on all surface models where both surface and subsurface diffusion were considered. The climbing image nudged elastic band (CI-NEB) (Henkelman *et al.*, 2000) and Dimer (Henkelman and Jónsson, 1999) methods were employed to determine the minimum energy path of hydrogen dissociation and diffusion. The CI-NEB and dimer methods allow for ionic relaxation of each configuration along the minimum path where the transition state (TS) is located at the saddle point of the reaction coordinate as confirmed by a single imaginary frequency.

Ab initio molecular dynamic (AIMD) simulations were carried out to investigate the dynamics of hydrogen dissociation, adsorption, and diffusion at high hydrogen surface coverage as an occurrence in high H<sub>2</sub> pressure. The canonical NVT ensemble of N ose thermostat was employed to set an equilibrium temperature of 300 K with a total of 40 H<sub>2</sub> molecules in the system. The simulation time was set to 30 ps with a time-step of 0.5 fs. The atomic mass of H atom was changed to the deuterium mass to facilitate the integration (Stihl and Vladimirov, 2016).

### 3.9 References

- Bl ochl, P. E. (1994). Projector Augmented-Wave Method. *Phys. Rev. B.* *50*, 17953.
- Born, M. and Oppenheimer, R. (1927). Zur Quantentheorie der Molekeln. *Ann. Phys. (Berl.)*. *389*, 457.
- Grimme, S. (2006). Semiempirical GGA-type density functional constructed with a long-range dispersion correction. *J. Comput. Chem.* *27*, 1787.
- Henkelman, G., Arnaldsson, A., and J nsson, H. (2006). A fast and robust algorithm for Bader decomposition of charge density. *Comput. Mater. Sci.* *36*, 354.
- Henkelman, G. and J nsson, H. (1999). A Dimer Method for Finding Saddle Points on High Dimensional Potential Surfaces Using Only First Derivatives. *J. Chem. Phys.* *111*, 7010.
- Henkelman, G., Uberuaga, B. P., and J nsson, H. (2000). A climbing image nudged elastic band method for finding saddle points and minimum energy paths. *J. Chem. Phys.* *113*, 9901.
- Hohenberg, P. and Kohn, W. (1964). Inhomogeneous Electron Gas. *Phys. Rev.* *136*, B864.
- Kohn and Sham. (1965). Self-Consistent Equations Including Exchange and Correlation Effects. *Phys. Rev.* *140*, A1133.
- Kohn, W. and Sham, L. J. (1965). Self-Consistent Equations Including Exchange and Correlation Effects. *Phys. Rev.* *140*, A1133.
- Kresse, G. and Furthm ller, J. (1996a). Efficiency of Ab-Initio Total Energy Calculations for Metals and Semiconductors Using a Plane-Wave Basis Set. *Comp. Mater. Sci.* *6*, 15.

- Kresse, G. and Furthmüller, J. (1996b). Efficient iterative schemes for ab initio total-energy calculations using a plane-wave basis set. *Phys. Rev. B.* 54, 11169.
- Kresse, G. and Joubert, D. (1999). From ultrasoft pseudopotentials to the projector augmented-wave method. *Phys. Rev. B.* 59, 1758.
- Laasonen, K. (2013). Ab Initio Molecular Dynamics. In L. Monticelli & E. Salonen (Eds.), *Biomolecular Simulations: Methods and Protocols* (pp. 29). Totowa, NJ: Humana Press.
- Lee, Y.-K. (2021). Density Functional Theory (DFT) Calculations and Catalysis. *Catalysts.* 11, 454.
- Mazurek, A. H., Szeleszczuk, Ł., and Pisklak, D. M. (2021). A Review on Combination of Ab Initio Molecular Dynamics and NMR Parameters Calculations. *Int. J. Mol. Sci.* 22, 4378.
- Paquet, E. and Viktor, H. L. (2018). Computational Methods for Ab Initio Molecular Dynamics. *Adv. Chem.* . 2018, 9839641.
- Perdew, J. P., Burke, K., and Ernzerhof, M. (1996a). Generalized Gradient Approximation Made Simple. *Phys. Rev. Lett.* 77, 3865.
- Perdew, J. P., Burke, K., and Ernzerhof, M. (1996b). Generalized Gradient Approximation Made Simple. *Phys. Rev. Lett.* 77, 3865.
- Sanville, E., Kenny, S. D., Smith, R., and Henkelman, G. (2007). Improved grid-based algorithm for Bader charge allocation. *J. Comput. Chem.* 28, 899.
- Stihl, C. and Vladimirov, P. V. (2016). Multiscale Modelling of Hydrogen Behaviour on Beryllium (0001) Surface. *Nucl. Mater. Energy.* 9, 547.
- Weijing, D., Weihong, Z., Xiaodong, Z., Baofeng, Z., Lei, C., Laizhi, S., Shuangxia, Y., Haibin, G., Guanyi, C., Liang, Z., and Ge, S. (2018). The application of DFT in catalysis and adsorption reaction system. *Energy Procedia.* 152, 997.

# CHAPTER IV

## DFT STUDY ON THE ROLE OF SYNERGISTIC EFFECT ON TRANSITION METALS OF Mg-BASED HYDROGEN STORAGE MATERIALS: MODEL DEVELOPMENTS

### 4.1 Introduction

As mentioned in chapter II, Mg is one of the most promising candidates for hydrogen storage due to its advantages (Sadhasivam *et al.*, 2017). It cannot be used onboard due to its high stability where its formation enthalpy is exothermic by 0.76 eV/mol which is much larger than those of other metal hydrides (0.2 – 0.4 eV/mol) (Boateng and Chen, 2020; Zhang *et al.*, 2019). Such high stability of MgH<sub>2</sub> requires high desorption temperatures of 623-673 K inhibiting its practical application for vehicles (Crivello *et al.*, 2016; Zhang *et al.*, 2019; Zhang *et al.*, 2018). As a result, many works aimed to improve the kinetics of hydrogenation and dehydrogenation of Mg-based hydrides via alloying or doping with other elements (Humphries *et al.*, 2017; Mamula *et al.*, 2014; Vujasin *et al.*, 2017).

Both experimental and theoretical investigations reported that adding transition metals (TMs) enhances the hydrogen absorption and desorption processes. Recently, it has been experimentally shown that small amounts of Ni and V impurities in Mg-based materials can reduce the activation energies from 0.77 eV to 0.58 eV for hydrogenation and from 1.25 eV to 0.88 eV for dehydrogenation, which leads to the lower operating temperature and higher hydrogen capacity of Mg-based hydrides (Emami *et al.*, 2016; Sakamoto and Atsumi, 2019; Xiubo *et al.*, 2018). After dehydrogenation, the additional Ni forms an alloy phase with Mg and yields Mg<sub>2</sub>Ni whereas the V impurity remains as nanoparticles decorated on the Mg<sub>2</sub>Ni surfaces (Xiubo *et al.*, 2018). The catalytic role of Ni and V impurities has been assessed by a computational study based on density functional theory (DFT) which reveals that double substitution of Ni and V atoms at the Mg sites increase interactions of metal-

hydrogen bond and lower the dissociation barrier of hydrogen molecules (Banerjee *et al.*, 2009).

Although many extensive experimental works were reported, most computational studies have focused solely on doping one or two atoms on the Mg host (Banerjee *et al.*, 2008, 2009; Chen *et al.*, 2012; Kecik and Aydinol, 2009; Pozzo and Alfè, 2009). Such model studies could provide information regarding interactions between hydrogen and doped transition metals which play a role in thermodynamic (adsorption energies) and kinetics (dissociation barriers) properties of the hydrogen sorption. However, the catalytic roles of the added TMs toward kinetics of other important steps of hydrogen absorption process such as hydrogen spillover, surface diffusion, and subsurface diffusion are still missing. Specifically, when the added TM catalysts co-exist as nanoclusters or alloy on the Mg host as found in the case of V and Ni co-doped Mg. Therefore, in this work, we employed the model of the V cluster supported on the Mg<sub>2</sub>Ni alloy surface to represent the experimentally observed phases of V and Ni catalysts on the Mg-based hydrogen storage materials. The DFT calculations and ab-initio molecular dynamic (AIMD) simulations were applied to study the catalytic roles of Ni and V for hydrogen adsorption, hydrogen spillover, and surface, and subsurface diffusion. These processes were studied on the Mg(0001), Mg<sub>2</sub>Ni(010) and V cluster supported on Mg<sub>2</sub>Ni surfaces. The outcome provides a theoretical insight into how V and Ni catalysts enhance the hydrogen sorption processes. In addition, to consider the effect of high hydrogen pressure at hydrogenation conditions, the effect of high hydrogen coverages on various diffusion processes was examined.

## 4.2 Computational details

The general computational setting used in this study is the same as those in chapter III, The projector-augmented wave method (Blöchl, 1994; Kresse and Joubert, 1999) was used to treat core-valence electron interaction where the valence electrons of Mg  $3s^2 2p^6$ , Ni  $4s^2 3d^8$ , V  $4s^2 3d^3$  and H  $1s^1$  were expanded in the plane-wave basis with the kinetic energy cutoff of 450 eV. To explore the effects of V and Ni catalysts on the hydrogen absorptivity, three different surface models including Mg(0001),

Mg<sub>2</sub>Ni(010), and V/Mg<sub>2</sub>Ni surfaces were used. The vacuum region of 15 Å was added in the normal direction to avoid the interaction between the periodic images.

The Monkhorst-Pack (MP) grid (Monkhorst and Pack, 1976) k-points of 4×4×1 and 3×4×1 were used for Brillouin zone sampling for Mg(0001) and Mg<sub>2</sub>Ni(010) surfaces, respectively. The optimized Mg<sub>2</sub>Ni(010) structure was applied as support to construct the V/Mg<sub>2</sub>Ni surface model.

### 4.3 Model developments

#### 4.3.1 Mg(0001) surface model

The Mg unit cell belongs to the space group P6<sub>3</sub>/mmc No.194 with  $a = b = 3.20$  Å,  $c = 5.13$  Å,  $\alpha = \beta = 90^\circ$ ,  $\gamma = 120^\circ$ . We first optimized the Mg unit cells where their calculated lattice parameters are in agreement with the experimental values for Mg ( $a = 3.18$  Å,  $c = 5.25$  Å, 1.24 % error) (Hull, 1917). Then, we created the Mg(0001) surface models using their optimized bulk structures. The Mg (0001) surface is typically observed in experiments (Sprunger and Plummer, 1991) and thus has been used as a surface model in several computational studies (Banerjee *et al.*, 2008, 2009; Chen *et al.*, 2012; Kuklin *et al.*, 2014; Pozzo and Alfè, 2009) and also in this work.

The 3×4 Mg(0001) slab model was constructed with a thickness of 4 atomic layers where the bottom 2 layers were fixed to mimic its bulk atomic positions, as shown in Figure 3.1. This model was constructed with 48 Mg atoms.

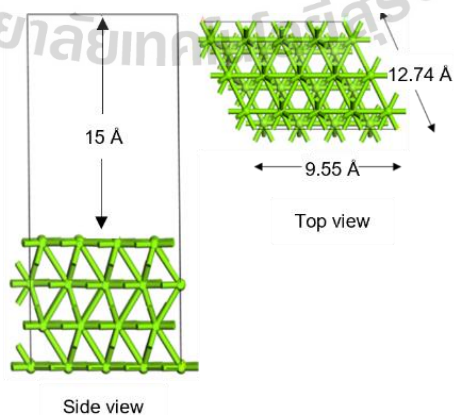


**Figure 4.1** Optimized structure of Mg(0001) surface.

### 4.3.2 Mg<sub>2</sub>Ni(010) surface model

The crystal structure of Mg<sub>2</sub>Ni is hexagonal where the space group is  $P6_222$  (No.180), as shown in Figure 4.2. There are 12 Mg and 6 Ni atoms existing the unit cell. The lattice constants of Mg<sub>2</sub>Ni are  $a = b = 5.21 \text{ \AA}$ ,  $c = 13.24 \text{ \AA}$ ,  $\alpha = \beta = 90^\circ$ ,  $\gamma = 120^\circ$  (Li *et al.*, 2016). We optimized Mg<sub>2</sub>Ni unit cells where their calculated lattice parameters were consistent with the experimental results for Mg<sub>2</sub>Ni ( $a = 5.19 \text{ \AA}$ ,  $c = 13.17 \text{ \AA}$ , 0.90 % error) (Wu *et al.*, 2017; Xu *et al.*, 2014; Zhang *et al.*, 2017).

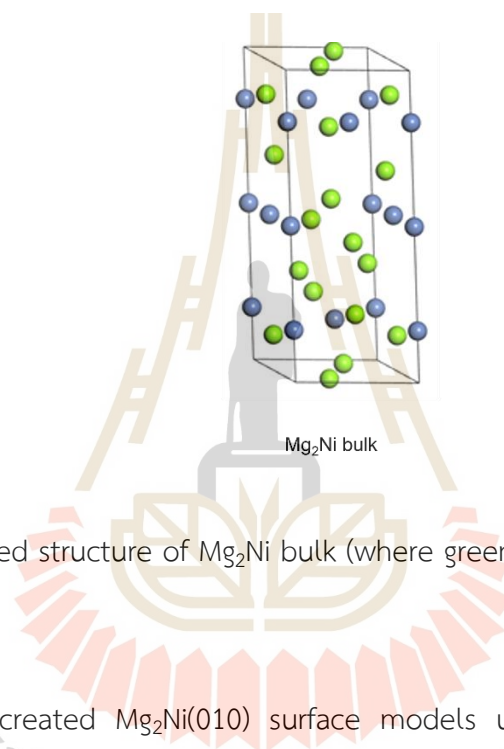


**Figure 4.2** Optimized structure of Mg<sub>2</sub>Ni bulk (where green and blue balls denote Mg and Ni atoms).

Then, we created Mg<sub>2</sub>Ni(010) surface models using their optimized bulk structures. The Mg<sub>2</sub>Ni(010) surface has been used as a surface model in several computational studies (Banerjee *et al.*, 2008, 2009; Chen *et al.*, 2012; Kuklin *et al.*, 2014; Pozzo and Alfè, 2009), which validates the methodology used in this study. The 010 surface energies were determined according to eq 4.1, where  $\gamma_{slab}$  is the surface energy of slab,  $E_{slab}$  is the total energy of the slab,  $n$  is the number of Mg and Ni include the slab, and  $E_{bulk}$  is the total energy of bulk.

$$\gamma_{slab} = \frac{E_{slab} - nE_{bulk}}{2A} \quad (4.1)$$

The 010 facet was provided the different ratios of Mg and Ni atoms on the topmost surface, as shown in Figure 3.3. The calculated results were shown in Table 4.1.

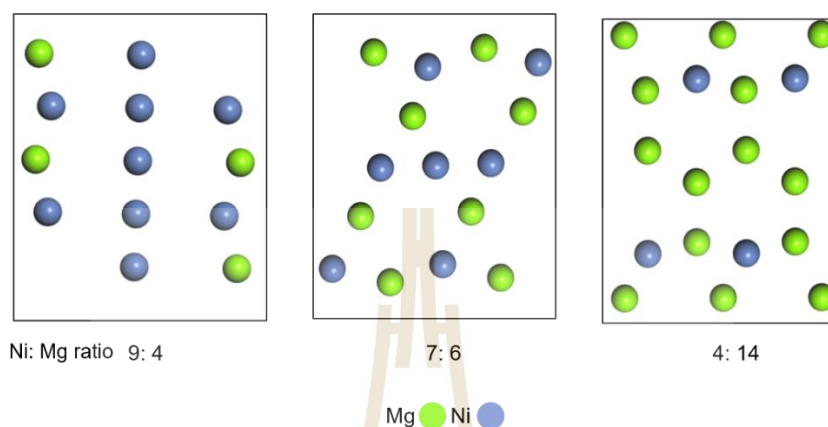


**Figure 4.3** Optimized geometries of the different ratios of Mg and Ni atoms on the topmost layers of  $Mg_2Ni(010)$  surface.

**Table 4.1** Calculated surface energy of  $Mg_2Ni(010)$  surface in the different ratios of Ni and Mg atoms on the topmost layer. Their geometrical structures are shown in Figure 4.2.

Ni: Mg ratio	Surface energy ( $eV/\text{\AA}^2$ )
9: 4	0.08
7: 6	0.07
4: 14	0.07

The different ratios of Ni and Mg atoms displayed consistency of surface energy. The Ni: Mg atoms of 7: 6 was established as suitable for use in this study because its topmost layer contains both Mg and Ni atoms where Ni acts as active sites for hydrogen adsorption as reported in several computational studies (Wu *et al.*, 2017; Xu *et al.*, 2014; Zhang *et al.*, 2017).

The final surface model of Mg<sub>2</sub>Ni(010) contains 48 Mg and 24 Ni atoms. The 1x2 slab model contains 12 atomic layers with fixed bottom 6 layers, as shown in Figure 4.4.

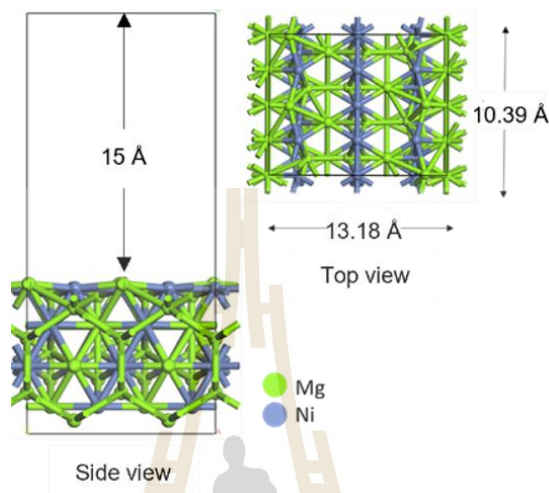


**Figure 4.4** Optimized geometries of Mg<sub>2</sub>Ni(010) surface.

### 4.3.3 V/Mg<sub>2</sub>Ni(010) surface model

The optimized Mg<sub>2</sub>Ni(010) structure was applied as support to construct the V<sub>10</sub>/Mg<sub>2</sub>Ni surface model. The stability of isolated V clusters with different shape and size were determined using the stability function (Chaves *et al.*, 2017).

#### 4.3.3.1 Optimized geometries of vanadium cluster

To obtain a reasonable vanadium cluster model, V clusters in various sizes ranging from 8-15 atoms were created and optimized. The stability function (Chaves *et al.*, 2017) was used as a descriptor to determine the energetic stability of the V cluster at a particular size. The stability function of a V cluster containing *n* atoms ( $\Delta^2 E_{(V_n)}$ ) can be calculated using the following equation,

$$\Delta^2 E_{(V_n)} = E_{tot}^{V_{n-1}} + E_{tot}^{V_{n+1}} - 2E_{tot}^{V_n} \quad (4.2)$$

where  $E_{tot}^{V_{n-1}}$ ,  $E_{tot}^{V_n}$ , and  $E_{tot}^{V_{n+1}}$  are total energies of V cluster containing *n*-1, *n*, and *n*+1 atoms, respectively.

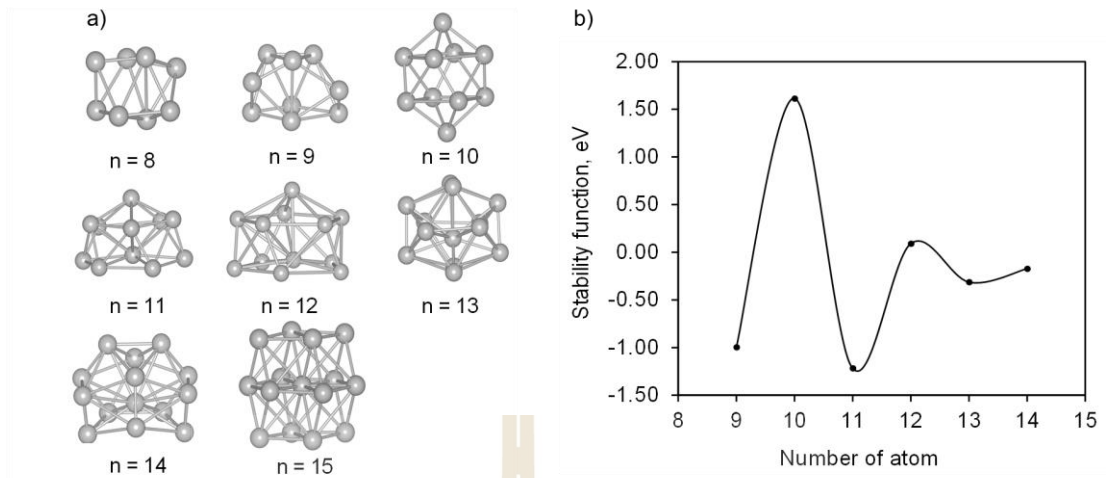


**Figure 4.5** Optimized geometries of isolated V<sub>n</sub> clusters: (a) from 8-15 atoms, and (b) Stability function,  $\Delta^2 E$ , with respect to the number of vanadium atoms ( $n = 9-14$ ).

The most stable configuration and the corresponding stability function of the V cluster containing  $n$  atoms, where  $n$  starting from 8 to 15 atoms, are shown in Figure 4.5(a). The V<sub>10</sub> cluster exhibits the highest stability function (of 1.62 eV) indicating the most stable size ( $n = 10$ ), which is in agreement with the previous computational work (Chaves *et al.*, 2017). The computations reveal that the V<sub>10</sub> cluster is most stable as it exhibits the highest stability function, as shown in Figure 4.5(b).

#### 4.3.3.2 Adsorption sites of V<sub>10</sub> on Mg<sub>2</sub>Ni(010) surface

To obtain the suitable model of V<sub>10</sub> deposited on Mg<sub>2</sub>Ni(010) surface, three distinct adsorption configurations (edge-on, face-on, and tip-on) of V<sub>10</sub> cluster on seven different sites on the Mg<sub>2</sub>Ni(010) are considered as shown in Figure 4.6. The adsorption energy of the V cluster is defined as below.

$$E_{\text{ads}} = E_{(\text{cluster/slab})} - [E_{(\text{cluster})} + E_{(\text{slab})}] \quad (4.3)$$

where the  $E_{(\text{cluster/slab})}$ ,  $E_{(\text{cluster})}$ , and  $E_{(\text{slab})}$  are total energies of the V<sub>10</sub> cluster on the slab, the isolated V<sub>10</sub> cluster, and the clean slab, respectively.

### 4.3.3.3 Adsorption sites on $Mg_2Ni(010)$ surface

The  $V_{10}$  cluster was then placed on the  $Mg_2Ni(010)$  surface where various adsorbed configurations and adsorption sites were examined. The tip-on configuration shows lower adsorption energies compared to other configurations, and these adsorption energies for all seven adsorption sites are plotted in Figure 4.6.

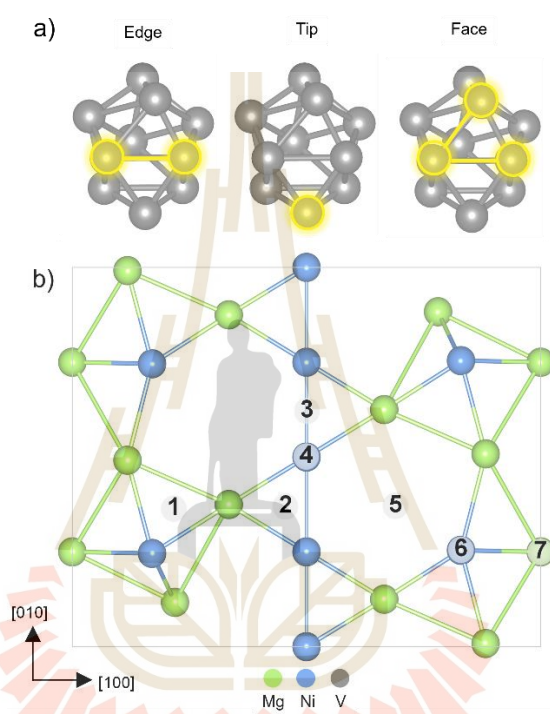


**Figure 4.6** (a) Optimized structures of 10 atoms of vanadium cluster. The yellow ball labeled the vanadium active sites. (b) seven adsorption sites of  $V_{10}$  on  $Mg_2Ni(010)$  surface.

We placed the three possible sites (i.e., E (edge), T (tip), and F (face)) of the V cluster on site 4 (atop-Ni atom) and site 7 (atop-Mg atom) on the  $Mg_2Ni(010)$  surface. All optimized structures were calculated  $E_{ads}$  by equation 4.3 corresponding to their  $E_{ads}$  shown in Figure 4.7. The  $E_{ads}$  of the V cluster was determined when more negative value means the more stable adsorbed configurations. The calculated results show that the  $V_{10}$  cluster adsorbed on the T4 in tip-on configuration is the most stable

configuration due to more interaction between the V cluster and neighboring surface atoms at the interface. Obviously, the higher distorted structure of V cluster exhibits more negative value in adsorption energy or a more stable configuration.

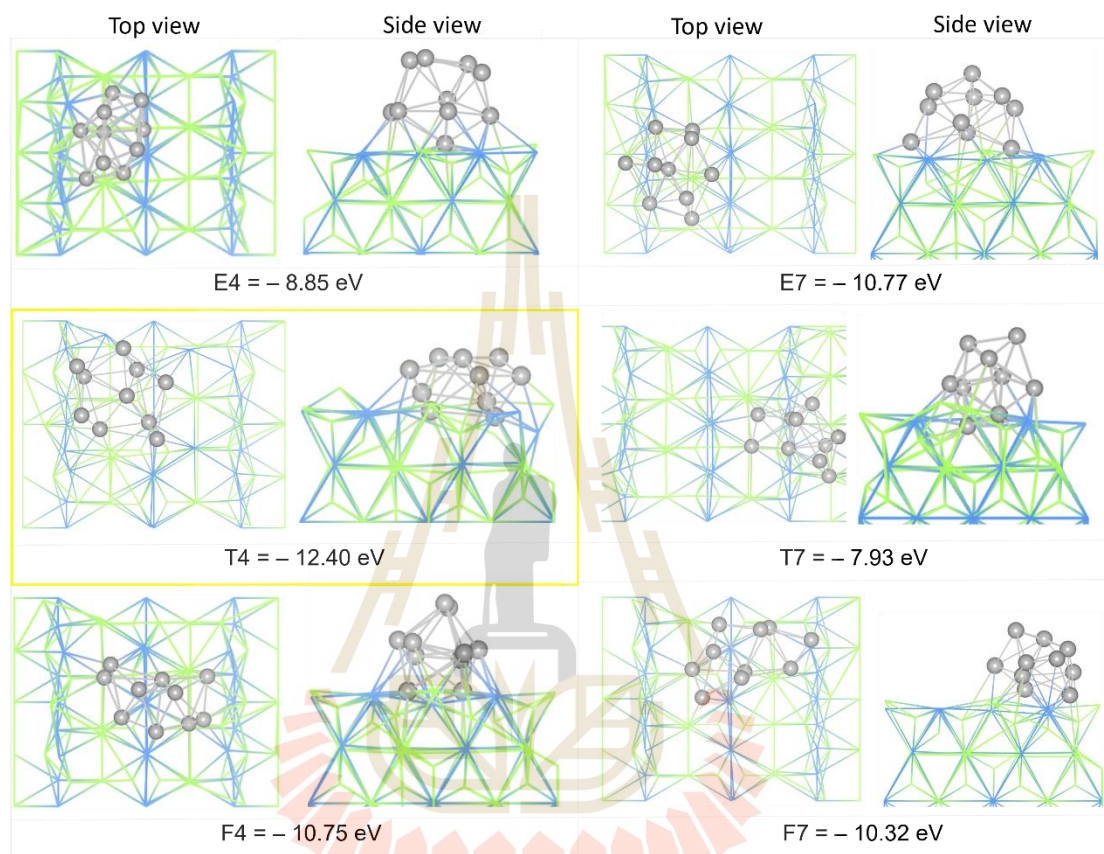


**Figure 4.7** Optimized structures of  $V_{10}$  decorated on  $Mg_2Ni(010)$  where the bottom atoms of  $V_{10}$  adsorbed on site 4 (atop-Ni atom) and site 7 (atop-Mg atom) on  $Mg_2Ni(010)$  surface at different sites: E (edge), T (tip), and F (face). The blue, green, and gray shades represent Ni, Mg, and V atoms.

In addition, we have been optimized the tip on of the V cluster to define the most stable structures at other sites (1-3, 5, and 6) on the surface, as shown in Figure 4.6. The optimized structures were shown in Figure 4.8 when compared with the most stable site of T4 as mentioned above. The results demonstrate that all configurations showed the same order of magnitude as those configurations from the previous group in the range of -12.40 - -10.49 eV. As a result, the  $V_{10}$  cluster adsorbed on T4 with tip-

on configuration is the most stable configuration, which compares to the tip-on adsorbed at different sites of the surface, as illustrated in Figure 4.8.

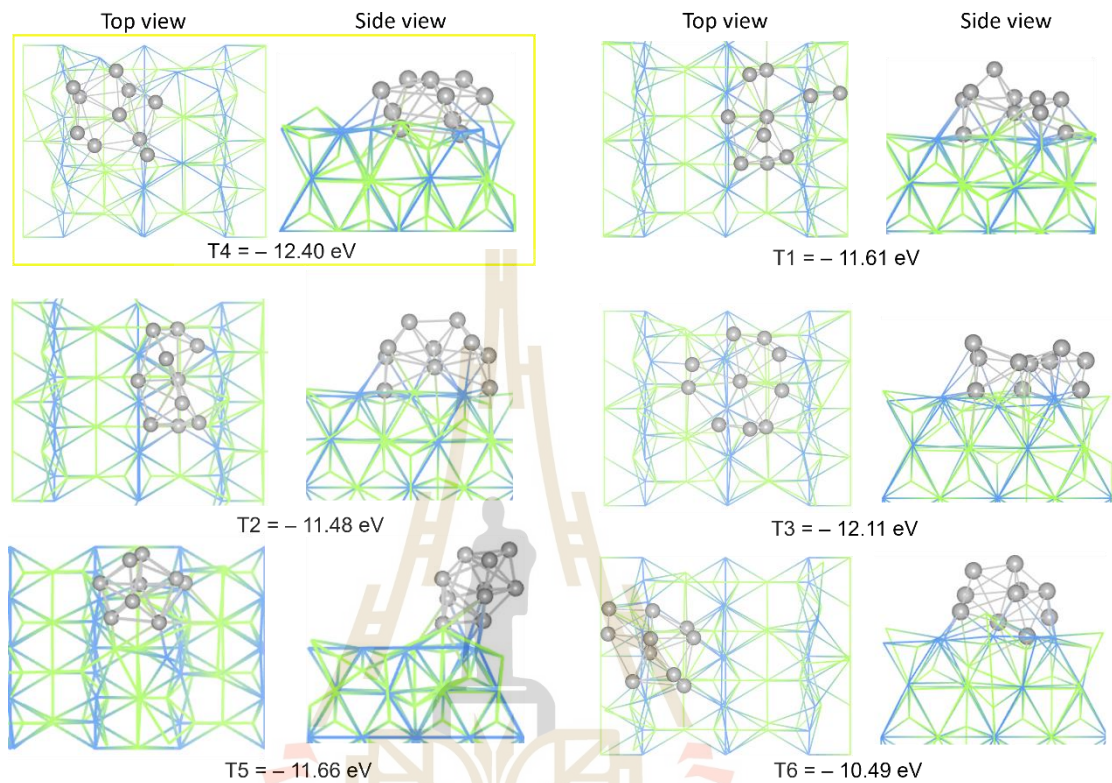


**Figure 4.8** Optimized structures of  $V_{10}$  decorated on  $Mg_2Ni(010)$  where the bottom atoms of  $V_{10}$  adsorbed on site 1-6 on  $Mg_2Ni(010)$  surface at tip-on sites. The blue, green, and gray shades represent Ni, Mg, and V atoms.

- Optimized structure of  $V_{10}$  on  $Mg_2Ni(010)$  surface

The computational results show that the V cluster prefers to adsorb on the top of the Ni site where the interaction between V atoms and Ni atoms on the surface is maximized. The V cluster and  $Mg_2Ni(010)$  surface undergo major reconstruction that some V atoms fuse into the  $Mg_2Ni(010)$  surface resulting in a very stable V/ $Mg_2Ni$  system, as shown in Figure 4.9. This allows us to define the vanadium cluster interacting with the  $Mg_2Ni$  surface (7 atoms labeled with red ball) and the vanadium cluster contacting vacuum (3 atoms labeled with orange ball).

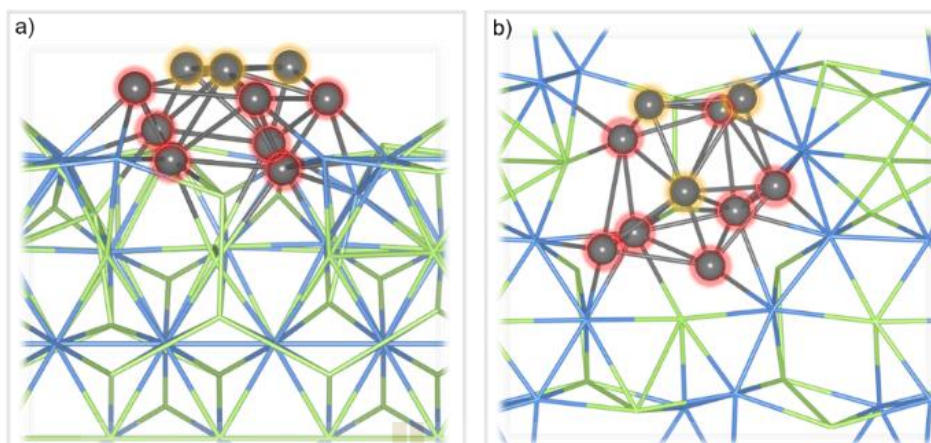


**Figure 4.9** Optimized structure of  $V_{10}$  adsorbed on  $Mg_2Ni(010)$  surface. (a) Side view, and (b) top view. The  $V_{10}$  cluster fuse into the  $Mg_2Ni(010)$  surface which can be distinguished as i) interface V atoms and ii) cluster V atoms which are marked in red and orange circles, respectively. The elements are colored as follows: green, Mg; blue, Ni; and gray, V.

#### 4.4 Conclusion

The models of  $Mg(0001)$ ,  $Mg_2Ni(010)$ , and V cluster supported on  $Mg_2Ni$  surfaces are constructed. The  $Mg_2Ni$  and V cluster deposited on  $Mg_2Ni$  structures were modeled, as evidenced by the experimental observations. The results indicate that the addition of the V cluster on the  $Mg_2Ni$  surface also induces surface reconstruction. As detailed in chapter V, we applied all surface models to study mechanisms of hydrogen adsorption and diffusion by considering all different adsorption sites.

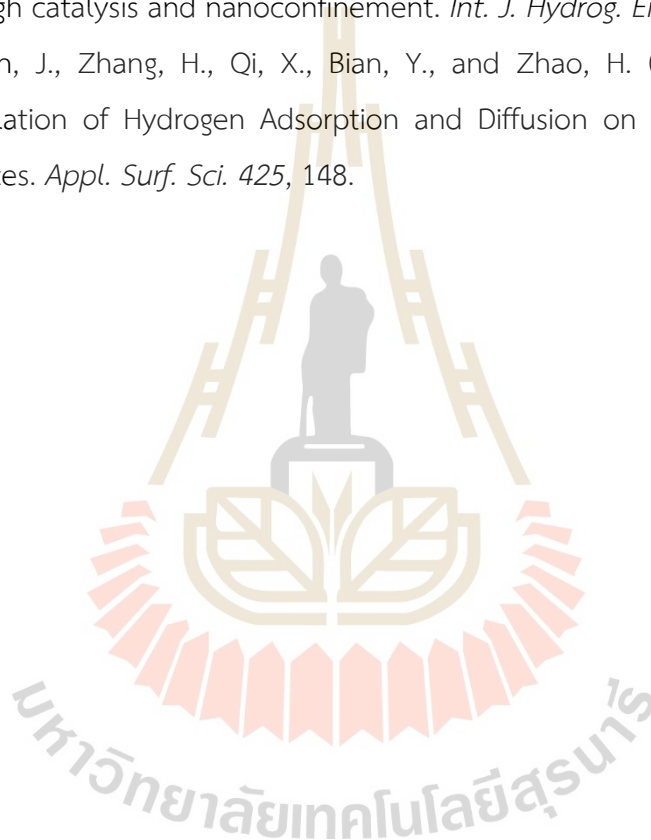
#### 4.5 References

Banerjee, S., Pillai, C. G. S., and Majumder, C. (2008). First-Principles Study of the  $H_2$  Interaction With Transition Metal (Ti, V, Ni) Doped  $Mg(0001)$  Surface: Implications for H-Storage Materials. *J. Chem. Phys.* 129, 174703.

- Banerjee, S., Pillai, C. G. S., and Majumder, C. (2009). Dissociation and Diffusion of Hydrogen on the Mg(0001) Surface: Catalytic Effect of V and Ni Double Substitution. *J. Phys. Chem. C*. *113*, 10574.
- Blöchl, P. E. (1994). Projector Augmented-Wave Method. *Phys. Rev. B*. *50*, 17953.
- Boateng, E. and Chen, A. (2020). Recent Advances in Nanomaterial-Based Solid-State Hydrogen Storage. *Mater. Today Adv.* *6*, 100022.
- Chaves, A. S., Piotrowski, M. J., and Da Silva, J. L. F. (2017). Evolution of the structural, energetic, and electronic properties of the 3d, 4d, and 5d transition-metal clusters (30 TM<sub>n</sub> systems for n = 2–15): a density functional theory investigation. *Phys. Chem. Chem. Phys.* *19*, 15484.
- Chen, M., Cai, Z.-Z., Yang, X.-B., Zhu, M., and Zhao, Y.-J. (2012). Theoretical Study of Hydrogen Dissociation and Diffusion on Nb and Ni Co-Doped Mg(0001): A Synergistic Effect. *Surf. Sci.* *606*, L45.
- Crivello, J. C., Denys, R. V., Dornheim, M., Felderhoff, M., Grant, D. M., Huot, J., Jensen, T. R., de Jongh, P., Latroche, M., Walker, G. S., Webb, C. J., and Yartys, V. A. (2016). Mg-Based Compounds for Hydrogen and Energy Storage. *Appl. Phys. A*. *122*, 85.
- Emami, H., Edalati, K., Staykov, A., Hongo, T., Iwaoka, H., Horita, Z., and Akiba, E. (2016). Solid-state reactions and hydrogen storage in magnesium mixed with various elements by high-pressure torsion: experiments and first-principles calculations. *RSC Adv.* *6*, 11665.
- Hull, A. W. (1917). The Crystal Structure of Magnesium. *PNAS*. *3*, 470.
- Humphries, T. D., Sheppard, D. A., and Buckley, C. E. (2017). Recent advances in the 18-electron complex transition metal hydrides of Ni, Fe, Co and Ru. *Coord. Chem. Rev.* *342*, 19.
- Kecik, D. and Aydinol, M. K. (2009). Density Functional and Dynamics Study of the Dissociative Adsorption of Hydrogen on Mg(0001) Surface. *Surf. Sci.* *603*, 304.
- Kresse, G. and Joubert, D. (1999). From ultrasoft pseudopotentials to the projector augmented-wave method. *Phys. Rev. B*. *59*, 1758.

- Kuklin, A. V., Kuzubov, A. A., Krasnov, P. O., Lykhin, A. O., and Tikhonova, L. V. (2014). Ni-doping effect of Mg(0001) surface to use it as a hydrogen storage material. *J. Alloys Compd.* 609, 93.
- Li, Y., Sun, G., and Mi, Y. (2016). The Structures and Properties of Y-Substituted Mg<sub>2</sub>Ni Alloys and Their Hydrides: A First-Principles Study. *AJAC. Vol.07No.01*, 8.
- Mamula, B., Grbović Novaković, J., Radisavljević, I., Ivanović, N., and Novaković, N. (2014). Electronic structure and charge distribution topology of MgH<sub>2</sub> doped with 3d transition metals. *Int. J. Hydrog. Energy.* 39, 5874.
- Monkhorst, H. J. and Pack, J. D. (1976). Special points for Brillouin-zone integrations. *Phys. Rev. B.* 13, 5188.
- Pozzo, M. and Alfè, D. (2009). Hydrogen Dissociation and Diffusion on Transition Metal (=Ti, Zr, V, Fe, Ru, Co, Rh, Ni, Pd, Cu, Ag)-Doped Mg(0001) Surfaces. *Int. J. Hydrog. Energy.* 34, 1922.
- Sadhasivam, T., Kim, H.-T., Jung, S., Roh, S.-H., Park, J.-H., and Jung, H.-Y. (2017). Dimensional effects of nanostructured Mg/MgH<sub>2</sub> for hydrogen storage applications: A review. *Renew. Sust. Energ. Rev.* 72, 523.
- Sakamoto, T. and Atsumi, H. (2019). Hydrogen absorption/desorption characteristics of Mg-V-Ni hydrogen storage alloys. *Fusion Eng. Des.* 138, 6.
- Sprunger, P. T. and Plummer, E. W. (1991). An Experimental Study of the Interaction of Hydrogen With the Mg(0001) Surface. *Chem. Phys. Lett.* 187, 559.
- Vujasin, R., Grbović Novaković, J., Novaković, N., Giusepponi, S., and Celino, M. (2017). Ab-Initio Study of Hydrogen Mobility in the Vicinity of MgH<sub>2</sub>-Mg Interface: The Role of Ti and TiO<sub>2</sub>. *J. Alloys Compd.* 696, 548.
- Wu, Z., Zhu, L., Zhang, Z., Jiang, Z., Yang, F., and Wang, Y. (2017). First Principles Study Towards the Influence of Interstitial Nitrogen on the Hydrogen Storage Properties of the Mg<sub>2</sub>Ni(010) Surface. *Int. J. Hydrog. Energy.* 42, 24868.
- Xiubo, X., Ming, C., Peng, L., Jiayang, S., and Tong, L. (2018). Synergistic Catalytic Effects of the Ni and V Nanoparticles on the Hydrogen Storage Properties of Mg-Ni-V Nanocomposite. *Chem. Eng.* 347, 145.

- Xu, B., Li, M., Li, X., Zhang, P., and Meng, L. (2014). Influence of Cr/Zr Doping on the Electronic Structure and Hydrogen Storage Properties of the  $Mg_2Ni(010)$  Surface: A First Principles Study. *J. Alloys Compd.* 601, 280.
- Zhang, J., Li, Z., Wu, Y., Guo, X., Ye, J., Yuan, B., Wang, S., and Jiang, L. (2019). Recent advances on the thermal destabilization of Mg-based hydrogen storage materials. *RSC Adv.* 9, 408.
- Zhang, J., Yan, S., and Qu, H. (2018). Recent progress in magnesium hydride modified through catalysis and nanoconfinement. *Int. J. Hydrog. Energy.* 43, 1545.
- Zhang, Z., Jin, J., Zhang, H., Qi, X., Bian, Y., and Zhao, H. (2017). First-Principles Calculation of Hydrogen Adsorption and Diffusion on Mn-doped  $Mg_2Ni(010)$  Surfaces. *Appl. Surf. Sci.* 425, 148.



# CHAPTER V

## DFT STUDY ON THE ROLE OF SYNERGISTIC EFFECT ON TRANSITION METALS OF Mg-BASED HYDROGEN STORAGE MATERIALS: RESULTS AND DISCUSSION

### 5.1 Introduction

To understand the behavior of hydrogen adsorption, the molecular and dissociative adsorption modes were examined on all surface models. Grimme's correction method (DFT-D3) was employed to describe the van der Waals interactions in all systems (Grimme, 2006). The projected density of states (PDOS) and Bader charge analysis (Henkelman *et al.*, 2006; Sanville *et al.*, 2007) were carried out to obtain insight into the origin of the adsorption strength. In addition, we explore the hydrogen diffusion behavior on all surface models where both surface and subsurface diffusion were considered. The climbing image nudged elastic band (CI-NEB) (Henkelman *et al.*, 2000) and Dimer (Henkelman and Jónsson, 1999) methods were employed to determine the minimum energy path of hydrogen dissociation and diffusion. The CI-NEB and dimer methods allow for ionic relaxation of each configuration along the minimum path where the transition state (TS) is located at the saddle point of the reaction coordinate as confirmed by a single imaginary frequency.

Ab initio molecular dynamic (AIMD) simulations were carried out to investigate the dynamics of hydrogen dissociation, adsorption, and diffusion at high hydrogen surface coverage as an occurrence in high H<sub>2</sub> pressure. The canonical NVT ensemble of the Nóse thermostat was employed to set an equilibrium temperature of 300 K with 40 H<sub>2</sub> molecules in the system. The simulation time was set to 30 ps with a time-step of 0.5 fs. The atomic mass of the H atom was changed to the deuterium mass to facilitate the integration (Stihl and Vladimirov, 2016). The AIMD results were also used to guide possible diffusion paths at low and high coverages.

## 5.2 Behavior of H<sub>2</sub> adsorption

To understand the behavior of hydrogen adsorption, the molecular and dissociative adsorption modes were examined. We calculated and compared H<sub>2</sub> adsorption energies on three different surface models, i.e., Mg(0001), Mg<sub>2</sub>Ni(010), and V/Mg<sub>2</sub>Ni surfaces. All adsorption modes were considered. The adsorption energies,  $E_{\text{ads}}$ , can be calculated using the following equation:

$$E_{\text{ads}} = E_{\text{H}_2/\text{surface}} - (E_{\text{surface}} + E_{\text{H}_2}) \quad (5.1)$$

where  $E_{\text{H}_2/\text{surface}}$  is the total energy of a structure with adsorbed hydrogen,  $E_{\text{surface}}$  is the total energy of the clean Mg(0001), Mg<sub>2</sub>Ni(010), or V/Mg<sub>2</sub>Ni surface structures, and  $E_{\text{H}_2}$  is the total energy of a H<sub>2</sub> molecule. The more negative  $E_{\text{ads}}$  indicates the stronger hydrogen adsorption. The projected density of states (PDOS) and Bader charge analysis (Henkelman *et al.*, 2006; Sanville *et al.*, 2007) were carried out to obtain insight into the origin of the adsorption strength. In addition, the climbing image nudged elastic band (CI-NEB) (Henkelman *et al.*, 2000) methods were employed to determine the minimum energy path of hydrogen dissociation. All the data were summarized in Table 5.1 and Figure 5.1. The H<sub>2</sub> molecule is placed on the surfaces in a parallel orientation. The H<sub>2</sub> molecule molecularly adsorbs on the top site of Mg(0001) surfaces. The two hydrogen atoms occupy the hollow sites after the dissociation process above the hollow site of the Mg(0001) surface, as shown in Figure 5.1. The H<sub>2</sub> molecule weakly interacts with the Mg(0001) surface with an  $E_{\text{ads}}$  of -0.05 eV. The H<sub>2</sub> molecule locates at 3.50 Å above the surface and maintains the same H-H bond length of 0.75 Å with an isolated gas H<sub>2</sub> molecule, as shown in Figure 5.1(a). The dissociative adsorption is 0.07 eV more favorable than molecular adsorption on Mg(0001) surface; however, the H-H bond breaking requires a relatively high energy barrier of 0.64 eV. The dissociated H atoms prefer to bind at the 3-fold hollow site, as shown in Figure 5.1(b).

**Table 5.1** Calculated adsorption energies,  $E_{\text{ads}}$ , (eV) for hydrogen adsorption on the Mg(0001), Mg<sub>2</sub>Ni(010), and V<sub>10</sub>/Mg<sub>2</sub>Ni(010) surfaces. The energy barrier of hydrogen dissociation (eV). Bader Charges of the total hydrogen atoms in (Q, H) |e|. The adsorption site is the nearest neighbor of hydrogen atoms.

NO	Surface	$E_{\text{ads}}$ (eV)	Adsorption mode	H-H bond (Å)	$E_a$ (eV)	Q, H ( e )	Adsorption site
1	Mg(0001)	-0.04	Molecular	0.75	-	0.02	Mg <sub>top</sub>
2	Mg(0001)	-0.05	Molecular	0.75	-	0.02	Mg <sub>hollow</sub>
3	Mg(0001)	-0.05	Molecular	0.75	-	0.02	Mg <sub>bridge</sub>
4	Mg(0001)	-0.12	Dissociative	-	0.64	1.95	Mg <sub>hollow</sub>
5	Mg <sub>2</sub> Ni(010)	-0.59	Kubas	0.90	-	0.10	Ni <sub>top</sub>
6	Mg <sub>2</sub> Ni(010)	-0.59	Kubas	0.90	-	0.10	Ni <sub>top</sub>
7	Mg <sub>2</sub> Ni(010)	-0.88	Kubas	0.94	barrierless	0.83	Ni <sub>top</sub>
8	Mg <sub>2</sub> Ni(010)	-0.88	Kubas	0.94	barrierless	0.83	Ni <sub>top</sub>
9	Mg <sub>2</sub> Ni(010)	-0.06	Molecular	0.75	-	0.03	Mg <sub>top</sub>
10	Mg <sub>2</sub> Ni(010)	-0.13	Molecular	0.77	-	0.05	Ni <sub>bridge</sub>
11	Mg <sub>2</sub> Ni(010)	-0.11	Molecular	0.76	-	0.05	Ni <sub>bridge</sub>
12	Mg <sub>2</sub> Ni(010)	-0.09	Molecular	0.76	-	0.03	Mg-Ni <sub>hollow</sub>
13	Mg <sub>2</sub> Ni(010)	-1.57	Dissociative	-	barrierless	0.93	Mg-Ni <sub>hollow</sub>
14	Mg <sub>2</sub> Ni(010)	-1.80	Dissociative	-	barrierless	0.83	Mg-Ni <sub>hollow</sub>
15	Mg <sub>2</sub> Ni(010)	-1.57	Dissociative	-	barrierless	0.93	Mg-Ni <sub>hollow</sub>
16	Mg <sub>2</sub> Ni(010)	-1.57	Dissociative	-	barrierless	0.93	Mg-Ni <sub>hollow</sub>
17	Mg <sub>2</sub> Ni(010)	-1.47	Dissociative	-	barrierless	1.04	Mg-Ni <sub>hollow</sub>
18	Mg <sub>2</sub> Ni(010)	-1.80	Dissociative	-	barrierless	0.83	Mg-Ni <sub>hollow</sub>

**Table 5.1** (Continued) Calculated adsorption energies,  $E_{\text{ads}}$ , (eV) for hydrogen adsorption on the Mg(0001), Mg<sub>2</sub>Ni(010), and V<sub>10</sub>/Mg<sub>2</sub>Ni(010) surfaces. Bader Charges of the total hydrogen atoms in (Q, H) |e|. The adsorption site is the nearest neighbor of hydrogen atoms.

NO	Surface	$E_{\text{ads}}$ (eV)	Adsorption mode	H-H bond d (Å)	$E_a$ (eV)	Q, H ( e )	Adsorption site
19	V/ Mg <sub>2</sub> Ni(010)	-2.10	Dissociative	-	barrierless	1.00	V <sub>hollow</sub>
20	V/ Mg <sub>2</sub> Ni(010)	-1.91	Dissociative	-	barrierless	1.00	V <sub>hollow</sub>
21	V/ Mg <sub>2</sub> Ni(010)	-1.11	Dissociative	-	barrierless	0.87	Interface
22	V/ Mg <sub>2</sub> Ni(010)	-2.03	Dissociative	-	barrierless	1.00	V <sub>hollow</sub>
23	V/ Mg <sub>2</sub> Ni(010)	-1.60	Dissociative	-	barrierless	0.82	Interface
24	V/ Mg <sub>2</sub> Ni(010)	-1.97	Dissociative	-	barrierless	1.00	V <sub>hollow</sub>
25	V/ Mg <sub>2</sub> Ni(010)	-0.87	Dissociative	-	barrierless	1.53	Interface
26	V/ Mg <sub>2</sub> Ni(010)	-1.31	Dissociative	-	barrierless	0.82	Interface
27	V/ Mg <sub>2</sub> Ni(010)	-1.43	Dissociative	-	barrierless	0.69	Interface
28	V/ Mg <sub>2</sub> Ni(010)	-0.90	Dissociative	-	barrierless	0.78	Interface
29	V/ Mg <sub>2</sub> Ni(010)	-1.39	Dissociative	-	barrierless	0.84	Interface
30	V/ Mg <sub>2</sub> Ni(010)	-1.37	Dissociative	-	barrierless	0.84	Mg-Ni <sub>hollow</sub>
31	V/ Mg <sub>2</sub> Ni(010)	-0.64	Kubas	0.95	-	0.20	Ni <sub>top</sub>
32	V/ Mg <sub>2</sub> Ni(010)	-0.08	Molecular	0.75	-	0.04	Mg <sub>stop</sub>

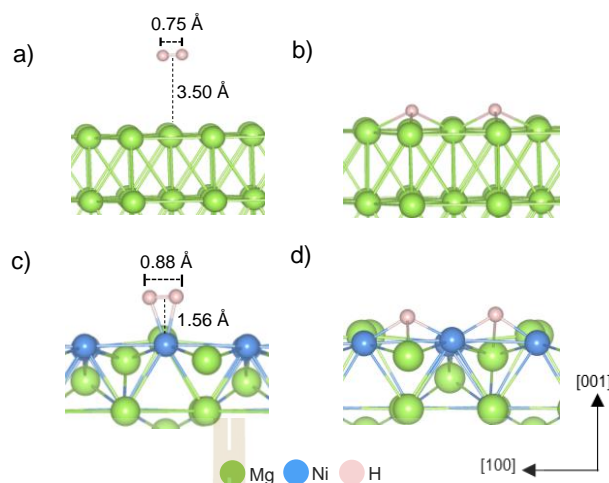


**Figure 5.1** Atomic structures of  $H_2$  on (a) molecular adsorption mode on Mg atop site, (b) dissociative adsorption on two Mg hollow sites, (c) Kubas adsorption on Ni atop site, and (d) dissociative adsorption on two Ni-Ni-Mg hollow sites. The labeling numbers show associated H-H, H-Mg, or H-Ni bond lengths in Angstrom.

The calculated results are in good agreement with those reported in previous works for adsorption geometry, adsorption energies ( $-0.06$  -  $-0.03$  eV), and the dissociation energy barriers ( $0.88$  -  $1.05$  eV) on clean Mg(0001) surface (Banerjee *et al.*, 2008; Chen *et al.*, 2012; Pozzo *et al.*, 2008). The significantly weak adsorption and high  $H_2$  dissociation barrier imply that pristine Mg is not suitable hydrogen storage material.

Improved adsorptivity is expected from the addition of Ni catalysts. Under operating conditions of hydrogen storage, the incorporation of Ni in Mg host material yields a  $Mg_2Ni$  phase as evidenced in experimental works (Cui *et al.*, 2014; Xiubo *et al.*, 2018; Zou *et al.*, 2015). Therefore, the  $Mg_2Ni(010)$  surface was applied. Three different adsorption sites were considered: Ni atop site, Mg atop site, and Mg-Ni hollow site, as detailed in Table 5.1.

The molecular  $H_2$  is likely to adsorb on atop site of Ni atom rather than Mg atom on  $Mg_2Ni(010)$  surface. The presence of Ni significantly improves  $H_2$  adsorptivity: molecular  $H_2$  exhibits stronger interaction with the Ni atom ( $E_{ads} = -0.88$  eV) than with

the Mg atom ( $E_{\text{ads}} = -0.06$  eV), as shown in Figure 5.1(c). The molecular adsorption on  $\text{Mg}_2\text{Ni}(010)$  adopted a so-called Kubas mode of adsorption (Kubas, 1988; Ma *et al.*, 2014). The Kubas adsorption mode occurs with an elongation of the H-H bond by 0.15 Å (compared to gas-phase  $\text{H}_2$ ) and a decrease in the molecular-surface distance, indicating a stronger interaction between  $\text{H}_2$  molecule and active site as compared to the  $\text{Mg}(0001)$  surface. The Kubas adsorption mode facilitates hydrogen dissociation on the  $\text{Mg}_2\text{Ni}$  surface resulting in barrierless for  $\text{H}_2$  dissociation. Upon  $\text{H}_2$  dissociation, the dissociative adsorption on the  $\text{Mg}_2\text{Ni}$  surface is significantly stable with an  $E_{\text{ads}}$  of  $-1.57$  eV. Both hydrogen atoms are located on two Ni-Ni-Mg hollow sites, as shown in Figure 5.1(d). The calculated results also agree with the previous computational works using the DFT-PBE method that the  $\text{H}_2$  dissociation on the Ni-doped  $\text{Mg}(0001)$  surface is barrierless with  $E_{\text{ads}}$  in the range of  $-0.60$  to  $-1.34$  eV (Banerjee *et al.*, 2008; Chen *et al.*, 2012; Pozzo *et al.*, 2008). Besides atop site of Ni, the molecular adsorption on the Mg atop site, bridge site, or the hollow site in  $\text{Mg}_2\text{Ni}$  surface is still a weak interaction like that in Mg surface.

We now turn to describe the synergistic effect of the V and Ni catalysts using the  $\text{V}_{10}/\text{Mg}_2\text{Ni}$  surface model, where various adsorption modes and sites were studied. Many adsorption sites on the V cluster, the  $\text{Mg}_2\text{Ni}$  surface, and the cluster-surface interface were considered. As illustrated in Figure 5.2, the calculated  $E_{\text{ads}}$  at various adsorption sites indicates that the most energetically favorable sites are at the V cluster where dissociative adsorption is the preferred adsorption mode with an  $E_{\text{ads}}$  in the range of  $-2.10$  to  $-1.91$  eV. Dissociative adsorption at cluster-surface interface sites and on  $\text{Mg}_2\text{Ni}$  surface sites is less stable than on the V cluster, yet still relatively highly favorable. The adsorption energies range from  $-1.60$  to  $-0.87$  eV at the interface sites and  $-1.37$  to  $-0.08$  eV at the  $\text{Mg}_2\text{Ni}$  surface sites. Like the  $\text{Mg}_2\text{Ni}$  surface, the  $\text{H}_2$  dissociation on  $\text{V}/\text{Mg}_2\text{Ni}$  surface are barrierless, indicating that the dissociative adsorption is spontaneous on both  $\text{Mg}_2\text{Ni}$  and  $\text{V}/\text{Mg}_2\text{Ni}$  surfaces. In contrast, the molecular adsorption, found only on the Mg sites on the surface, exhibits much weaker  $E_{\text{ads}}$  of  $-0.08$  eV.

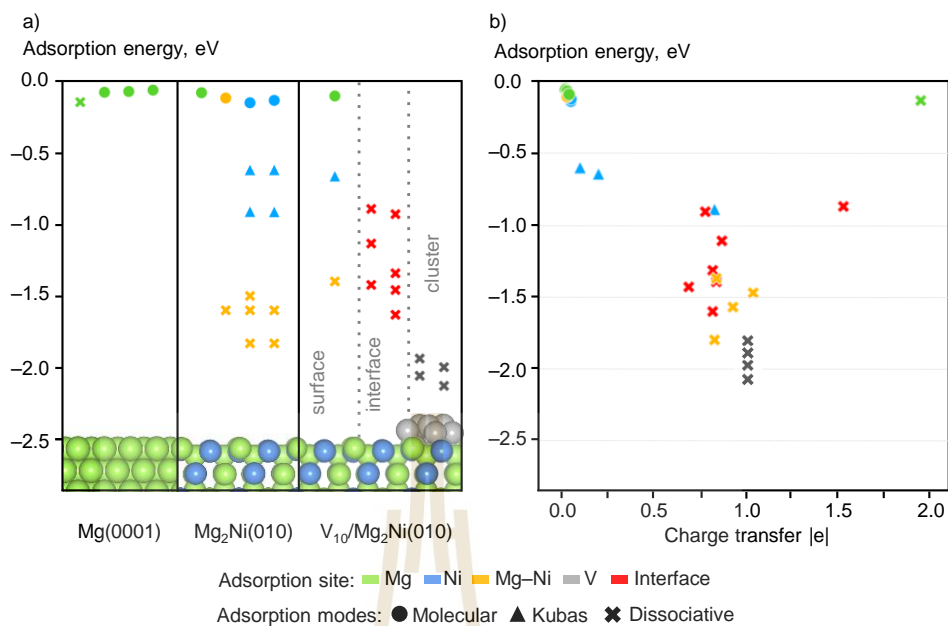


**Figure 5.2** The relationship between the adsorption energies of hydrogen and (a) adsorption sites and (b) degrees of charge transfer from the surface to the adsorbed H atoms. All illustrations of the atomic structures are generated by VESTA (Momma and Izumi, 2011).

To better understand the adsorption behavior, charge transfer to adsorbed hydrogen was calculated using Bader charge analysis (Henkelman *et al.*, 2006; Sanville *et al.*, 2007). Upon H<sub>2</sub> adsorption, the electrons of the surfaces are transferred to hydrogen atoms, as depicted in Figure 5.3.

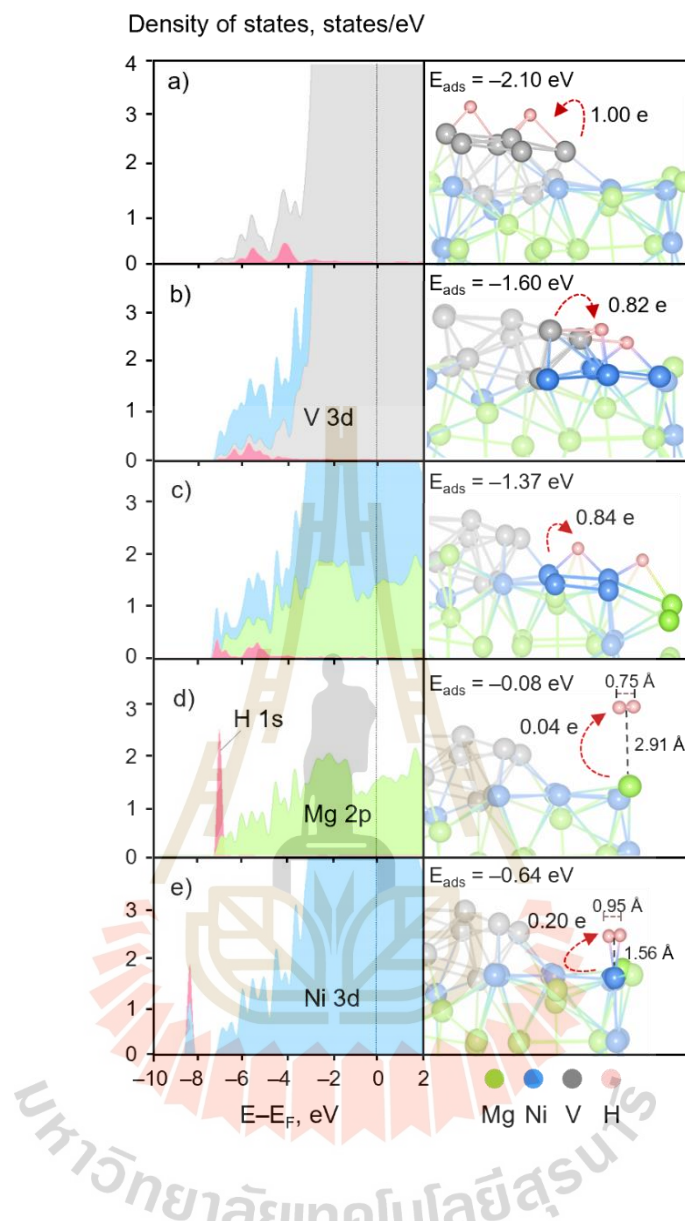


**Figure 5.3** Calculated projected density of states (PDOS) [left] and charge transfer to hydrogen [right] upon adsorption on  $V_{10}/Mg_2Ni(010)$  surface at (a) V cluster, (b) interface, (c) hollow site on the surface, (d) atop of Mg, and (e) atop of Ni. The shaded areas in the PDOS represent the states contributed by H 1s (pink), V 3d (gray), Ni 3d (blue), and Mg 2p (green). The vertical dash line in the PDOS denotes the Fermi level ( $E_F$ ). The labeled numbers next to red arrows indicate numbers of charge transfer from substrate to adsorbed hydrogen atoms or molecules.

The adsorption energies correlate with the number of transferred electrons, i.e., stronger adsorption generally involves greater charge transfer to the adsorbed hydrogen atoms. In particular, the strong dissociative adsorption that occurred at the TM sites consistently exhibits high charge transfer. For example, adsorptions on the V cluster ( $E_{\text{ads}} = -2.10$  eV), interface ( $E_{\text{ads}} = -1.60$  eV), and  $\text{Mg}_2\text{Ni}$  surface ( $E_{\text{ads}} = -1.37$  eV), exhibit a relatively high charge transfer of 1.00, 0.82, and 0.84  $|e|$ , respectively (Figure 5.3). This is because the dissociated hydrogen atoms chemically interact with the TM atoms as depicted in their PDOS (Figure 5.3(a-c)) that the H 1s states are broadened and largely overlap with the TM 3d states in the region of  $-2.5$  to  $-7.5$  eV below the Fermi level ( $E_F$ ). On the other hand, the degree of charge transfer is much lower (0.02  $|e|$  in Figure 5.3(b)) for weak molecular adsorption at the Mg site which is consistent with the PDOS that displays negligible overlap of H 1s – Mg 3p states (Figure 5.3(d)). The Kubas adsorption at the Ni sites exhibit larger charge transfer than that of molecular adsorption but smaller than that of dissociative adsorption, thus the adsorption energies of Kubas mode situate between molecular and dissociative adsorption energies (Figure 5.3(b)). The PDOS of Kubas adsorption mode at the Ni site reveals partial overlap between the hydrogen molecular orbital and the Ni 3d states at  $-8.50$  eV below the Fermi level, as shown in Figure 5.3(e). Interestingly, a significantly larger charge transfer (1.95  $|e|$ ) can occur upon dissociative adsorption on the Mg(0001) surface (Figure 5.3(b)). However, the adsorption is much weaker ( $E_{\text{ads}} = -0.12$  eV) than dissociative adsorption at V and Ni sites. This may attribute to the limited interaction with fully occupied Mg 2p states as depicted in Figure 5.3(e) and reported in the previous computational work (Paskaš Mamula *et al.*, 2014). The calculated results agree with previous studies describing that Mg exhibits fully occupied p orbitals which cannot accommodate the  $\text{H}_2$  molecular orbital (Banerjee *et al.*, 2008; Chen *et al.*, 2012). The presence of Ni and V facilitates hydrogen adsorption and dissociation as d orbitals of Ni and V can largely hybridize with the hydrogen molecular orbital leading to strong hydrogen adsorption and H–H bond weakening.

Thus, H<sub>2</sub> molecules could spontaneously dissociate, and dissociative hydrogen atoms are dramatically be stabilized. The presence of V sites and the interface sites on V/Mg<sub>2</sub>Ni structure provide additional highly active sites for barrierless H<sub>2</sub> dissociation and strong adsorption in addition to the Ni sites, therefore V/Mg<sub>2</sub>Ni material enhance reactivity of the initial absorption processes of H<sub>2</sub> dissociation and hydrogen adsorption.

### 5.3 Hydrogen diffusion on Mg(0001), Mg<sub>2</sub>Ni(010), and V/Mg<sub>2</sub>Ni(010) surfaces

Diffusion of dissociated hydrogen atoms also plays a crucial role in determining the performance of hydrogen storage materials. In this section, we computationally evaluated hydrogen diffusion kinetics and diffusion behavior of hydrogen atoms on the surface and into the subsurface of Mg(0001), Mg<sub>2</sub>Ni(010), and V/Mg<sub>2</sub>Ni structures.

#### 5.3.1 Hydrogen diffusion behavior on Mg(0001) surface

We first examined the diffusion processes on the Mg(0001) surface where the initial configuration involves two adsorbed hydrogen atoms on the two adjacent three-fold hollow sites. Then, we considered the movement of one H atom to the neighboring site and the other H atom is maintained at the initial adsorbed position. The minimum energy path of a hydrogen atom diffusion was determined using the CI-NEB and Dimer. Computations reveal that the surface diffusion on Mg(0001) structure exhibits a barrier of 0.21 eV and is endothermic with small reaction energy of 0.07 eV. The TS structure involves the H atom located at the bridge site with a slightly shorter Mg-H bond distance than that of the initial state by 0.08 Å (1.91 vs 1.99 Å), as shown in Figure 5.4(a).

A higher diffusion barrier was found for subsurface diffusion where the H atom diffuses downward into the hollow site between surface and subsurface, as shown in Figure 5.4(b). The diffusion process into subsurface is considered essential to determine absorption kinetics of materials. The transition state structure exhibits a Mg-H bond of 2.02 Å. The calculated subsurface diffusion barrier of 0.49 eV and reaction energy of 0.32 eV are greater than those of surface diffusion as shown in Figure 5.4(b).

This indicates that subsurface diffusion is substantial thermodynamically and kinetically less favorable than surface diffusion. The calculated results are consistent with the previous computational work reported that the subsurface diffusion is relatively difficult showing diffusion barrier in the range of 0.47 eV - 0.59 eV on clean Mg(0001) surface (Chen *et al.*, 2012; Han *et al.*, 2021).

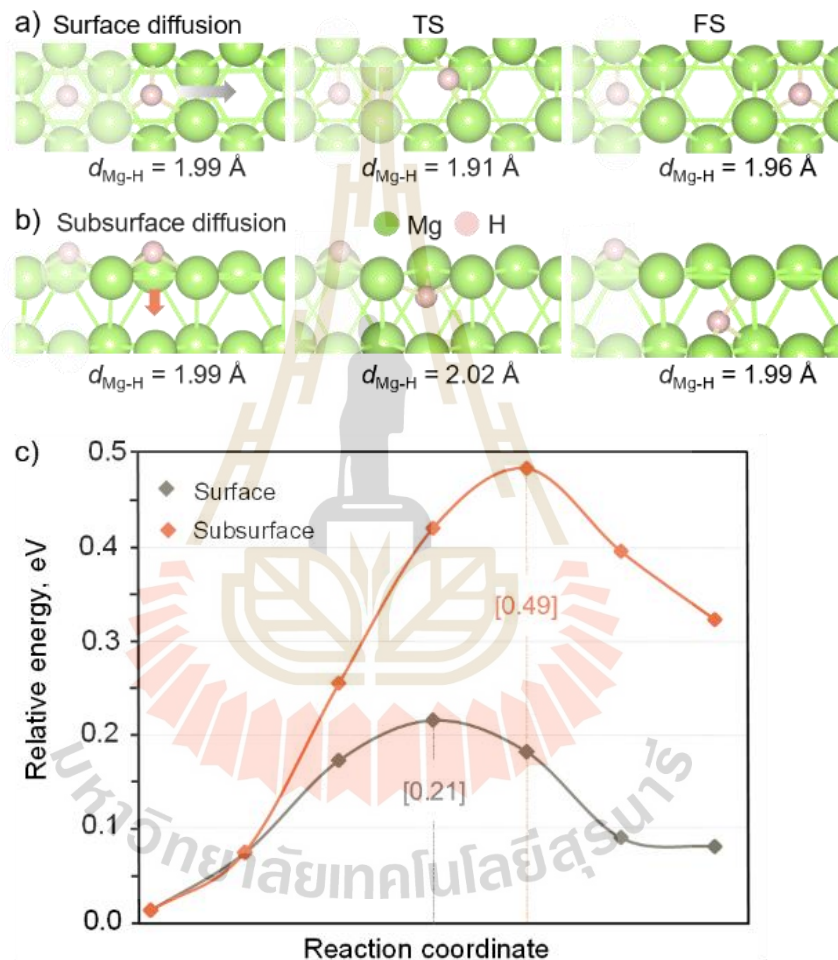


**Figure 5.4** Schematic illustrations of the most favorable diffusion paths for (a) surface and (b) subsurface diffusion on Mg(0001) surface with (c) their corresponding potential energy profiles. Labeled numbers in the brackets indicate diffusion barriers of the diffusion process.

### 5.3.2 Hydrogen diffusion behavior on $\text{Mg}_2\text{Ni}(010)$ surface.

Next, we examined various surface diffusion paths on the  $\text{Mg}_2\text{Ni}(010)$  surface. Three distinct diffusion paths of one H atom moving from the initial site to the neighboring site were explored as follows:  $A \rightarrow B$ ,  $C \rightarrow D$ , and  $C \rightarrow A$ . We considered the diffusion between the two most stable sites on the surface, i.e., Ni-Ni bridge site where the initial position is (A) and the final position (B), as shown in Figure 5.5(a).

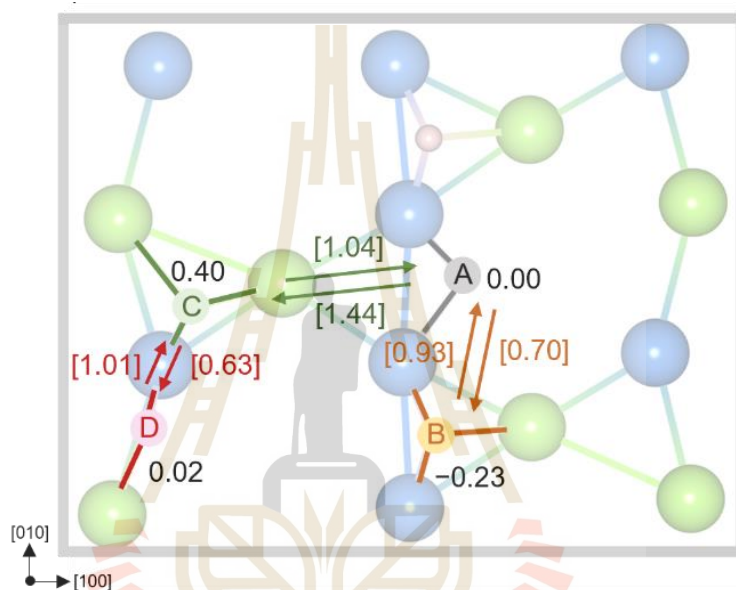


**Figure 5.5** Schematic illustration of all considered surface diffusion paths and the corresponding diffusion barriers and reaction energies for surface diffusion. The diffusion barriers and relative energies are labeled as numbers with and without bracket, respectively. All energies are in eV.

The diffusion from A to B site, denoted as  $A \rightarrow B$ , exhibits a barrier of 0.70 eV with exothermic reaction energy of  $-0.23$  eV. Alternatively, surface diffusion may occur at less stable sites for hydrogen adsorption, as shown in Figure 5.5. The diffusion between two less stable sites i.e., Ni-Mg-Mg hollow site (C) and bridging Ni-Mg site (D), is also examined. The  $C \rightarrow D$  diffusion path yields energy barrier of 0.63 eV and exothermic reaction energy of  $-0.38$  eV which the barriers are comparable to those of

the A→B diffusion path. Both diffusion paths are in the [010] direction where Ni atoms (A→B) or Ni/Mg atoms (C→D) are aligned in [010] direction. Diffusion across the Ni rows along the [100] direction i.e. C→A diffusion path, is substantially more kinetically limited showing significantly higher energy barrier of 1.04 eV, as seen in Figure 5.5. Note that all the reported diffusion barriers are of the exothermic processes whereas the movements in the opposite directions result in endothermic diffusion with larger barriers, as noted in Figure 5.5. The results suggest that H<sub>2</sub> molecules rapidly dissociate and cover most active sites of the Mg<sub>2</sub>Ni(010) surface whereas the surface diffusion hardly occurs due to relatively high energy barrier of 0.6 – 0.7 eV and limited available surface sites.

It can be seen that hydrogen diffusion along the [010] direction is more facile than those of other directions. This is because hydrogen strongly interacts with Ni atoms on the surface. In the [010] direction, Ni atoms directly connect with each other forming “connected Ni sites” and provide low-lying energy paths for hydrogen diffusion. Such favorable diffusion paths on the connected Ni sites are also expected for subsurface diffusion. As shown in Figure 5.6, the subsurface diffusion is kinetically and thermodynamically more favorable when the H atom moves from the adsorption sites with a lower ratio of Ni/Mg to the higher ones in subsurface.

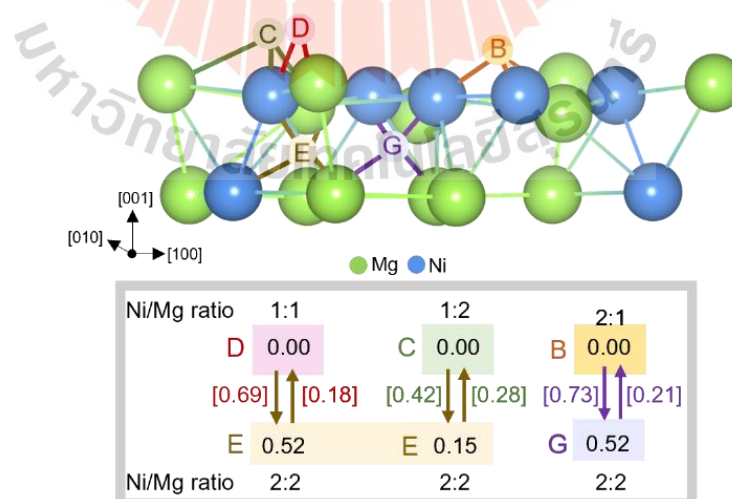


**Figure 5.6** Schematic illustration of all considered diffusion paths and the corresponding diffusion barriers and reaction energies for subsurface diffusion.

The diffusion barriers and relative energies are labeled as numbers with and without bracket, respectively. All energies are in eV. The Ni/Mg ratios indicate the nearest-neighbor environment of the H atom at different adsorption sites.

For instance, the C→E subsurface diffusion path displays a relatively low barrier of 0.42 eV and reaction energy of 0.15 eV while the B→G and D→E subsurface diffusion paths require higher barriers and reaction energies. It can be seen that all considered subsurface diffusion paths are endothermic implying that the insertion of hydrogen at the sublayer is energetically less favorable than surface adsorption. However, the subsurface diffusion barriers are significantly smaller than surface diffusion barriers suggesting that the adsorbed H atoms are likely to diffuse into Mg<sub>2</sub>Ni material. Our calculated results are consistent with the other computational study which reported a similarly preferred diffusion path via connected Ni sites for subsurface diffusion in Mg<sub>2</sub>Ni(010) surface (Zhang *et al.*, 2017). Their calculated diffusion barriers in the range of 0.55 - 1.06 eV (Zhang *et al.*, 2017) are also similar to our work (0.42 - 0.73 eV).

### 5.3.3 Hydrogen diffusion behavior on V/Mg<sub>2</sub>Ni(010) surface.

The influence of the V cluster was shown to promote spontaneous H<sub>2</sub> dissociation and strong hydrogen adsorption. Initially, two H atoms prefer to adsorb at the hollow sites on the V cluster. To further facilitate hydrogen storage process, the dissociative adsorbed H atoms are anticipated to easily diffuse into the Mg<sub>2</sub>Ni material which could occur either directly through the V cluster or via hydrogen spillover from the cluster to the Mg<sub>2</sub>Ni surface and subsequently diffuse into the subsurface. Five different diffusion paths (path A - E) on V/Mg<sub>2</sub>Ni(010) surface were studied, as shown in Figure 5.7(a).

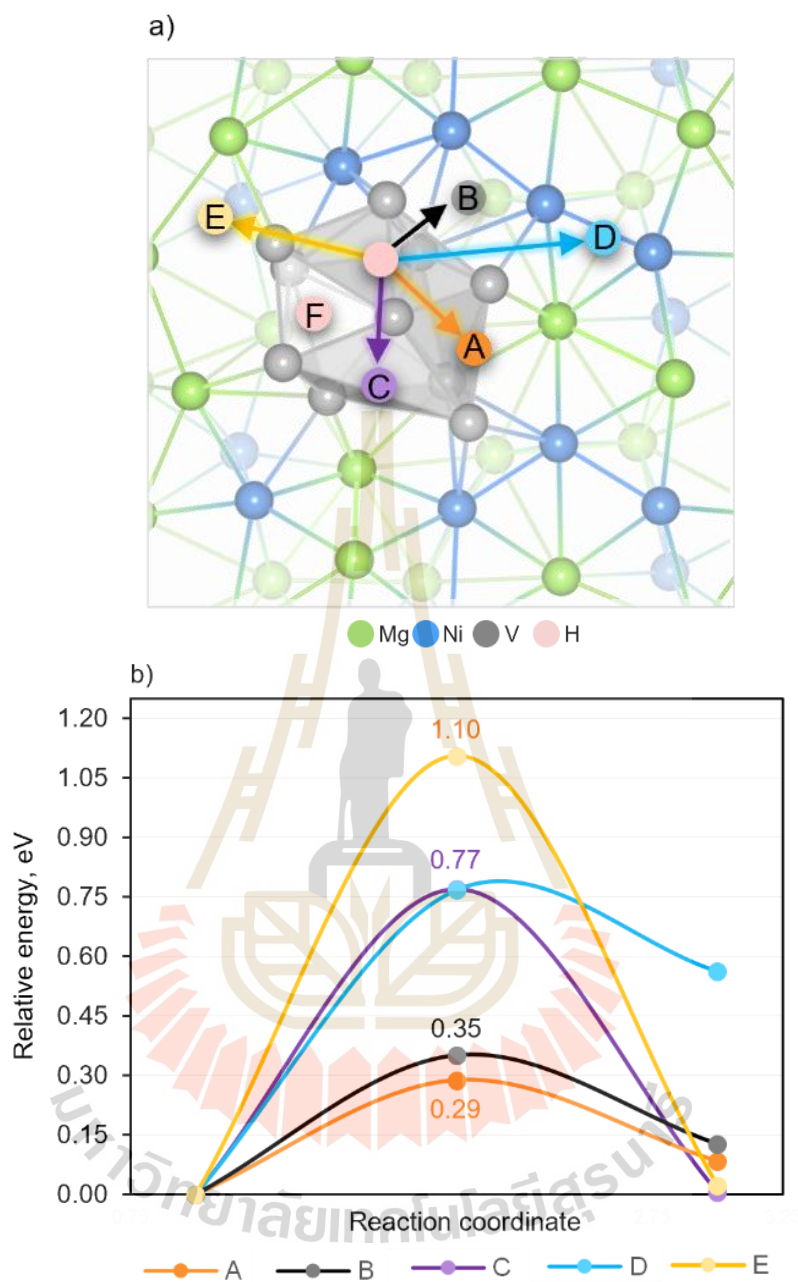


**Figure 5.7** Schematic illustration for (a) different surface diffusion paths (A-E) on the  $V/Mg_2Ni(010)$  surface in top view and (b) the corresponding energy profiles. Labeled numbers indicate the diffusion barriers in eV.

The two most energetically favorable paths are paths A and B where diffused H moves out of V hollow site toward the next hollow on a cluster and spillover to the interface. Meanwhile, the other paths established high energy barrier. We find that diffusion through the V cluster (path E) is unlikely due to a significantly high barrier of 1.10 eV, as shown in Figure 5.7(b).

After, we found the two most energetically favorable paths. Various diffusion paths were considered further the cluster diffusion (path A) and spillover (path B), as shown in Figure 5.8(a).

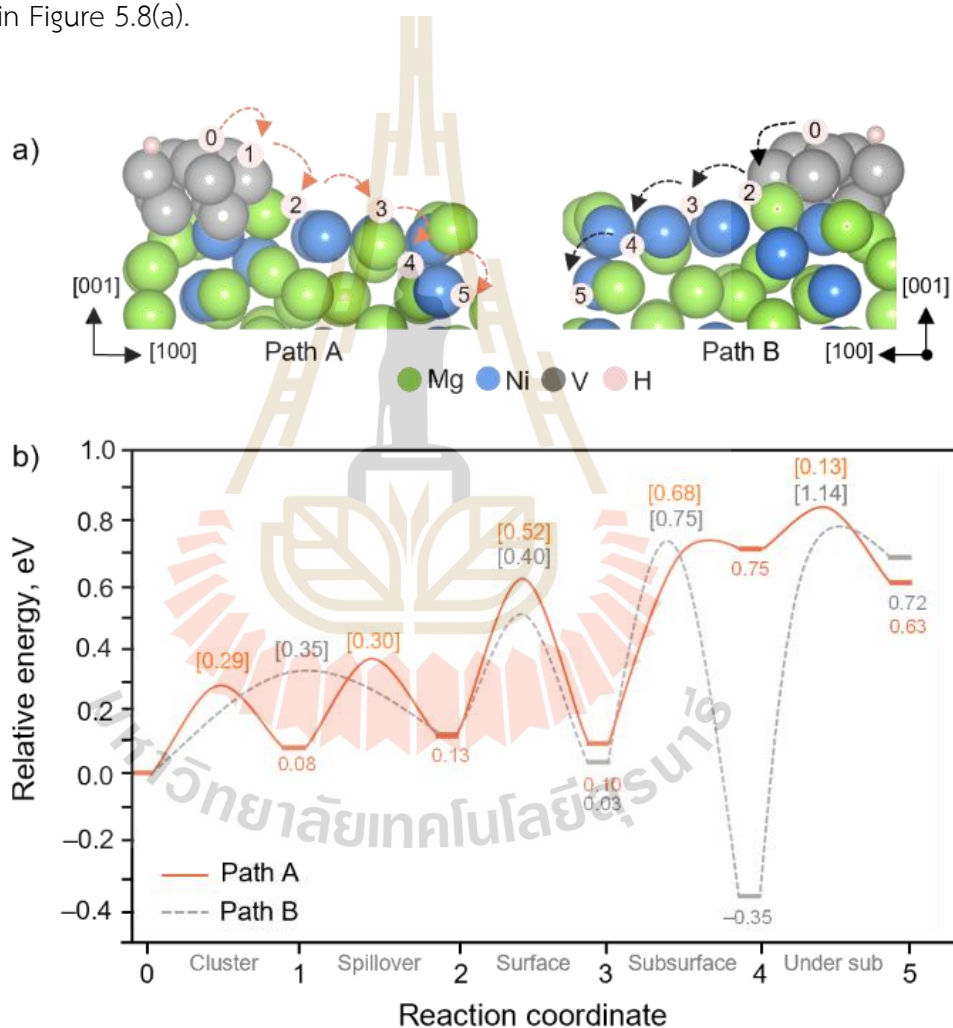


**Figure 5.8** Schematic illustrations of (a) two different diffusion paths, path A (left) and B (right), from V cluster to under-subsurface layer of the V/Mg<sub>2</sub>Ni system with (b) the corresponding potential energy profiles. Labeled numbers with and without brackets indicate diffusion barriers and relative energies, respectively.

The diffusion mechanism includes cluster diffusion ( $0 \rightarrow 1$ ), spillover ( $1 \rightarrow 2$ ), surface diffusion ( $2 \rightarrow 3$ ), subsurface diffusion ( $3 \rightarrow 4$ ), and under subsurface diffusion ( $4 \rightarrow 5$ ). As seen in Figure 5.5(a) (path A), hydrogen diffusion on the V cluster is facile showing the lowest energy barrier of 0.29 eV. The spillover via both paths is similarly favorable where the effective barriers are 0.30 (0.08 + 0.30) eV and 0.35 eV for path A ( $0 \rightarrow 1 \rightarrow 2$ ) and B ( $0 \rightarrow 2$ ), respectively and the reaction energies are slightly endothermic by 0.13 eV. The surface diffusion through path B is slightly more favorable with the barrier of 0.40 eV when compared to path A (0.52 eV). The surface diffusion via both paths is exothermic. Note that the surface diffusion on the  $V_{10}/Mg_2Ni$  surface is kinetically more favorable than those on the  $Mg_2Ni$  surface due to the  $Mg_2Ni$  surface reconstruction upon the deposition of V cluster leading to the formation of the connected Ni sites nearby the cluster which facilitates the spillover and surface diffusion.

The most distinctive point between the two paths is the energy required when the H atom is inserted into the subsurface regions. The subsurface site of path B binds hydrogen considerably stronger than the subsurface site of path A, as shown in Figure 5.9.

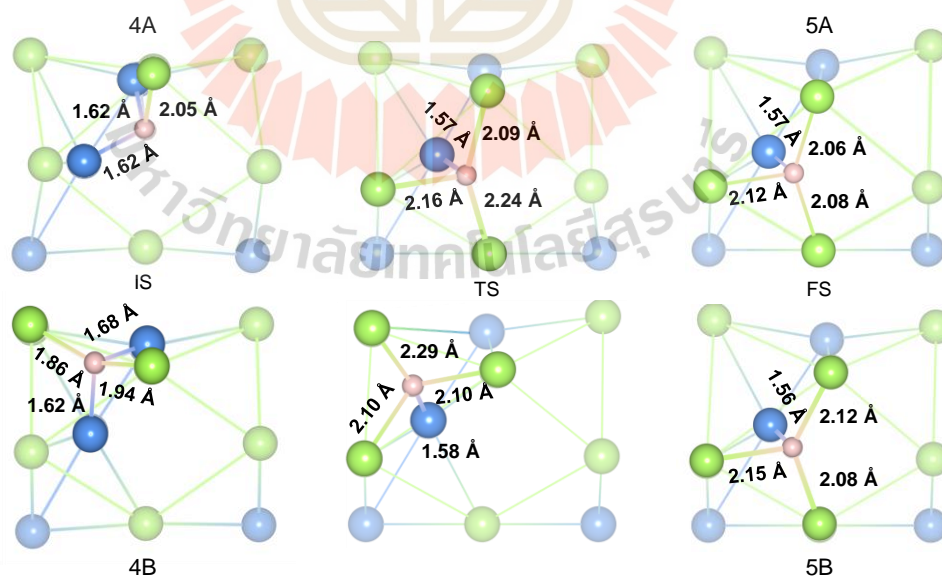


**Figure 5.9** The crystal structure of (side view) diffused H atom jump from the subsurface [left] site to under subsurface diffusion [right] into the bulk  $Mg_2Ni$ .

Only structures at the region near the subsurface and under subsurface sites are shown for clarity. The H-Mg and H-Ni bond lengths surrounded the interstitial site which corresponding to the labelled numbers in crystal structure. The elements are colored as follows: green, Mg; blue, Ni; pink, H.

Thus, the subsurface diffusion through path B becomes highly thermodynamically favorable. This is because, while the surface site of both paths having the same Ni/Mg ratio of 2:1, the subsurface site of path B show a lower Ni/Mg ratio of 2:2 than that of the subsurface site of path A (2:1).

However, their subsurface-diffusion barriers are similar; 0.75 eV and 0.68 eV for path A and B, respectively. Such a stable hydrogen insertion configuration along path B leads to a very high barrier of 1.14 eV for further hydrogen diffusion into the under subsurface whereas the under-subsurface diffusion of path A displays much smaller barrier of 0.13 eV. Thus, the under subsurface diffusion is more feasible to occur at the subsurface site having less strong interaction with hydrogen atom as in path A. On the other hand, the subsurface site that strongly interact with hydrogen as in path B acts as a trapping site where hydrogen does not tend to diffuse into the under subsurface. Overall, the energy profiles indicate that the rate-determining steps for both diffusion paths are essentially in the step of the subsurface diffusion whereas the spillover from cluster to surface is much more facile. The effective barrier for path A of 0.68 eV is somewhat lower than that of path B (0.75 eV) making path A kinetically more favorable. Nevertheless, such high barriers are considered unfavorable for hydrogen diffusion into the bulk materials. High hydrogen coverages may affect the diffusion kinetics which is discussed in the next section.

#### 5.4 Effect of hydrogen coverages

In this section, we examined the behavior of hydrogen adsorption and diffusion at high coverages to account for the effect of high H<sub>2</sub> pressure under storage conditions. To obtain the high coverage systems, we carried out AIMD simulations using canonical NVT ensembles at room temperature with 40 H<sub>2</sub> molecules on the Mg(0001), Mg<sub>2</sub>Ni(010), and V<sub>10</sub>/Mg<sub>2</sub>Ni structures.

The AIMD results showed that in the absence of TM catalysts on Mg(0001) surface, the H<sub>2</sub> molecules hardly adsorb on the surface, as shown in Figure 5.10.

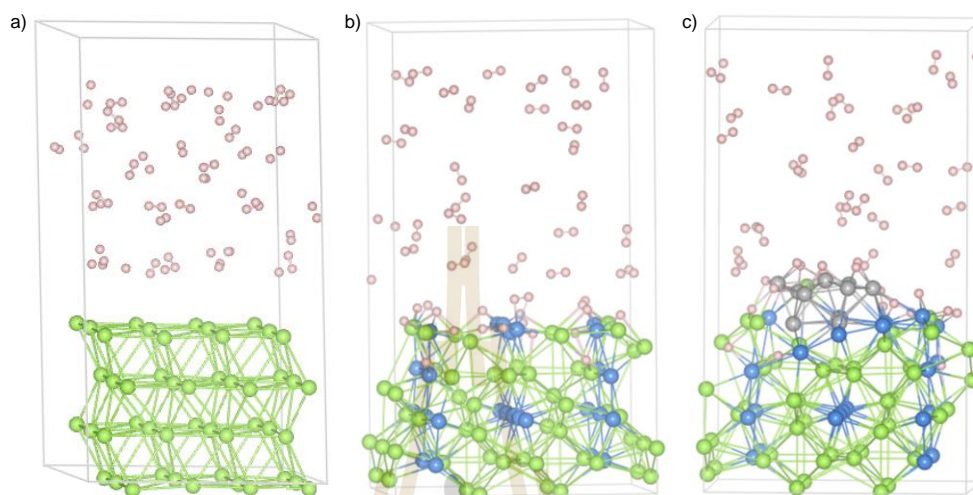


**Figure 5.10** The AIMD results involve 40 H<sub>2</sub> in the system at 30 ps (300 K); a) Mg(0001), b) Mg<sub>2</sub>Ni(010), and V<sub>10</sub>/Mg<sub>2</sub>Ni(010) surface. Green, Mg; blue, Ni; pink, H; gray, V.

The AIMD results are consistent with the DFT calculations at low hydrogen coverage (0.125 monolayer = ML) that H<sub>2</sub> molecules only weakly interact with the surface where the adsorbed molecule maintains its gas-phase structure. Thus, high hydrogen coverage does not promote hydrogen adsorption on Mg(0001) surface. Hydrogen diffusion into the subsurface was not found on Mg(0001) structure during the AIMD simulations of 30 ps.

#### 5.4.1 Effect of hydrogen coverages on Mg<sub>2</sub>Ni(010) surface.

The presence of Ni catalysts on Mg<sub>2</sub>Ni(010) surface, clearly affects hydrogen adsorption behavior. As shown in Figure 5.11, the AIMD results reveal that H<sub>2</sub> molecules simultaneously dissociate and adsorb at the Ni active sites resulting in 16 H atoms, corresponding to 1 ML, on the Mg<sub>2</sub>Ni surface at 30 ps.

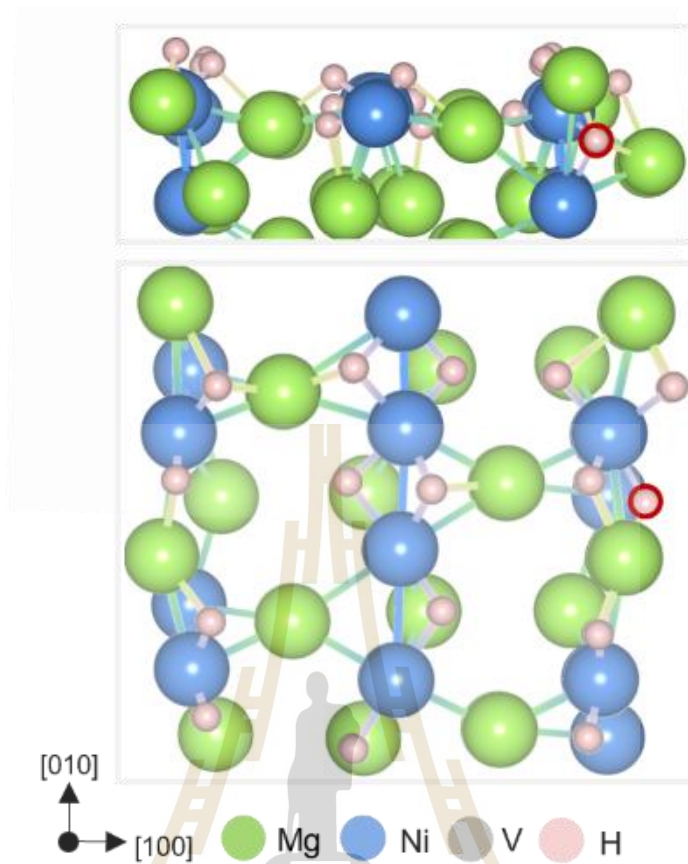


**Figure 5.11** Optimized structures of low-energy configurations obtained from the AIMD simulations for high hydrogen coverage (1 ML) on  $\text{Mg}_2\text{Ni}$  (010) surface including 16 adsorbed H atoms. The subsurface H atoms are marked with red circles.

The most favorable subsurface diffusion path (C→E) obtained from DFT calculations at low hydrogen coverage of 0.125 ML, as shown in Figure 5.6, was also found to be the early subsurface diffusion path seen in AIMD simulations. The calculated barrier of subsurface diffusion C→E at high hydrogen coverages is 0.26 eV which is much lower than that of the low coverages (0.42 eV). This indicates that at high  $\text{H}_2$  pressure of storage conditions, when the  $\text{Mg}_2\text{Ni}$  surface contains high hydrogen coverage, the hydrogen subsurface diffusion is significantly more facile, as shown in Figure 5.12.

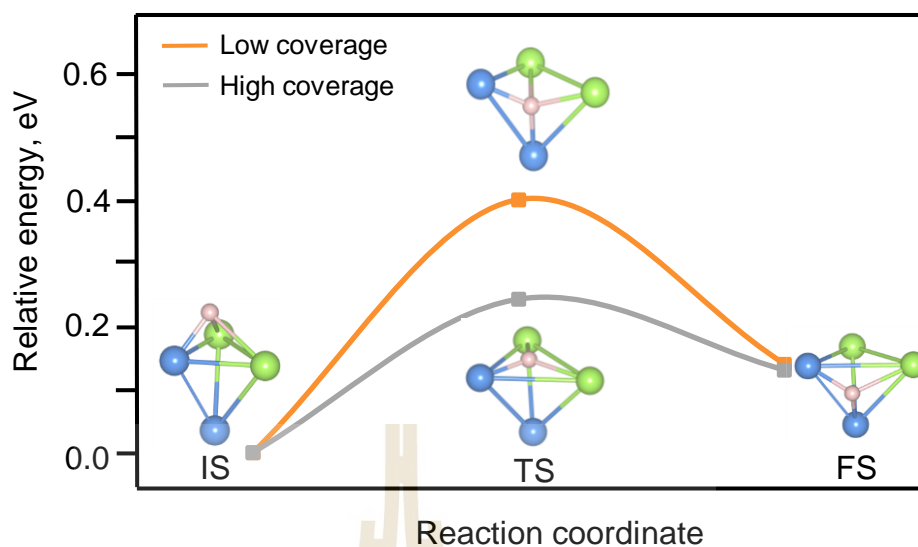


**Figure 5.12** Energy profiles of the most favorable subsurface diffusion on the  $\text{Mg}_2\text{Ni}(010)$  surface at low and high hydrogen coverage. Only structures at the region near the subsurface and under subsurface sites are shown for clarity. The elements are colored as follows: green, Mg; blue, Ni; pink, H.

The subsurface diffusion at low and high coverages are slightly endothermic showing comparable reaction energies (barriers) of 0.15 (0.42) and 0.14 (0.26) eV, respectively. The DFT results agree very well with those observed in AIMD simulations suggesting that subsurface diffusion is kinetically feasible at high hydrogen coverages.

#### 5.4.2 Effect of hydrogen coverages on V/ $\text{Mg}_2\text{Ni}(010)$ surface

The addition of V cluster on  $\text{Mg}_2\text{Ni}$  surface has been shown to enhance hydrogen dissociation and adsorption as discussed in the previous section. The AIMD simulations on the V/ $\text{Mg}_2\text{Ni}$  surface also agree that  $\text{H}_2$  molecules spontaneously dissociate and adsorb on the  $\text{V}_{10}$  cluster and on  $\text{Mg}_2\text{Ni}$  surface. Figure 5.13 shows hydrogen atoms covering the entire V/ $\text{Mg}_2\text{Ni}$  surface where 6 H atoms locate on the V cluster, 6 H atoms at the V- $\text{Mg}_2\text{Ni}$  interface sites, 6 H atoms on the  $\text{Mg}_2\text{Ni}$  surface sites, and 2 H atoms in the subsurface. More adsorbed hydrogen of 20 H atoms (1 ML) was found on the V/ $\text{Mg}_2\text{Ni}$  surface compared to 16 H atoms (1 ML) on  $\text{Mg}_2\text{Ni}$  surface suggests that the addition of V catalysts increased surface adsorption capability.

Furthermore, as shown in Figure 5.13, two H atoms are already undergoing diffusion from the surface into the subsurface via Ni sites in which the subsurface diffusion path agrees very well with the most favorable one (path A, Figure 5.5(a)) found in DFT calculations as discussed earlier.

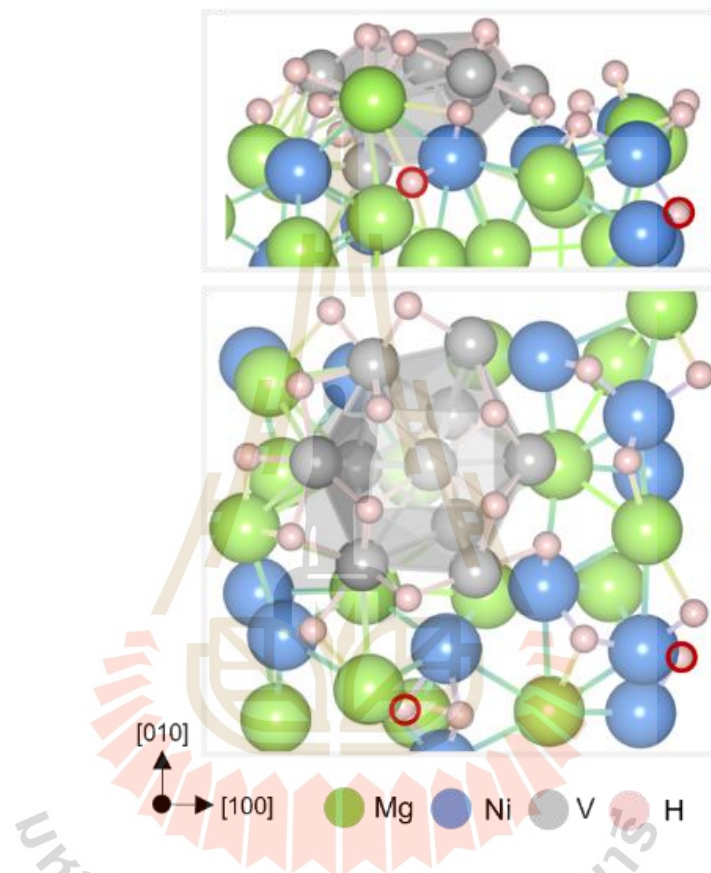


**Figure 5.13** Optimized structures of low-energy configurations obtained from the AIMD simulations for high hydrogen coverage (1 ML) on V/Mg<sub>2</sub>Ni system containing 20 adsorbed H atoms. The subsurface H atoms are marked with red circles.

To examine the effect of hydrogen coverages on the diffusion kinetics on V/Mg<sub>2</sub>Ni material, we calculated diffusion barriers of path A at high hydrogen coverages (1 ML). The diffusion barriers at high coverage are shown in Figure 5.14.

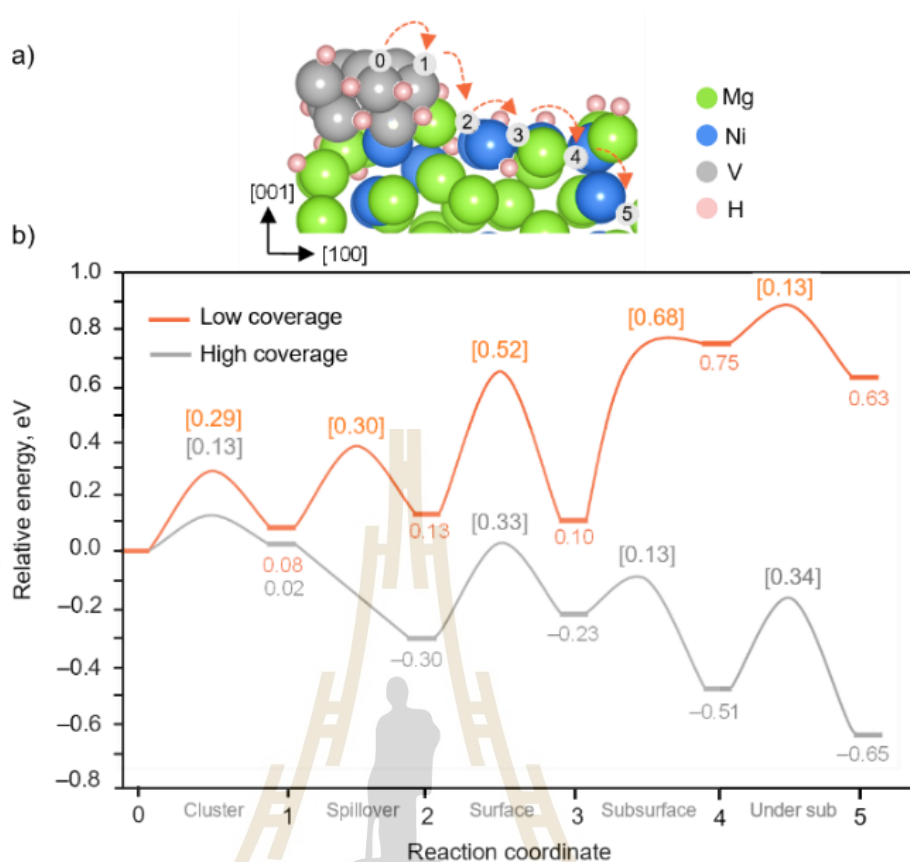


**Figure 5.14** Schematic illustrations of a) hydrogen diffusion from V cluster to under-subsurface layer of the V/Mg<sub>2</sub>Ni system at high hydrogen coverage (1 ML) with b) the corresponding potential energy profiles at low and high coverages. Labeled numbers with and without brackets indicate diffusion barriers and relative energies, respectively.

The results demonstrate that under high coverage, the overall reaction energy becomes highly exothermic suggesting that high coverage strongly influences the hydrogen absorption mechanism to be energetically more favorable. Diffusion kinetics is also accelerated where the barriers of most diffusion steps are decreased compared to those at low hydrogen coverage of 0.10 ML, including cluster diffusion (0.13 vs 0.29 eV), spillover (barrierless vs 0.30 eV), surface diffusion (0.33 vs 0.52 eV), subsurface diffusion (0.13 vs 0.68 eV) and under subsurface diffusion (0.34 vs 0.13 eV). Especially, the rate-determining step of subsurface diffusion becomes much more kinetically and energetically preferred at high coverages.

Our calculated results agree with previous computational works that high hydrogen coverage promote hydrogen diffusion (Chen *et al.*, 2015a, 2015b). For instance, computational studies reported that the generally known difficult step of hydrogen spillover from a TM cluster to oxide surfaces become kinetically and thermodynamically favorable at high hydrogen coverages (Chen *et al.*, 2015a, 2015b).

## 5.5 Conclusion

In this chapter, the synergistic roles of Ni and V catalysts on hydrogen absorption in Mg-based storage materials were investigated using first-principles approaches. The structures of  $\text{Mg}_2\text{Ni}(010)$ , and V cluster supported on  $\text{Mg}_2\text{Ni}$  surfaces were modeled based on experimental characterizations. Behaviors of hydrogen adsorption and diffusion were investigated using these surface models and compared with those of the pristine  $\text{Mg}(0001)$  surface. Computations reveal that both Ni and V catalysts energetically and kinetically improve hydrogen adsorption that  $\text{H}_2$  molecules spontaneously dissociate and strongly interact with the catalysts. Hydrogen dissociation process becomes barrierless on  $\text{Mg}_2\text{Ni}$  and  $\text{V}/\text{Mg}_2\text{Ni}$  surfaces. The electronic structure analysis provides deeper understanding toward their catalytic roles that such strong interactions are originated from the well-overlapped molecular orbitals of adsorbed hydrogen and  $3d$  states of Ni and V atoms. The presence of Ni promotes not only hydrogen dissociation and adsorption process but also subsurface diffusion; however, hydrogen surface diffusion on  $\text{Mg}_2\text{Ni}$  surface could be kinetically limited at low hydrogen coverage. The presence of the V cluster induces surface reconstruction resulting in a formation of more favorable sites i.e., V-Ni bridges and connected Ni sites, for hydrogen adsorption. The presence of V cluster also increases number of strong adsorption sites for hydrogen both on the V cluster and at the V-  $\text{Mg}_2\text{Ni}$  interface, thus hydrogen uptakes are enhanced. In addition, the structure reconstruction upon V deposition also facilitates hydrogen atoms spillover and surface diffusion which are not kinetically limited via V-Ni bridges and connected Ni sites, respectively. The absorption process at low hydrogen coverage on  $\text{V}/\text{Mg}_2\text{Ni}$  structure is kinetically limited by subsurface diffusion.

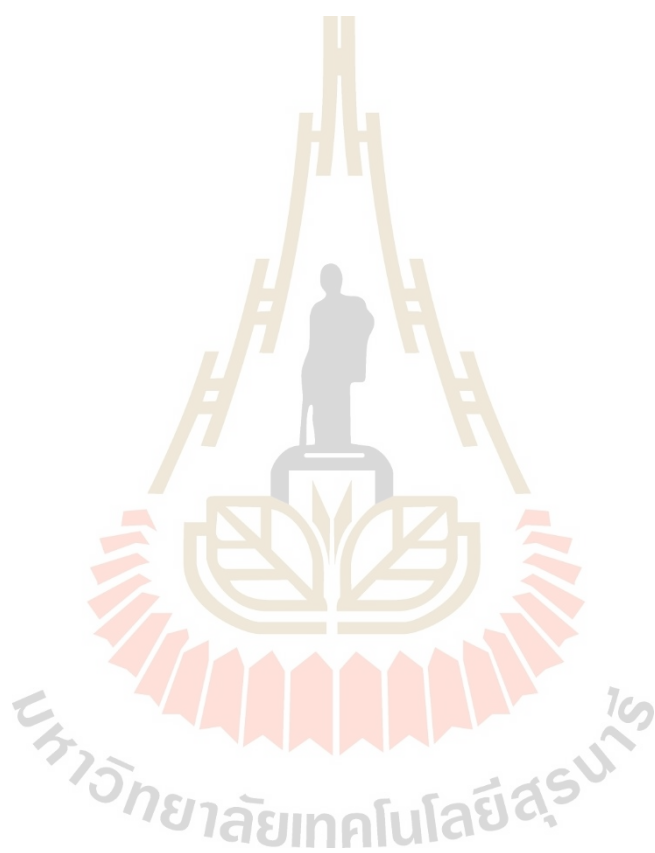
Nevertheless, the kinetics of surface and subsurface diffusion are dramatically improved at high hydrogen coverages. Also, the under-subsurface diffusion becomes significantly thermodynamically favorable at high hydrogen coverages. The computations suggest that the effect of Ni and V catalysts on hydrogen absorption enhancement including hydrogen adsorption and diffusion processes could considerably be pronounced at the operating condition of high H<sub>2</sub> pressure.

## 5.6 References

- Banerjee, S., Pillai, C. G. S., and Majumder, C. (2008). First-Principles Study of the H<sub>2</sub> Interaction With Transition Metal (Ti, V, Ni) Doped Mg(0001) Surface: Implications for H-Storage Materials. *J. Chem. Phys.* *129*, 174703.
- Chen, H.-Y. T., Tosoni, S., and Pacchioni, G. (2015a). Adsorption of Ruthenium Atoms and Clusters on Anatase TiO<sub>2</sub> and Tetragonal ZrO<sub>2</sub>(101) Surfaces: A Comparative DFT Study. *J. Phys. Chem. C.* *119*, 10856.
- Chen, H.-Y. T., Tosoni, S., and Pacchioni, G. (2015b). Hydrogen Adsorption, Dissociation, and Spillover on Ru<sub>10</sub> Clusters Supported on Anatase TiO<sub>2</sub> and Tetragonal ZrO<sub>2</sub>(101) Surfaces. *ACS Catal.* *5*, 5486.
- Chen, M., Cai, Z.-Z., Yang, X.-B., Zhu, M., and Zhao, Y.-J. (2012). Theoretical Study of Hydrogen Dissociation and Diffusion on Nb and Ni Co-Doped Mg(0001): A Synergistic Effect. *Surf. Sci.* *606*, L45.
- Cui, J., Liu, J., Wang, H., Ouyang, L., Sun, D., Zhu, M., and Yao, X. (2014). Mg–TM (TM: Ti, Nb, V, Co, Mo or Ni) Core–Shell like Nanostructures: Synthesis, Hydrogen Storage Performance and Catalytic Mechanism. *J. Mater. Chem.* *2*, 9645.
- Grimme, S. (2006). Semiempirical GGA-type density functional constructed with a long-range dispersion correction. *J. Comput. Chem.* *27*, 1787.
- Han, Z., Wu, Y., Yu, H., and Zhou, S. (2021). Location-Dependent Effect of Nickel on Hydrogen Dissociation and Diffusion on Mg(0001) Surface: Insights Into Hydrogen Storage Material Design. *J. Magnes. Alloy.*
- Henkelman, G., Arnaldsson, A., and Jónsson, H. (2006). A fast and robust algorithm for Bader decomposition of charge density. *Comput. Mater. Sci.* *36*, 354.

- Henkelman, G. and Jónsson, H. (1999). A Dimer Method for Finding Saddle Points on High Dimensional Potential Surfaces Using Only First Derivatives. *J. Chem. Phys.* *111*, 7010.
- Henkelman, G., Uberuaga, B. P., and Jónsson, H. (2000). A climbing image nudged elastic band method for finding saddle points and minimum energy paths. *J. Chem. Phys.* *113*, 9901.
- Kubas, G. J. (1988). Molecular Hydrogen Complexes: Coordination of a  $\sigma$  Bond to Transition Metals. *Acc. Chem. Res.* *21*, 120.
- Ma, L., Zhang, J.-M., and Xu, K.-W. (2014). Hydrogen storage on nitrogen induced defects in palladium-decorated graphene: A first-principles study. *Appl. Surf. Sci.* *292*, 921.
- Momma, K. and Izumi, F. (2011). VESTA 3 for Three-Dimensional Visualization of Crystal, Volumetric and Morphology Data. *J. Appl. Crystallogr.* *44*, 1272.
- Paskaš Mamula, B., Grbović Novaković, J., Radisavljević, I., Ivanović, N., and Novaković, N. (2014). Electronic Structure and Charge Distribution Topology of MgH<sub>2</sub> Doped with 3d Transition Metals. *Int. J. Hydrog. Energy* *39*, 5874.
- Pozzo, M., Alfè, D., Amieiro, A., French, S., and Pratt, A. (2008). Hydrogen Dissociation and Diffusion on Ni- and Ti-Doped Mg(0001) Surfaces. *J. Chem. Phys.* *128*, 094703.
- Sanville, E., Kenny, S. D., Smith, R., and Henkelman, G. (2007). Improved grid-based algorithm for Bader charge allocation. *J. Comput. Chem.* *28*, 899.
- Stihl, C. and Vladimirov, P. V. (2016). Multiscale Modelling of Hydrogen Behaviour on Beryllium (0001) Surface. *Nucl. Mater. Energy.* *9*, 547.
- Xiubo, X., Ming, C., Peng, L., Jiaxiang, S., and Tong, L. (2018). Synergistic Catalytic Effects of the Ni and V Nanoparticles on the Hydrogen Storage Properties of Mg-Ni-V Nanocomposite. *Chem. Eng.* *347*, 145.
- Zhang, Z., Jin, J., Zhang, H., Qi, X., Bian, Y., and Zhao, H. (2017). First-Principles Calculation of Hydrogen Adsorption and Diffusion on Mn-doped Mg<sub>2</sub>Ni(010) Surfaces. *Appl. Surf. Sci.* *425*, 148.

Zou, J., Long, S., Chen, X., Zeng, X., and Ding, W. (2015). Preparation and hydrogen sorption properties of a Ni decorated Mg based Mg@Ni nano-composite. *Int. J. Hydrog. Energy.* 40, 1820.



## CHAPTER VI

### HYDROGEN ADSORPTION ON CARBON-BASED MATERIALS DECORATED WITH Ni NANOPARTICLES

#### 6.1 Introduction

The physisorption on carbon-based materials is mainly found in the alternative hydrogen storage adsorbents due to the high surface area and porosity. In this chapter V, we have shown that the synergetic of TMs catalysts can improve the hydrogen adsorption and facilitate the dissociation of H<sub>2</sub> molecules. This doping strategy is efficient when doping with TMs on carbon-based materials. Both experimental and theoretical studies found that adding transition metal to carbon-based materials can help the hydrogen storage performance. However, doping the other element as transition metal or heteroatom on adsorbents as a catalyst can be enhanced the hydrogen sorption enthalpy and improve the interaction between hydrogen and adsorbents.

Furthermore, the effect of TMs has been investigated on defect graphene found that the combination of TMs nanoparticle and heteroatom dope on graphene (defect with heteroatoms) can improve the hydrogen adsorption and hydrogen spillover. Ni nanoparticle is commonly used as a catalyst doped into the carbon-based material due to their abundance, availability, and low cost. This chapter proposed that the experimental observations agree with our computational study. The present research synthesizes the Ni-doped on carbon-based materials used by different carbon sources. According to the N- and O-rich in the carbon sources, the adsorbent defect was found, as evidenced by their IR and XPS spectra (Plerdsranoy *et al.*, 2021; Thaweelap *et al.*, 2021). To obtain insight into Ni-doped carbon-based materials that enhanced the hydrogen storage capacity, the first-principles methods were employed to study interactions between Ni cluster and the surfaces, the behavior of H<sub>2</sub> adsorption, and their structural and electronic properties.

## 6.2 Computational details

Spin-polarized density functional theory (DFT) calculations as implemented in Vienna ab initio Simulation Package (VASP 5.3) (Kresse and Furthmüller, 1996; Perdew *et al.*, 1996) were carried out to study Ni-substrate interactions and behavior of H<sub>2</sub> adsorption. The interaction between nuclei and core electron was described using the projector augmented wave (PAW) method (Kresse and Joubert, 1999). The generalized gradient approximation (GGA) with Perdew-Burke-Ernzerhof (PBE) functional was used to describe the exchange-correlation term (Perdew *et al.*, 1996). The plane wave cut-off energy was set to 500 eV for all calculations. Moreover, the van der Waals interactions were included using the DFT-D3 method of Grimme correction (Grimme, 2006; Grimme *et al.*, 2010). Structural optimizations and electronic energy calculations were carried out using the energy convergence criterion of 10<sup>-6</sup> eV with residual force on each atom smaller than 0.02 eV/Å.

The Monkhorst-Pack k-point mesh of 3×3×1 was employed to sample the Brillouin zone (Monkhorst and Pack, 1976). The vacuum gap of 15 Å was added in the normal direction to avoid the interactions between periodic images. The charge was analyzed by means of Bader charge calculations (Henkelman *et al.*, 2006; Sanville *et al.*, 2007). To study the adsorption behavior of Ni<sub>13</sub> decorated on the different substrates, we carried out *ab initio* molecular dynamic (AIMD) simulations in an NVT ensemble at 300 K using the Nosé-Hoover thermostat (Nosé, 1984). Due to the large supercells, Brillouin zone integrations were sampled only at the  $\Gamma$ -point. The time-step of 0.5 fs was employed for 10 ps.

To directly compare the calculated atomic structure model with the experiment result and study the role of white line changing, the XANES spectrum was simulated. The fully relaxed structure of the Ni<sub>13</sub> cluster on pyrrolic graphene obtained from DFT calculation was used as input coordinates for FEFF8.2 codes (Rehr *et al.*, 2009), employed to calculate selected Ni K-edge XANES spectrum based on the multiple-scattering expansion within the muffin-tin potentials. The Hedin-Lundqvist (Hedin and Lundqvist, 1971) was used as the exchange-correlation potential with an imaginary part of 0.5 eV to simulate the experimental broadening.

The radii for self-consistent potential and full-multiple scattering calculations were set at 0.80 nm, respectively.

### 6.3 Hydrogen adsorption of O/N-rich hierarchical carbon scaffold decorated with Ni NPs

This work considered two different surface models, i.e., the defect-free surface and the HCS surface model. The defect-free model was simply represented using a pristine graphene sheet. The HCS surface model was modeled considering the presence of nitrogen and oxygen heteroatoms, as evidenced from our IR and XPS spectra. Pyridinic and epoxy groups were used to represent nitrogen and oxygen heteroatoms, respectively, since these functional groups are commonly found in various carbon materials (Bian *et al.*, 2015; Li *et al.*, 2017; Liu *et al.*, 2012).

#### 6.3.1 Model development

The Ni nanoparticles were modeled as an icosahedral Ni<sub>13</sub> cluster. Interactions between the Ni<sub>13</sub> cluster and the surfaces were described by the binding energy,  $E_b$ , which can be calculated as follow.

$$E_b = (E_{\text{surface}} + E_{\text{Ni}_{13}}) - E_{\text{Ni/surface}} \quad (6.1)$$

where  $E_{\text{Ni/surface}}$  is the total energy of the Ni<sub>13</sub> on the pristine graphene or defect graphene system;  $E_{\text{Ni}}$  is the total energy of the isolated Ni<sub>13</sub> cluster; and  $E_{\text{surface}}$  is the total energy of the bare pristine graphene or defect graphene sheet.

Computations show that the Ni<sub>13</sub> cluster binds more strongly to the defect graphene sheet ( $E_b = 5.41$  eV) than the pristine graphene ( $E_b = 2.88$  eV). As shown in Figure 6.1(a), the optimized structure of the Ni supported on pristine graphene exhibits a face-on configuration of the Ni<sub>13</sub> cluster where three Ni atoms are on the hollow site of the graphene sheet with an average Ni-C distance of 2.37 Å. On the other hand, the Ni<sub>13</sub> cluster effectively binds to the N and O heteroatoms of the defect graphene with average Ni-N distance of 1.98 Å and Ni-O distance of 2.17 Å, as shown in Figure 6.1(b). Bader charge analysis reveals that the Ni<sub>13</sub> cluster donates its electron to the surfaces

upon Ni deposition where larger charge transfer was observed for the defect graphene (1.14 e<sup>-</sup> vs. 0.77 e<sup>-</sup>), as shown in Figure 6.1 panel a and b.

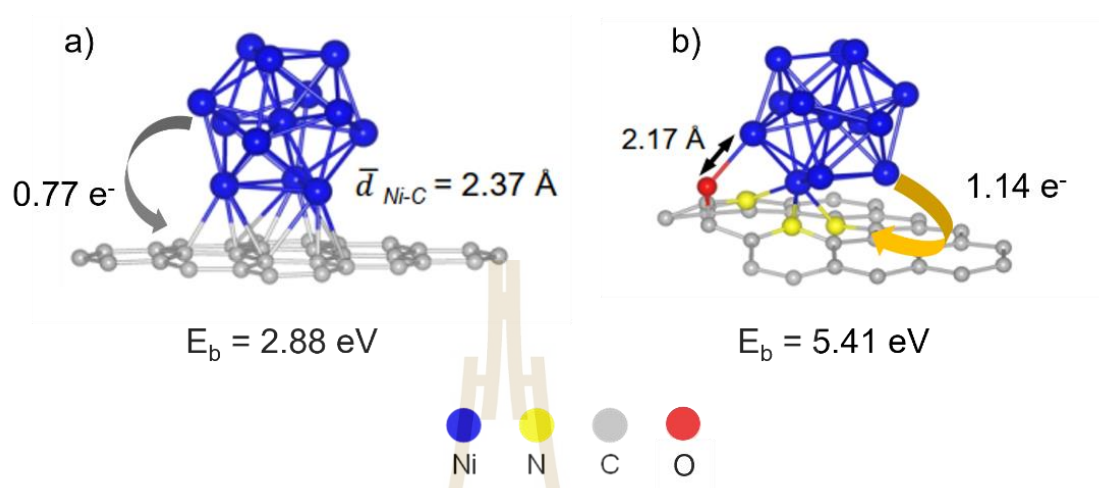


**Figure 6.1** The optimized structures of the Ni<sub>13</sub> cluster supported on pristine a) graphene and b) defected graphene. The calculated cluster-support binding energies,  $E_b$ , are labeled. The numbers of electron gain/loss by each species are indicated.

The optimized structures and charge analysis agree very well with the calculated  $E_b$ , confirming that the heteroatom (N, O) doping improves Ni-substrate interactions. Such strong interactions could inhibit Ni sintering upon hydrogen sorption leading to superior hydrogen storage capability and long cycle life.

### 6.3.2 Hydrogen adsorption on the defect-free surface and the HCS surface model.

Next, the behavior of hydrogen adsorption was examined using AIMD simulations where 20 H<sub>2</sub> molecules were included in an NVT canonical ensemble at 300 K with a simulation time of 10 ps. Low-energy configurations obtained from the AIMD results were then optimized using the DFT method. Computations reveal similar behavior of H<sub>2</sub> adsorption on both Ni-supported pristine and doped graphene systems where two different adsorption modes are identified. The H<sub>2</sub> adsorbed structures of both systems include dissociative adsorption of 10 hydrogen atoms and Kubas-mode

(Kubas, 2001; López-Corral *et al.*, 2011) adsorption of 9 H<sub>2</sub> molecules on the Ni<sub>13</sub> cluster. The adsorption energy per H<sub>2</sub> molecule,  $E_{\text{ads}}$ , can be calculated as

$$E_{\text{ads}} = [E_{\text{H}_2+\text{Ni}_{13}/\text{surface}} - (n_{\text{H}_2}E_{\text{H}_2} + E_{\text{Ni}_{13}/\text{GP}})]/n_{\text{H}_2} \quad (6.2)$$

where  $E_{\text{H}_2+\text{Ni}_{13}/\text{surface}}$  and  $E_{\text{Ni}_{13}/\text{GP}}$  are the total energy of the systems in the presence and absence of H<sub>2</sub> adsorption, respectively.  $E_{\text{H}_2}$  is the total energy of a H<sub>2</sub> molecule in the gas phase.

The calculated results reveal insignificant differences of  $E_{\text{ads}}$  for the Ni-supported on pristine graphene (−0.93 eV) and doped graphene systems (−0.87 eV/mol). In addition, Bader charge analysis shows that, upon adsorption, the Ni<sub>13</sub> cluster gives electrons to the adsorbed hydrogen. The number of electrons of adsorbed hydrogen is increased by 2.40 e<sup>−</sup> which are mainly transferred from the Ni<sub>13</sub> cluster (−2.30 e<sup>−</sup>) for both systems. Overall, the calculated results indicate that the heteroatom (N, O) doping has negligible effects on the behavior of hydrogen adsorption. Nevertheless, it strengthens interactions between the Ni<sub>13</sub> cluster and the support, which could improve Ni distribution and lead to better hydrogen storage capability.

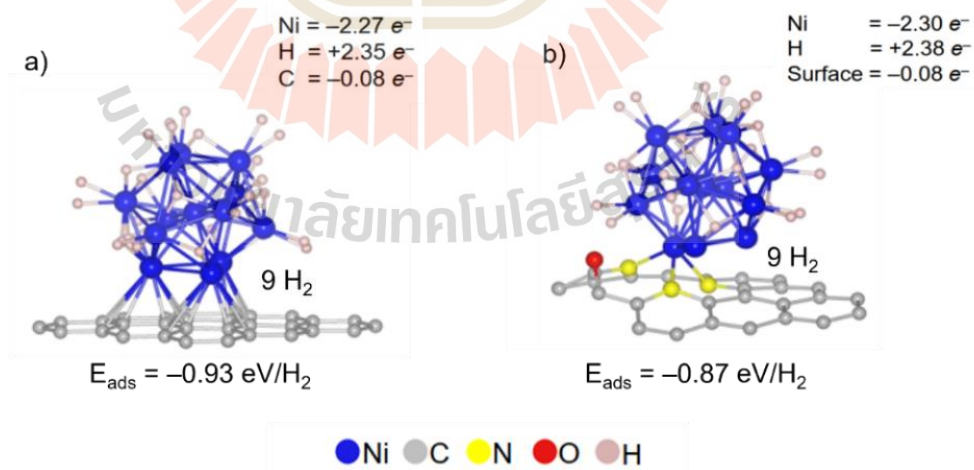


**Figure 6.2** The optimized H<sub>2</sub> adsorbed structures are illustrated on pristine a) graphene and b) defected graphene, respectively. The calculated H<sub>2</sub> adsorption energy per H<sub>2</sub> molecule,  $E_{\text{ads}}$ , is labeled.

The measured and simulated XANES spectra confirm the behavior of charge transfer. The simulated Ni K-edge XANES spectra of Ni supported defect graphene in the absence and presence of H<sub>2</sub> coverages are shown in Figure 6.3. Note that for Ni K-edge XANES, the simulated spectra are the selected spectra obtained from Ni atom, which interact with N and nearest O on the defect graphene.

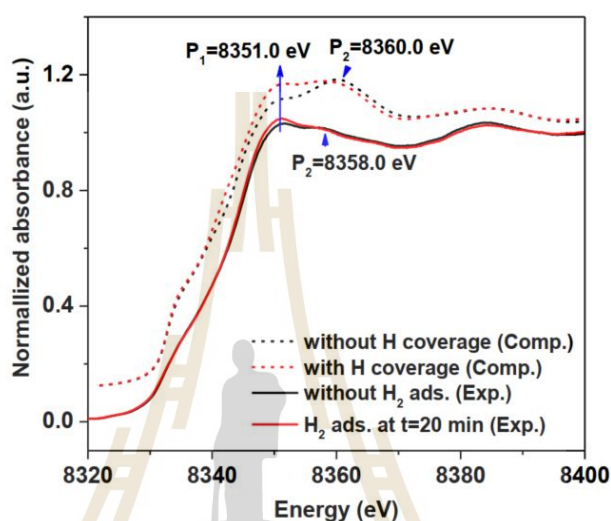


**Figure 6.3** The simulated XANES spectra of Ni K-edge of the Ni<sub>13</sub> cluster supported on defect graphene in the absence (Figure 6.1) and presence of hydrogen coverage (Figure 6.2)

When comparing the plots to the measured spectra from experiment data, it is found that besides an overall shift of about 10 eV, the spectra contain two peaks (denoted as P1 and P2) consistent with those observed in the samples. It can be seen from the experimental spectra that the height of the P1 peak, so-called white line, depends strongly on the H absorption process, while the P2 peak decreases as the reduction time increases. Likewise, the simulated H adsorption process (Figure 6.2) exhibits similar behavior where the white line intensity increases upon the adsorption. Our simulated spectra such character that the white line shifts toward higher intensity when H<sub>2</sub> adsorbs on the Ni<sub>13</sub> cluster. The increased white-line intensity reflects the lower occupation number of the Ni cluster suggesting the transfer of electrons from the Ni cluster to the adsorbed hydrogen.

## 6.4 Ni-doped activated carbon nanofibers for storing hydrogen at ambient condition

According to the experimental observations, ACNF\* samples contain graphitic lattice and disordered  $sp^3$  carbons (Raman spectra) with non-negligible nitrogen contents (IR spectra). Hence, for simplicity, we used nitrogen (N)-doped graphene as a model for ACNF\* surface where the pyrrolic defect was created upon N doping, as shown in Figure 6.4 (a). Such N-doped structure was reported as one of the most common configurations under experimental conditions (Rangel *et al.*, 2016).

### 6.4.1 Model developments of Ni supported pyrrolic graphene model

To represent the Ni catalysts, the icosahedral  $Ni_{13}$  cluster was placed onto the pyrrolic graphene model where the tip of the  $Ni_{13}$  cluster was at the vacancy site and formed three Ni–N bonds. Such a configuration is consistent with our XPS results in Ni–N coordination, where direct N–C bond is absent. The optimized structure reveals that the tip Ni atom effectively binds to three N atoms with an average Ni–N bond distance of 1.89 Å, as shown in Figure 6.4. Such N-doped structure was reported as one of the most common configurations under experimental conditions (Rangel *et al.*, 2016).

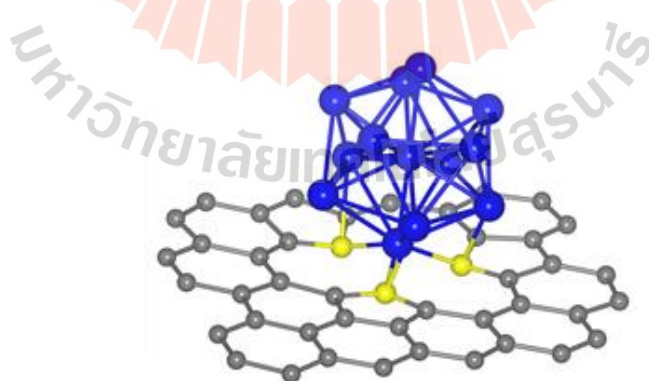


**Figure 6.4** The optimized structures of  $Ni_{13}$  cluster supported on pyrrolic graphene in the absence. The electron transfer is schematically depicted by the colors of each

atom, where the positive and negative values describe electron gains and losses, respectively. The labeled numbers represent each atomic species in the total number of electrons gained/lost.

The calculated  $E_b$  of 8.56 eV agrees with previously calculated values where the  $E_b$  of Ni<sub>13</sub> on the pristine graphene are in the range of 7.42 and 8.02 eV (Montejo-Alvaro *et al.*, 2019; Sahoo *et al.*, 2014). The other works used different metal clusters supported on N-doped graphene also exhibit comparable  $E_b$ , 7.62 eV for Ag<sub>8</sub> and 8.33 eV for Pt<sub>14</sub> cluster (Jalili *et al.*, 2017; Tian *et al.*, 2015). Such high binding energy indicates a strong interaction between the cluster and the pyrrolic graphene. The calculated results imply that the supported Ni particles effectively bind to the ACNF\* surface and tend not to agglomerate upon adsorption-desorption cycling, as evidenced by our experimental observations. In addition, the Bader charge analysis (Henkelman *et al.*, 2006; Sanville *et al.*, 2007) shows that upon adsorption, the Ni cluster gives electrons to the support where 1.98 e<sup>-</sup> were transferred from the cluster. As schematically depicted in Figure 6.5, these electrons were mainly located at the relatively high electronegative N atoms (+1.68 e<sup>-</sup>) where small fractions are delocalized throughout the graphene sheet (+0.30 e<sup>-</sup>).

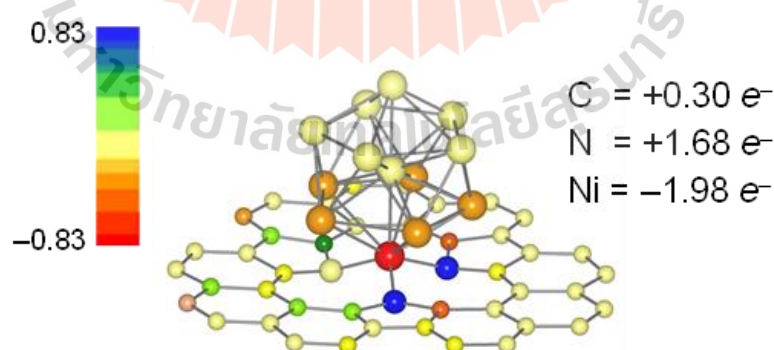


**Figure 6.5** The electron transfer is schematically depicted by the colors of each atom, where the positive and negative values describe electron gains and losses, respectively. The labeled numbers represent the total number of electrons gained/lost by each atomic species.

### 6.4.2 Hydrogen adsorption on Ni supported pyrrolic graphene model

The behavior of H<sub>2</sub> adsorption was examined using AIMD simulations where 20 H<sub>2</sub> molecules were included in an NVT canonical ensemble at 300 K for 1 ps. Upon simulations, H<sub>2</sub> molecules dissociatively adsorb on the Ni<sub>13</sub> cluster where strong interactions between H<sub>2</sub> molecules and the graphene is absent. A low energy configuration was selected to further carry out static structural optimization using DFT where only adsorbed hydrogen atoms were included in the calculation. Computations reveal that the optimized structure contains 20 H atoms (10 H<sub>2</sub> molecules) adsorbed on the hollow sites and top sites of the Ni<sub>13</sub> cluster. The calculated adsorption energy of -1.21 eV/H<sub>2</sub> molecule indicates a strong chemisorption character with an average Ni-H bond distance of 1.71 Å. The chemisorbed hydrogen slightly affects the local structure of the Ni<sub>13</sub> cluster with elongation of Ni-Ni bond distance up to 36 pm as compared with the cluster without H<sub>2</sub> adsorption.

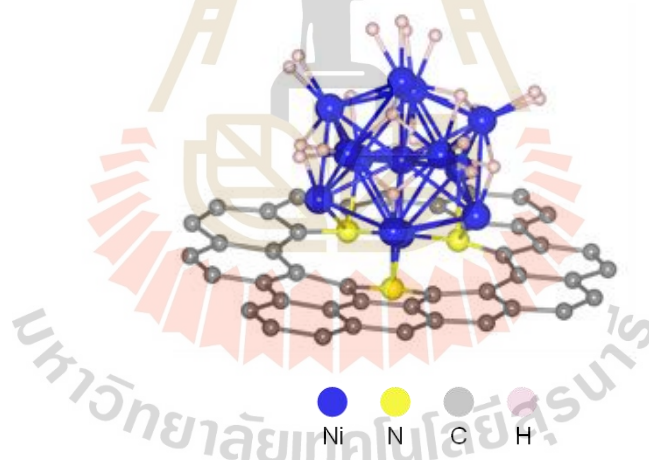


**Figure 6.6** The optimized structures H<sub>2</sub> adsorbed on Ni<sub>13</sub> cluster supported on pyrrolic graphene in the absence.

The Bader charge analysis was carried out to gain insight into the binding character of the adsorbed hydrogen. It can be seen from Figure 6.5 that, upon adsorption, electrons are transferred from the Ni<sub>13</sub> cluster to H atoms as the number of electrons of the Ni<sub>13</sub> cluster is depleted by 2.63 e<sup>-</sup> where they are mainly transferred to the adsorbed hydrogen atoms (+2.60 e<sup>-</sup>). The calculated results are consistent with

the commonly known character of metal–hydrogen bonds, where metal usually shares electrons with hydrogen.

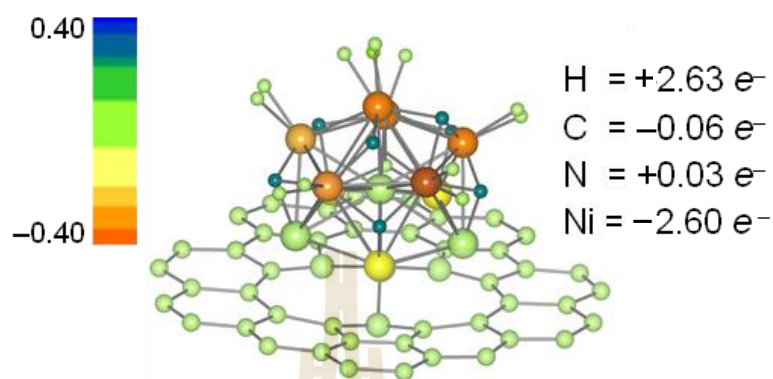


**Figure 6.7** The electron transfer is schematically depicted by the colors of each atom where the positive and negative values describe electron gains and losses, respectively. The labeled numbers represent the total number of electrons gain/loss by each atomic species.

The measured and simulated XANES spectra confirm this behavior of charge transfer. The simulated Ni *K*-edge XANES spectra of different hydrogen coverages on Ni-supported pyrrolic graphene are shown in Figure 6.6. Note that for Ni *K*-edge XANES, the simulated spectra are the selected spectra obtained from the Ni atom at the center of the Ni<sub>13</sub> cluster. When comparing the plots to the measured spectra from Figure 7b (yellow line), it is found that besides an overall shift of about 10 eV, the spectra contain two peaks (denoted as P1 and P2) that are consistent with that observed in the samples. Although the low energy peak P1 and high energy peak P2 is the opposite directions with the experimental spectrum, which might be due to the relatively small amount of hydrogen in the experiment, the features in the simulated spectra are very similar to the measurements. It can be seen from the experimental spectra (Figure 6.8) that the height of the P1 peak, the so-called white line, depends strongly on the electron occupation of the Ni atoms as illustrated through the intensity change upon NiO reduction where the white line decreases as the reduction temperature increases. Nevertheless, the pre-edge of each spectrum hardly changes upon the reduction

process indicating that the local structure of the Ni cluster is maintained. Likewise, the H<sub>2</sub> adsorption process exhibits similar behavior where the white line intensity increases upon the adsorption. Such character was confirmed by our simulated spectra that the white line shifts toward higher intensity as H coverage is increased. The increased white-line intensity reflects the lower occupation number of the Ni cluster suggesting the transfer of electrons from the Ni cluster to the adsorbed hydrogen. Overall, the measured and simulated spectra are in reasonable agreement with the Bader charge analysis that Ni tends to share its electrons to form Ni–H bonds upon adsorption.

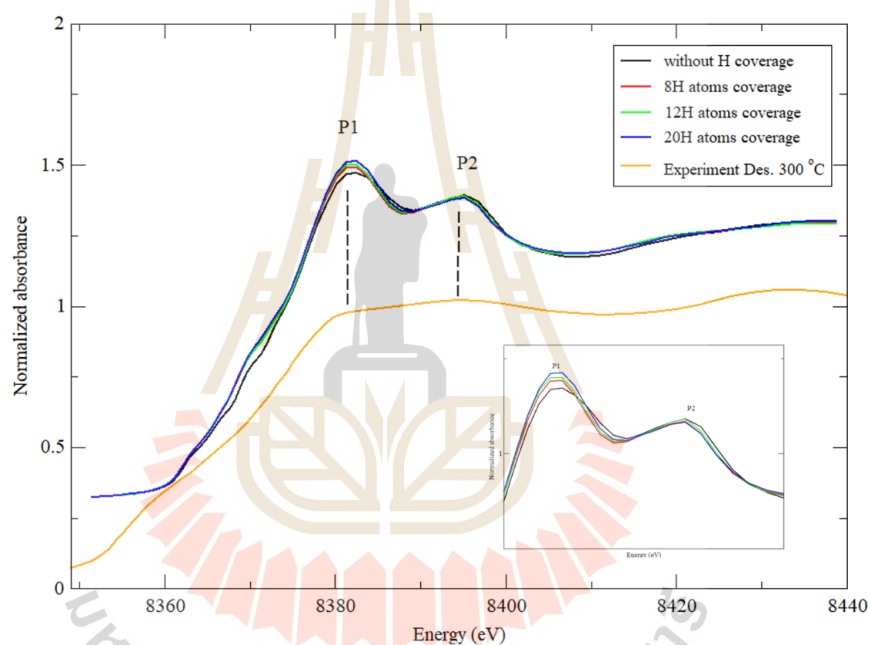


**Figure 6.8** The H adsorbed structures at various hydrogen coverages were then used to simulate XANES spectra compared with the measured spectra.

## 6.5 Conclusion

This chapter starts with the carbon-based materials synthesis from the melamine-formaldehyde resin used as a carbon source where the N- and O-rich HCS with the good atomic distribution. The highest hydrogen capacity at 298 K under 20-100 bar H<sub>2</sub> of 0.87-2.4 wt% H<sub>2</sub> was obtained from HCS doped with 2 wt % Ni. The interactions between Ni nanoparticles and heteroatoms of HCS were experimentally

and theoretically confirmed by Ni-N, Ni-O, and C-O-Ni bonds (Ni 2p and O 1s XPS results) and strong binding energy of 5.41 eV (twice as high as binding energy between Ni and pristine carbon). Suitable Ni loading content and strong Ni-HCS interactions led to well-dispersed Ni nanoparticles with small sizes on HCS, resulting in high reactive surface area for hydrogen adsorption and prevention of Ni particle agglomeration upon cycling. For hydrogen adsorption, computational and experimental studies confirmed not only chemisorbed hydrogen and Kubas dihydrogen complexes onto Ni nanoparticle via electron transfer from Ni to adsorbed hydrogen. Then, the second model was constructed from the activated carbon nanofibers (ACNF\*) prepared by carbonization and chemical activation of polyacrylonitrile (PAN)-polyvinylpyrrolidone (PVP) electrospun nanofibers. The 5–20 wt% of Ni-doped on ACNF\* are proposed for hydrogen adsorption at 25 °C. The best hydrogen adsorption capacities up to 2.12 wt% H<sub>2</sub> (p(H<sub>2</sub>) = 100 bar) together with cycling stability upon 10 ad/desorption cycles with an average capacity of 1.17 wt% H<sub>2</sub> (p(H<sub>2</sub>) = 50 bar) are obtained from 5 wt% Ni-doped ACNF\*. Excellent ad/desorption and reversibility are benefited from small particle sizes (5–10 nm) and the uniform distribution of Ni nanoparticles. The latter is due to suitable Ni loading content (5 wt%) and strong interaction between Ni nanoparticles and N atoms in ACNF\*, confirmed by both experiments and first-principles computations. Both experiments and computations indicate that hydrogen adsorption mechanisms are not only chemisorption of adsorbed hydrogen atoms onto Ni nanoparticles but also physisorption and spillover of hydrogen.

## 6.6 References

- Bian, Y., Bian, Z.-Y., Zhang, J.-X., Ding, A.-Z., Liu, S.-L., and Wang, H. (2015). Effect of the oxygen-containing functional group of graphene oxide on the aqueous cadmium ions removal. *Appl. Surf. Sci.* 329, 269.
- Grimme, S. (2006). Semiempirical GGA-type density functional constructed with a long-range dispersion correction. *J. Comput. Chem.* 27, 1787.

- Grimme, S., Antony, J., Ehrlich, S., and Krieg, H. (2010). A consistent and accurate ab initio parametrization of density functional dispersion correction (DFT-D) for the 94 elements H-Pu. *J. Chem. Phys.* *132*, 154104.
- Hedin, L. and Lundqvist, B. I. (1971). Explicit local exchange-correlation potentials. *J. Phys. C.* *4*, 2064.
- Henkelman, G., Arnaldsson, A., and Jónsson, H. (2006). A fast and robust algorithm for Bader decomposition of charge density. *Comput. Mater. Sci.* *36*, 354.
- Jalili, S., Goliaei, E. M., and Schofield, J. (2017). Silver cluster supported on nitrogen-doped graphene as an electrocatalyst with high activity and stability for oxygen reduction reaction. *Int. J. Hydrog. Energy.* *42*, 14522.
- Kresse, G. and Furthmüller, J. (1996). Efficiency of ab-initio total energy calculations for metals and semiconductors using a plane-wave basis set. *Comp. Mat. Sci.* *6*, 15.
- Kresse, G. and Joubert, D. (1999). From ultrasoft pseudopotentials to the projector augmented-wave method. *Phys. Rev. B.* *59*, 1758.
- Kubas, G. J. (2001). Metal–dihydrogen and  $\sigma$ -bond coordination: the consummate extension of the Dewar–Chatt–Duncanson model for metal–olefin  $\pi$  bonding. *J. Organomet. Chem.* *635*, 37.
- Li, Y., Li, S., Wang, Y., Wang, J., Liu, H., Liu, X., Wang, L., Liu, X., Xue, W., and Ma, N. (2017). Electrochemical synthesis of phosphorus-doped graphene quantum dots for free radical scavenging. *Phys. Chem. Chem. Phys.* *19*, 11631.
- Liu, H., Wang, X., Zhai, G., Zhang, J., Zhang, C., Bao, N., and Cheng, C. (2012). Preparation of activated carbon from lotus stalks with the mixture of phosphoric acid and pentaerythritol impregnation and its application for Ni(II) sorption. *Chem. Eng. J.* *209*, 155.
- López-Corral, I., Germán, E., Juan, A., Volpe, M. A., and Brizuela, G. P. (2011). DFT Study of Hydrogen Adsorption on Palladium Decorated Graphene. *J. Phys. Chem. C.* *115*, 4315.
- Monkhorst, H. J. and Pack, J. D. (1976). Special points for Brillouin-zone integrations. *Phys. Rev. B.* *13*, 5188.

- Montejo-Alvaro, F., Oliva, J., Zarate, A., Herrera-Trejo, M., Hdz-García, H. M., and Mtz-Enriquez, A. I. (2019). Icosahedral transition metal clusters (M13, M = Fe, Ni, and Cu) adsorbed on graphene quantum dots, a DFT study. *Physica E Low Dimens. Syst. Nanostruct.* 110, 52.
- Nosé, S. (1984). A molecular dynamics method for simulations in the canonical ensemble. *Mol. Phys.* 52, 255.
- Perdew, J. P., Burke, K., and Ernzerhof, M. (1996). Generalized Gradient Approximation Made Simple. *Phys. Rev. Lett.* 77, 3865.
- Plerdsranoy, P., Thaweelap, N., Poo-arporn, Y., Khajondetchairit, P., Suthirakun, S., Fongkaew, I., Chanlek, N., Utke, O., Pangon, A., and Utke, R. (2021). Hydrogen adsorption of O/N-rich hierarchical carbon scaffold decorated with Ni nanoparticles: Experimental and computational studies. *Int. J. Hydrog. Energy.* 46, 5427.
- Rangel, E., Sansores, E., Vallejo, E., Hernández-Hernández, A., and López-Pérez, P. A. (2016). Study of the interplay between N-graphene defects and small Pd clusters for enhanced hydrogen storage via a spill-over mechanism. *Phys. Chem. Chem. Phys.* 18, 33158.
- Rehr, J. J., Kas, J. J., Prange, M. P., Sorini, A. P., Takimoto, Y., and Vila, F. (2009). Ab initio theory and calculations of X-ray spectra. *C. R. Phys.* 10, 548.
- Sahoo, S., Gruner, M. E., Khanna, S. N., and Entel, P. (2014). First-principles studies on graphene-supported transition metal clusters. *J. Chem. Phys.* 141, 074707.
- Sanville, E., Kenny, S. D., Smith, R., and Henkelman, G. (2007). Improved grid-based algorithm for Bader charge allocation. *J. Comput. Chem.* 28, 899.
- Thaweelap, N., Plerdsranoy, P., Poo-arporn, Y., Khajondetchairit, P., Suthirakun, S., Fongkaew, I., Hirunsit, P., Chanlek, N., Utke, O., Pangon, A., and Utke, R. (2021). Ni-doped activated carbon nanofibers for storing hydrogen at ambient temperature: Experiments and computations. *Fuel.* 288, 119608.
- Tian, Y., Liu, Y.-j., Zhao, J.-x., and Ding, Y.-h. (2015). High stability and superior catalytic reactivity of nitrogen-doped graphene supporting Pt nanoparticles as a catalyst for the oxygen reduction reaction: a density functional theory study. *RSC Adv.* 5, 34070.

## CHAPTER VII

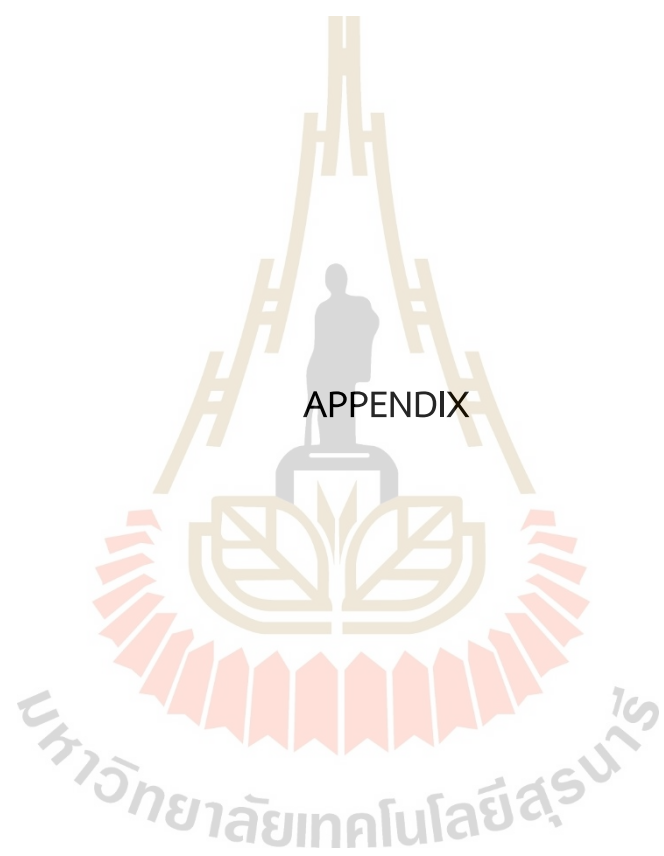
### CONCLUSIONS

This thesis studies the effect of TM catalysts on hydrogen adsorption kinetics on the chemical storage materials, which can be used in the long term and desirable potential for hydrogen storage application. Both Mg-based and carbon-based materials have been extensively studied as the hydrogen storage application. To improve the drawback of these materials, adding transition metals as a catalyst can improve the hydrogen storage performance. The role of TMs in alternative chemical storage has been the focus of this work. Since Mg-based hydrogen storage material operated hydrogen at ambient temperature is highly desirable. To make lower the operating temperature for hydrides, the TMs acting as catalysts were added to improve the hydrogen storage materials performance. On the other hand, carbon-based materials have the disadvantage of small hydrogen sorption enthalpy due to low H<sub>2</sub> uptake. The new strategy to increase the operating temperature for carbon-based material is a combination of heteroatoms and TMs on the adsorbent, increasing the binding energy between metal particles and substrate. The role of TMs of alternative chemical storage has been focused on using first-principles approaches. The hydrogen sorption kinetics has been a major challenge for the hydrogen storage material. The main conclusions derived from this work are:

- The synergistic roles of TMs catalysts on hydrogen absorption in Mg-based storage materials were investigated using first-principles approaches. Computations reveal that both Ni and V catalysts energetically and kinetically improve hydrogen adsorption that H<sub>2</sub> molecules spontaneously dissociate and strongly interact with the catalysts. The hydrogen dissociation process becomes barrierless on Mg<sub>2</sub>Ni and V/Mg<sub>2</sub>Ni surfaces. The electronic structure analysis provides a deeper understanding of their catalytic roles from the well-overlapped molecular orbitals of

adsorbed hydrogen and  $3d$  states of Ni and V atoms. The presence of Ni promotes not only hydrogen dissociation and adsorption process but also subsurface diffusion; however, hydrogen surface diffusion on  $Mg_2Ni$  surface could be kinetically limited at low hydrogen coverage. The presence of the V cluster induces surface reconstruction resulting in more favorable sites, i.e., V-Ni bridges and connected Ni sites, for hydrogen adsorption and increases the number of strong adsorptions; thus, hydrogen uptakes are enhanced. In addition, the structure reconstruction upon V deposition also facilitates hydrogen atoms spill over and surface diffusion via V-Ni bridges and connected Ni sites, respectively. The surface, subsurface, and under-subsurface diffusion kinetics are dramatically improved at high hydrogen coverages. The computations suggest that the effect of Ni and V catalysts on hydrogen absorption enhancement, including hydrogen adsorption and diffusion processes, could considerably be pronounced at the operating condition of high  $H_2$  pressure.

- The effect of Ni on defect graphene found that the combination of Ni nanoparticle and heteroatom dope on graphene (defect with heteroatoms) can improve the hydrogen adsorption and hydrogen capacity. The role of Ni on different defect graphene has been investigated using density functional theory calculation. Suitable Ni loading content and strong Ni-adsorbents interactions led to well-dispersed Ni nanoparticles, resulting in high reactive surface area for hydrogen adsorption and prevention of Ni particle agglomeration upon cycling. For hydrogen adsorption, computational and experimental studies confirmed not only chemisorbed hydrogen and Kubas dihydrogen complexes onto Ni nanoparticles via electron transfer from Ni to adsorbed hydrogen.



APPENDIX

## APPENDIX

### PUBLICATION AND PRESENTATIONS

#### A.1 List of publications

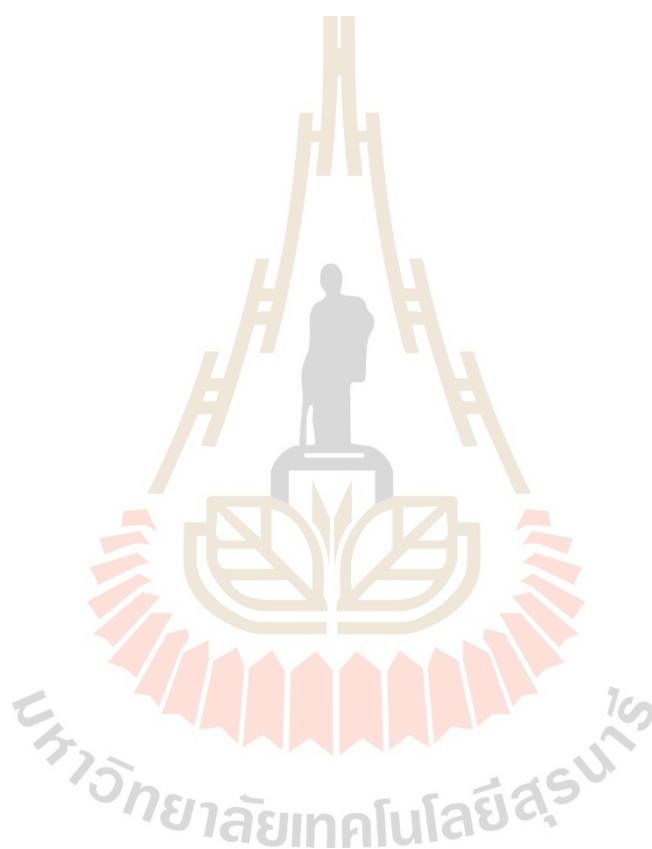
Plerdsranoy, P., Thaweelap, N., Poo-arporn, Y., Khajondetchairit, P., Suthirakun, S., Fongkaew, I., Chanlek, N., Utke, O., Pagon, A., Utke. R. (2021). Hydrogen Adsorption of O/N-rich Hierarchical Carbon Scaffold Decorated with Ni Nanoparticles: Experimental and Computational Studies. *Int. J. Hydrog. Energy* 46: 5427.

Thaweelap, N., Plerdsranoy, P., Poo-arporn, Y., Khajondetchairit, P., Suthirakun, S., Fongkaew, I., Hirunsit, P., Chanlek, N., Utke, O., Pagon, A., Utke. R. (2021). Ni-doped Activated Carbon Nanofibers for Storing Hydrogen at Ambient Temperature: Experiments and Computations. *Fuel* 288: 119608



## A.2 List of presentations (oral)

Khajondetchairit, P., Ngamwongwan, L., Hirunsit, P., and Suthirakun, S. (October 2021). Role of V and Ni Catalysts on Hydrogen Sorption Kinetics of Mg-based Hydrogen Storage Materials: A Computational Study. **6<sup>th</sup> International Conference on Computation for Science and Technology 2021 (6<sup>th</sup> ICCST)**. Faculty of Pharmacy, Chiang Mai University, Thailand.



**Role of V and Ni Catalysts on Hydrogen Sorption Kinetics  
of Mg-based Hydrogen Storage Materials:  
A Computational Study**

Patcharaporn Khajondetchairit<sup>1,4</sup>, Lappawat Ngamwongwan<sup>2,4</sup>, Pussana Hirunsit<sup>3,4\*</sup>,  
Suwit Suthirakun<sup>1,4,\*</sup>

<sup>1</sup>*School of Chemistry, Institute of Science, Suranaree University of Technology, Nakhon Ratchasima, 30000, Thailand;* <sup>2</sup>*School of Physics, Institute of Science, Suranaree University of Technology, Nakhon Ratchasima, 30000, Thailand;* <sup>3</sup>*National Nanotechnology Center, National Science and Technology Development Agency, Pathum Thani, 12120, Thailand;* <sup>4</sup>*Research Network NANOTEC – SUT on Advanced Nanomaterials and Characterization, School of Chemistry, Suranaree University of Technology; suthirak@sut.ac.th*

Adding transition metals (TMs) in Mg-based hydrogen storage materials has been proposed as a promising approach to improve their storage performance. In particular, previous experimental study reported that, upon adding Ni and V catalysts in the Mg, formation enthalpy activation energies of de/hydrogenation were dramatically decreased.<sup>1</sup> Herein, we aim to unravel the roles of Ni and V catalysts on improving kinetics and thermodynamics of hydrogen absorption in the Mg-based storage materials using first-principles methods. The surface models used in this study account for the addition of Ni catalysts in the form of Mg<sub>2</sub>Ni surface whereas the deposition of V catalyst exist as a cluster on the surface, as evident<sup>2</sup> from the experimental observations. We find that both V and Ni help stabilize hydrogen adsorption and facilitate dissociation of the H–H bond. Such strong interactions stem from the strong hybridization between molecular orbital of the molecule and the transition metal 3d states.<sup>3</sup> The addition of the V cluster on the Mg<sub>2</sub>Ni surface induces surface reconstruction which in turn provides extra adsorption sites and creates facile diffusion paths where hydrogen can easily spillover from the cluster to surface. The diffusion kinetics on the surface are also improved upon deposition of V cluster since the reconstruction causes the formation of connected Ni sites which serve as low-energy diffusion paths. Although the diffusion into the materials requires significantly higher barriers, increasing hydrogen coverages reduces such barriers by a half suggesting that hydrogen absorption into the materials is kinetically appreciable at operating conditions of high H<sub>2</sub> pressure. The catalytic roles of Ni and V are confirmed by the results obtained from ab-initio molecular dynamic simulations where hydrogen prefers to dissociatively adsorb on the TM sites and can further diffuses into the subsurface region. Through systematic computational investigations, our findings provide useful insights and guidance on using combination of TM catalysts to improve performance of Mg-based hydrogen storage materials.

**References**

1. Sakamoto, T.; Atsumi, H. *Fusion Eng. Des.*, **2019**, *138*, 6-9.
2. Xiubo, X.; Ming, C.; Peng, L.; Jiaxiang, S.; Tong, L. *Chem. Eng*, **2018**, *347*, 145-155.
3. Valencia, H.; Gil, A.; Frapper, G. *J. Phys. Chem. C*, **2015**, *119*, 5506-5522.

## CURRICULUM VITAE

Patcharaporn Khajondetchairit was born on April 5, 1992, in Nakhon Ratchasima, Thailand. She received her bachelor's degree in Chemistry (second-class honors) in 2014 from Rajamangala University of Technology Isan, Thailand. During her bachelor's degree, she completed an internship (3 months) at the Soil analysis divisions of the office of agricultural research and development region 3, Khonkaen, Thailand. She then continued her master's study in Chemistry, Faculty of Science, Kasetsart University with a Graduate school Scholarship from Kasetsart University under the supervision of Assoc. Prof. Dr. Matthew Paul Gleeson. She was studied in computational and Medicinal Chemistry Laboratory (CMCL) used the computational design of the lead compounds to match the protein target, synthesized, and purified the compounds. In 2017, she has published an article in an international journal and participated in an international conference during her master's program. In 2019, she joined the Computational and Material Science and Catalysis group (COMSCAT) as a Ph.D. student under the supervision of Asst. Prof. Dr. Suwit Suthirakun with Research Network of Nanotechnology (RNN), and One Research One Graduate (OROG) scholarships from Institute of Research and Development, Suranaree University of Technology. During the period of her Ph.D. program, she has published articles in an international journal and participated in international conferences (listed in APPENDIX) during her Ph.D. program. Her expertise in Computational materials design and heterogeneous catalysis is based on density functional theory (DFT) calculation. The results of this research project are described in this thesis.